

N74-28272

NASA TECHNICAL TRANSLATION

NASA TT F-15,537

SPACE RESEARCH IN THE UKRAINE  
NO. 3. SPACE PHYSICS AND ASTRONOMY

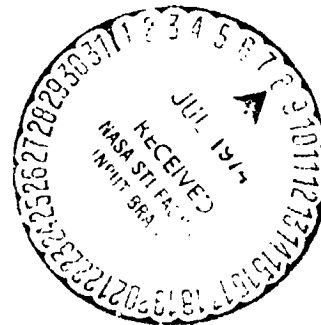
(NASA-TT-F-15537) SPACE RESEARCH IN THE  
UKRAINE. NO. 3: SPACE PHYSICS AND  
ASTRONOMY (Kanner (Leo) Associates)  
171 p HC \$11.75

CSCI 03A

N74-28272  
THRU  
N74-28285  
Unclass  
41673

G3/30

Translation of "Kosmicheskiye Issledovaniya na Ukraine, Vypusk 3.  
Fizika Kosmosa i Astronomiya," Kiev, "Naukova Dumka"  
Publisher, 1973, pp. 1-111



NATIONAL AERONAUTICS AND SPACE ADMINISTRATION  
WASHINGTON, D.C. 20546  
MAY 1974

## STANDARD TITLE PAGE

1. Report No. NASA TT F-15,537	2. Government Accession No.	3. Recipient's Catalog No.	
4. Title and Subtitle SPACE RESEARCH IN THE UKRAINE, NO. 3, SPACE PHYSICS AND ASTRONOMY		5. Report Date MAY 1974	
		6. Performing Organization Code	
7. Author(s)		8. Performing Organization Report No.	
		10. Work Unit No.	
9. Performing Organization Name and Address Leo Kanner Associates Redwood City, California 94063		11. Contract or Grant No. NASW-2481	
		13. Type of Report and Period Covered Translation	
12. Sponsoring Agency Name and Address National Aeronautics and Space Admin- istration, Washington, D.C. 20546		14. Sponsoring Agency Code	
15. Supplementary Notes  Translation of "Kosmicheskiye Issledovaniya na Ukraine, Vypusk 3. Fizika Kosmos i Astronomiya," Kiev, "Naukova Dumka" Publisher, 1973, pp. 1-111			
16. Abstract  This collection examines problems in cosmic rays, electro-magnetic processes in the atmospheres of pulsars, ionospheric physics and the propagation of radio waves from space objects, electromagnetic processes in the earth's magnetosphere and their relationship with chromospheric flares, and studies of the moon and the planets of the solar system using astronomical methods, along with methodological and instrumental advances.			
17. Key Words (Selected by Author(s))		18. Distribution Statement  Unclassified-Unlimited	
19. Security Classif. (of this report)  Unclassified	20. Security Classif. (of this page)  Unclassified	21. No. of Pages	22. Price

### Annotation

This collection examines problems in cosmic rays, electromagnetic processes in the atmospheres of pulsars, ionospheric physics and the propagation of radio waves from space objects, electromagnetic processes in the earth's magnetosphere and their relationship with chromospheric flares, and studies of the moon and the planets of the solar system using astronomical methods, along with methodological and instrumental advances.

This collection is intended for scientific and engineering-technical personnel investigating space, space physics, astronomy, and developing instruments for space research.

### Editorial Board:

Academician of the Ukrainian SSR [UkSSR] Academy of Sciences  
G.S. Pisarenko (chief editor)

Academician of the UkSSR Academy of Sciences Yu.A. Mitropol'skiy  
(assistant chief editor)

Candidate of Technical Sciences N.V. Novikov (assistant chief editor)

Academician of the UkSSR Academy of Sciences S.I. Subbotin  
(assistant to chief editor)

Academician of the UkSSR Academy of Sciences I.N. Frantsevich  
(assistant chief editor)

Academician of the UkSSR B.I. Verkin

Corresponding member of the UkSSR Academy of Sciences D.A. Dudko

Candidate of Biological Sciences V.A. Kordyum

Corresponding member of the UkSSR Academy of Sciences N.N. Sirotinin

Corresponding member of the UkSSR Academy of Sciences V.I. Trefilov

Academician of the UkSSR Academy of Sciences A.Ya. Usikov

Academician of the UkSSR Academy of Sciences Ye.P. Fedorov

Candidate of Technical Sciences E.A. Eskin (chief secretary)

### Chief Editor of Issue:

Academician of the UkSSR Academy of Sciences S.I. Subbotin

## TABLE OF CONTENTS

	Page
Long-term Integrated Radiophysical Studies of the Ionosphere, Near Space, and the Propagation of Radio Waves From Space Objects	1 ✓
Study of the Moon and Planets at the Khar'kov State University Astronomical Observatory	29 ✓
Electromagnetic Processes in the Atmosphere of Pulsars	44 ✓
Diurnal and Seasonal Trends in the Incidence of Sudden Commencements (SC) and Sudden Impulses (SI)	54
Chromospheric Flares and Sudden Commencements of Geomagnetic Storms	61
Acceleration of Solar Cosmic Rays During Chromo- spheric Flares	69
Effect of Small Flares in the Neutral Component of Secondary Cosmic Radiation	77
Analysis of the Nature of Excessive Cosmic Radiation in the Area of the Brazilian Magnetic Anomaly at Altitudes 250-500 km, From Kosmos-225 Satellite Data	86
Instruments for Measuring Radiant Thermal Fluxes	95
Possibility of Using Sources of Vacuum Ultraviolet Irradiation to Solve Problems of Space Materials Science	102 ✓
Method of Calculating Gas-Dynamics and Heat Transfer in Single-Stage Refrigeration Units	124
Problem of Selecting Optimal Regimes for Storage of Cryogenic Agents	139 ✓
Intermediate Memory Devices	155



"Long-term integrated radiophysical studies of the ionosphere, near space, and the propagation of radio waves from space objects," Misyura, V.A., Kosmicheskiye issledovaniya na Ukraine, No. 3, "Naukova dumka," Kiev, 1973, p. 3.

A brief review is presented along with a generalization of original studies of the ionosphere, near-space, and the interplanetary medium, and the propagation of radio waves from space objects, which was conducted with the participation and under the supervision of the author over a 20 year period by groups of Ukrainian scientists, and also in collaboration with scientists of other republics and as part of the Interkosmos program. Emphasis is placed on studies in which the Khar'kov State University participated.

Bibliography: 41 entries; figures: 12; tables: 2.

"Study of the moon and planets at the Khar'kov State University Astronomical Observatory," N.P. Barabashov (deceased), Kosmicheskiye issledovaniya na Ukraine, No. 3, "Naukova dumka," Kiev, 1973, p. 20.

Results of observations of the moon and planets conducted under the supervision of the author are described. Data on the discovery of high porosity values and the broken terrain of the lunar surface are given, with data on the coloration of rocks in the lunar surface; the Khar'kov observers refute the results of Landerer based on polarimeter observations of the moon.

A comparative description is given of data of astronomical and satellite observations.

"Electromagnetic processes in the atmosphere of pulsars," Yukhimuk, A.K., Kosmicheskiye issledovaniya na Ukraine, No. 3, "Naukova dumka," Kiev, 1973, p. 30.

The work consists of two parts. The first deals with the fine structure of radio pulses. Based on kinetic theory, processes occurring in the plasma shell of a pulsar when external electromagnetic radiation is present are investigated. It is shown that acted on by an electromagnetic wave, electrons drift relative to ions, which is the cause of the excitation of longitudinal oscillations. A dispersion equation describing the longitudinal oscillations in magnetized plasma is derived. Conditions for excitation of oscillations are found. Correlation functions of electron density are calculated, along with the coefficients of electromagnetic wave scattering. It is shown that variations in the amplitude of pulsar pulses are associated with scintillations caused by fluctuations in the plasma electron density.

The second part of the work presents a mechanism for the radio emission of pulsars. The model of a rotating and a pulsating star, a neutron star with dipolar or more complex magnetic field, is examined. Charged particles are accelerated in the pulsating magnetic fields. Accelerated charged particles lead to the formation of radiation belts. Particles from the radiation belts storing the pulsations are expelled into the near-polar regions owing to the disruption of the adiabatic invariant. Emission of electromagnetic waves occurs when rotating relativistic electrons travel along curved trajectories, which are identified with the force lines issuing from the magnetic poles of a pulsar.

Bibliography: 17 entries.

"Diurnal and seasonal trends in the incidence of sudden commencements (SC) and sudden impulses (SI)," Nesmyanovich, E.I., Kosmicheskiye issledovaniya na Ukraine, No. 3, "Naukova dumka," Kiev, 1973, p. 37.

Based on world data for the period 1 January 1955 to 31 December 1968, reports of 894 SC cases and 2152 SI cases were collected, based on which a study was made of the diurnal and seasonal trends in the incidence of their appearances.

It is shown that the diurnal trend is pronounced for all events with a maximum at (06-8)<sup>h</sup> UT [world time].

The diurnal trend for SC in the resultant period is more pronounced. The seasonal trend in incidence of appearances of SC and SI is absent.

Thus, geomagnetic disturbances of both SC and SI are monitored by world time.

These results lead to the conclusion that the presence or absence of SC and SI during geomagnetic storms is determined not only by the nature of the corpuscular flux, the presence of shock waves and tangential discontinuities, but also by purely terrestrial conditions.

The classification of storms based on types of commencements is extremely arbitrary.

Bibliography: 8 entries; figures: 2; tables: 3.

"Chromospheric flares and sudden commencements of geomagnetic storms," Nesmyanovich, A.T. and Nesmyanovich E.I., Kosmicheskiye issledovaniya na Ukraine, No. 3, "Naukova dumka," Kiev, 1973, p. 40.

The authors compiled a catalogue of flare activity during 1957-1967 (the solar activity cycle). By comparing all reliable SC during this period with chromospheric flares, the following conclusions can be drawn:

1. There is no statistically significant correlation between SC and chromospheric flares. One cannot draw conclusions on the rate of propagation of shock waves or solar plasma from the lag time of a SC relative to any nearest flare occurrence.

2. The assumption that a shock wave propagates throughout the entire hemisphere is unjustified and contradicts the fact of recurrence of SC.

3. A statistically significant correlation was established between SC and chromospheric flares, that is, a relationship between a SC and the moment that a flare active region transits the Central Meridian.

4. SC are caused by shock waves or tangential discontinuities formed at the western boundary of the quasisteady directed corpuscular flux or at the boundary between sectors.

Bibliography: 11 entries; figures: 2; tables: 3.

"Acceleration of solar cosmic rays during chromospheric flares," Dorman, L.I., Raychenko, L.V., and Yukhimuk, A.K., Kosmicheskiye issledovaniya na Ukraine, No. 3, "Naukova dumka," Kiev, 1973, p. 45.

Using the Focker-Planck equation, an examination is made of the acceleration of charged particles by fluctuational electric fields caused by the propagation of intense radio emission in the long-wave range. Correlation functions of electric fields near the boundary of plasma instability were computed. The interaction of charged particles with these fields is examined. It is shown that due to the interaction of particles with fluctuational fields, solar cosmic rays can be accelerated to energies of  $E = 10^2 - 10^3$  Mev.

Bibliography: 10 entries.

"Effect of small flares in the neutral component of secondary cosmic radiation," Bondarenko, V.I., Raycheko, L.V., and Yukhimuk, A.K., Kosmicheskiye issledovaniya na Ukraine, No. 3, "Naukova dumka," Kiev, 1973, p. 50.

Results are presented of an investigation of the effect of small flares, scale divisions 1 and 1<sup>+</sup> in the neutron component of secondary cosmic radiation from the data of neutron supermonitors at the stations of Kiev, Bukhta Tiksi, and Deep River. It is shown that flares of scale divisions 1 and 1<sup>+</sup> are accompanied by an effect in the neutron component amounting to about 0.4%. A mechanism for the outflow of particles accelerated in small flares owing to diffusion across the magnetic field of a trap is presented.

Bibliography: 10 entries; figures: 6.

"Analysis of the nature of excessive cosmic radiation in the area of the Brazilian magnetic anomaly at altitudes 250-500 km, from Kosmos-225 satellite data," Raychenko, L.V., Kosmicheskiye issledovaniya na Ukraine, No. 3, "Naukova dumka," Kiev, 1973, p. 55.

Results are presented from a study of the region of anomalous cosmic radiation in the area of the Brazilian magnetic anomaly at the altitudes 250-500 km, using data measurements taken on the Kosmos-225 satellite (14-29 June 1968). The existence of a stable intensity anomaly discovered in the experiments on the second and third Soviet spacecraft-satellites [1-3] is confirmed. The total vector of the geomagnetic field at different altitudes was compared with isoline maps. For the first time an altitude profile of the South Atlantic anomaly of radiation intensity was obtained, using data from the same instrument. The nature of the anomalies in cosmic radiation intensity over the regions of negative magnetic anomalies is discussed.

Bibliography: 8 entries; figures: 9.

"Instruments for measuring radiant thermal fluxes," Gerashchenko, O.A., and Sazhina, S.A., Kosmicheskiye issledovaniya na Ukraine, No. 3, "Naukova dumka," Kiev, 1973, p. 62.

An absolute two-sided radiometer is described, based on the principle of replacing absorbed radiant energy with electrical. The sensitive element of the detector is a thermoelectric transducer of thermal flux. The design, fabrication technology, methods of measurement, technical characteristics and general view of the instrument are presented.

Bibliography: 2 entries; figures: 2.

"Possibility of using sources of vacuum ultraviolet irradiation to solve problems of space materials science," Verkhovtseva, E.T., and Yaremenko, V.I., Kosmicheskiye issledovaniya na Ukraine, No. 3, "Naukova dumka," Kiev, 1973, p. 66.

An urgent problem in space materials science is simulating the interaction of vacuum ultraviolet (VUV) of solar emission (spectral region  $\lambda < 2000 \text{ \AA}$ ) with solids in space conditions, that is, producing a light source with a distribution that approximates the distribution of solar energy.

This review presents information on the distribution of the energy flux of VUV of solar radiation; requirements that must be satisfied by the VUV source used for space materials science are formulated; and a critical evaluation is given of the possibilities of using existing sources for space materials science. From this evaluation it was established that none of the sources of VUV satisfies the specific requirements imposed on the simulator of solar radiation. A way out of this impasse was found to be the development in the FTINT [transliterated] of the Ukrainian SSR Academy of Sciences of a new type of source based on exciting a supersonic gas jet flowing into vacuum with a dense electron beam. The article stresses a source of a new type -- its spectral and operation characteristics are presented.

Bibliography: 72 entries; figures: 9; tables: 5.

"Method of calculating gas-dynamics and heat transfer in single-stage refrigeration units," Zhitomirskiy, I.S., and Podol'skiy, A.G., Kosmicheskiye issledovaniya na Ukraine, No. 3, "Naukova dumka," Kiev, 1973, p. 80.

A generalized mathematical model of gas-dynamic and heat-transfer processes in single-stage regenerative installations operating in Sterling, MacMahon, Gifford-MacMahon, and pulsating tube cycles is proposed.

A numerical method of solving initial equations on a digital computer is examined, making it possible to calculate the change in thermodynamic parameters in the working cycle in different machine components, as well as the dependence of cold productivity on the temperature level in the steady regime.

Bibliography: 24 entries; figures: 6.

"Problem of selecting optimal regimes for storage of cryogenic agents," Mikhal'chenko, R.S., Getmanets, V.F., and Iskhakov, Yu.F., Kosmicheskiye issledovaniya na Ukraine, No. 3, "Naukova dumka," Kiev, 1973, p. 90.

A thermodynamic analysis is given of different regimes of storage of hydrogen, nitrogen, oxygen, and argon using the high vacuum of space. Optimal regimes are determined from the standpoint of minimizing weight characteristics. Several new storage regimes are proposed.

Bibliography: 17 entries; figures: 8; tables: 1.

"Intermediate memory devices," Basalayev, G.V., Kmet', A.B., Rakov, M.A., and Tarasevich, V.A., Kosmicheskiye issledovaniya na Ukraine, No. 3, "Naukova dumka," Kiev, 1973, p. 101.

This article briefly describes problems and several methods of transfer and processing of data whose practical implementation requires operational memory devices.

Devices incorporating multistable elements are presented; their main parameters are given and the possibility of using the proposed devices for storing information for transmission in space radiocommunications channels is indicated.

Bibliography: 6 entries; figures: 2.

N74-28273

LONG-TERM INTEGRATED RADIOPHYSICAL STUDIES OF THE IONOSPHERE,  
NEAR SPACE, AND THE PROPAGATION OF RADIO WAVES FROM SPACE OBJECTS

V. A. Misyura

Introduction and Formulation of Problem

/3\*

Radiophysical studies of the ionosphere and space consist [1] of the direct measurement of certain effects induced in the propagation (or reradiation) of radio waves from space objects (SO)\*\*. From measured effects and from data on the motion and position of SO given physical parameters of the medium and bodies (inverse problem) are determined, or else effects that are for some reason inconvenient to measure directly. These effects can be also of independent scientific and practical interest [1].

The principal effects measured are usually these: the Faraday effect (angle  $\Phi$  and velocity (frequency)  $\Phi = 2\pi F\phi$  of the rotation of the plane of polarization in a gyrotropic plasma), corrections  $\Delta L$ ,  $\Delta R$ ,  $\Delta\phi$ , and  $\Gamma_{da}$  -- due to the medium -- to the optical path  $L$  and group path  $R_r$ , respectively, to the phase  $\phi$ , and to the doppler shift of the radio wave frequency  $F_d$ ; refraction (vertical)  $\Delta\beta$ , horizontal (azimuthal)  $\Delta\epsilon$ , lateral  $\Delta\epsilon$ , and astromic  $\Delta\beta$  and  $\Delta\epsilon$ , and so on); absorption, reflection, and scattering of radio waves, including the so-called incoherent scattering (IS) by thermal fluctuations of plasma (intensity  $P_s$  and spectrum  $\sigma(\omega)$  of scattering), distortions of radio signals, and so on. Parameters of the medium, like the effects, can contain regular and sporadic components in the propagation of radiowaves.

Media such as planetary atmosphere and the interplanetary and interstellar medium are usually weakly inhomogeneous (at distances of the order of a radio wavelength), and therefore the powerful method of geometrical optics can be used in the theory and calculation of radio wave propagation.

---

1 By SO in radiophysical studies, we will mean satellites, rockets, spacecraft, and launch vehicles, planets, and also volumes of plasma, astronomical sources of radio waves, and other natural and artificial bodies and formations in the ionosphere and further away, radiating or reradiating radio waves.

\* Numbers in the margin indicate pagination in the foreign text.

Since the dielectric constant of plasma (or index of refraction  $n$ ) depends mainly on its electron concentration  $N$  (and also on the rate of collision  $\nu$  of electrons with other particles in the medium, magnetic field intensity  $H$ , frequency of radio waves  $f$ , and so on), the principal parameter of near and outer plasma obtained in radiophysical measurements is  $N$ . Parameters dependent on the distribution of  $N$  in space are also used -- total (integrated) electron concentration in the vertical column of the ionosphere of unit cross-sectional area ( $N_0$ ) and the ionosphere column of unit cross-sectional area inclined along the line of sight ( $N_L$ ) and extending from the point of observation to the level at which the SO is. The other parameters of the medium that are amenable to determination can include: electron temperature  $T_e$ , ion temperature  $T_i$ , and temperature of neutrals  $T_n$ , electron Larmor frequency  $f_N$  and ion Larmor frequency  $f_{Hi}$ , neutral and ionic composition, and also sporadic components of these quantities.

We will use the familiar formula:

$$n = \sqrt{\epsilon} = \sqrt{1 + \alpha}, \quad (1) \quad /4$$

where in the case of isotropic plasma (neglecting the magnetic field), with the collisions neglected

$$\alpha = -8.07Nf^{-2} = -\frac{f_p^2}{f^2}, \quad (2)$$

$N$  is electron concentration,  $10^5 \text{ el}\cdot\text{cm}^{-3}$ ;  $f$ , MHz;  $f_{pl}$  is plasma frequency ( $f_{pl_{\max}} = f_0$  is the critical frequency of the region

$F_2$ ,  $b^2 = f_0^2 f^{-2}$ ). In the case of gyrotropic plasma ( $H \neq 0$ ), it is sufficient to replace  $\alpha$  in (1) with the function  $\alpha_{o,e}$  ( $o$  is an ordinary and  $e$  is an extraordinary wave). In particular, for the so-called quasi-longitudinal and first high-frequency approximation

$$\alpha_{o,e} = \alpha \mp ab_L \quad (3)$$

to a precision up to small values of the order of  $\alpha b_L^2$ . Here the signs  $(-)$  and  $(+)$  refer, respectively, to the ordinary and extraordinary waves,  $b_L = f_L f^{-1}$ ,  $f_L$  is the projection of the Larmor frequency on the beam.

The studies examined in this article began more than 20 years ago, were gradually improved, expanded, and the precision of calculations and measurements was increased.

At the present time, the studies are integrated in the following aspect:

1. A number of regular and random parameters of the medium were measured independently or simultaneously at separate and widely scattered observational stations at the middle altitudes



(ML) of the Soviet Union and in the high latitudes (HL) of both hemispheres. These include  $N$ ,  $N_L$ ,  $N_0$ ,  $T_e$ ,  $T_i$ , ionic composition, transients  $\left(\frac{\partial N}{\partial t}, \frac{\partial N_0}{\partial t}, \eta = \frac{1}{N} \frac{\partial N}{\partial t}, \eta_0 = \frac{1}{N_0} \frac{\partial N_0}{\partial t}, \frac{\partial T_e}{\partial t}, \frac{\partial T_i}{\partial t}, \eta_e = \frac{1}{T_e} \frac{\partial T_e}{\partial t}, \eta_i = \frac{1}{T_i} \frac{\partial T_i}{\partial t}\right)$ , horizontal (x) gradients  $\left(\frac{\partial N}{\partial x}, \frac{\partial N_0}{\partial x}, \gamma = \frac{1}{N} \frac{\partial N}{\partial x}, \gamma_0 = \frac{1}{N_0} \frac{\partial N_0}{\partial x}\right)$ ,

longitudinal, latitudinal, and total gradients  $N_L$  and  $N_0$  along the track of the subionospheric satellite point and along the orbit (s) of the satellite ( $dN_L/ds$ ), vertical and inclined profiles of these parameters in the great expanse of the lower and outer ionosphere and exosphere, statistical characteristics of major inhomogeneities of these parameters, and also the above-noted regular and random effects in the propagation of radio waves

$(\Delta L, \Delta R, \Delta \beta, \Delta \varepsilon, F_{da}, \varphi, F_{\phi}, \Phi_{\phi})$ .

2. Theoretical and experimental studies were compared with each other.

3. Independent radiophysical methods were used simultaneously and separately: differential and single-frequency ED and EP signals reflected and radiated by satellites (Third AES [artificial earth satellite], Kosmos-12, -11, -53, -93, -95, -321, -356, -381, Interkosmos-2, Elektron-1, -2, -3, Explorer-19, -22, -27, Echo-1, and so on), by rocket (GPR - geophysical rockets and VSP - vertical space probe, launch to 4500 km) and by the moon, methods of incoherent scattering (IS), partial reflections (PR), cross modulation (CM), and vertical and phase soundings (VS and PS).

The most promising method is IS, which was first used in the Soviet Union in our integrated studies [2-7]. It is capable in the same, often repeated experiment of producing virtually all the main parameters of the lower and outer ionosphere and exosphere, their dynamics and inhomogeneities [2, 8]. In fact, the only drawback of the method is the complexity and high cost of IS equipment. Therefore there are thus far few facilities available [2]: in the lower (two facilities) and middle northern latitudes (US, USSR, Canada, France, and England -- several facilities)<sup>2</sup>.

15

The PR and CM methods are effective in measuring  $N$  and  $\nu$  in the lowest region of the ionosphere (region D). The new method of PS is more exact than VS for measurements of the entire lower ionosphere.

---

<sup>2</sup> Recently, the construction of two IS facilities has been oriented to the HL (cf., a paper by D. T. Farleigh at a session of the URSI-72 [transliterated] in Warsaw).

The method of differential ED and EP signals of vertically launched rockets yields reference vertical profiles of  $N$ ,  $N_0$ ,  $\partial N/\partial t$ , and  $\partial N_0/\partial t$ . Here the use of scattered observation points adds further the measurements of  $N_L$ ,  $\partial N_L/\partial t$ ,  $\Delta\beta$ ,  $\Delta L$ ,  $\Delta\epsilon$ , and profiles of the horizontal gradients ( $\partial N/\partial x$ ,  $\partial N_0/\partial x$ ,  $\gamma$ ,  $\gamma_0$ ) and the transients ( $\partial N/\partial t$ ,  $\partial N_0/\partial t$ ,  $\gamma$ ,  $\gamma_0$ ). The presence of several frequencies (especially coherent) and the combined recording of ED and EP increases the information and precision. Measurement of the vertical profiles of the horizontal gradients of  $N$  and  $N_0$  was first done in our 1962-1967 experiment [1, 9, 10, 11], especially at high altitudes  $\approx 450$  km [5, 7, 12, 13]. Placing probes and mass spectrometers on rockets also yielded profiles of  $T_e$ ,  $T_i$ , and composition. However, in contrast to IS, the rockets can provide only single-time measurements of profiles, which adds to measurement costs.

The use of this technique in satellite measurements at scattered points determined, in addition to  $N_L$ ,  $N$ ,  $\Delta\beta$ , and  $\Delta L$ , also the total horizontal gradients (magnitude and azimuth) of  $\gamma_0$  at the middle and high latitudes [1, 7, 13, 14, 15], and also provided statistical characteristics of the fluctuations of effects and parameters of the medium [5, 7, 13, 16]. Evidently, the first measurements of  $N_0$  by the difference EP technique in Soviet Union were in 1964 [14].

In recent years, a special portable radiotechnical ionospheric complex [17] has been built for integrated studies of the propagation of radiowaves and the ionosphere by the techniques of PR, CM, PS, VS, ED, and EP, together with IS, and so on. Using this complex, we took the first combined measurements with the PR and IS techniques.

From the nature of radiophysical studies it follows that the propagation of radio waves (theory and experiment) is a vital constituent of this work.

Making numerical calculations of effects that are of independent value and are used in comparing theory with experiment and interpreting the latter requires that working models of the medium and its inhomogeneities be developed and used, along with statistically reliable data on the parameters of the models for characteristic medium states.

The results of integrated radiophysical studies considered in this article embrace all constituent parts: formulation of the theory and techniques of calculating effects, obtaining and analyzing initial ratios used in the measurement techniques, and interpretation of experimental data; developing appropriate models of the medium, building and developing technical facilities for research, developing methods for taking measurements, processing them, and interpreting their results, and taking the

measurements. We present illustrations of some of the most interesting and regional, in our view, results of our investigations.

### 1. Developing a Model of the Ionosphere

By model of the medium we mean a global dependence of its parameters on coordinates and time. The extent of detail and the completeness of the model depend on its purpose. The fullest model is required when developing a theory of the formation, existence, and therefore, for predicting the model and its processes in the medium for other sets of conditions. Complete models of the medium at the present time are developed usually as a result of agreement at scientific conferences of the Committee on Space Research (COSPAR). Such, for example, is the CIRA-65 model (COSPAR International Reference Atmosphere 65 - the year the model was adopted) and the new IRA-70 model being developed. The parameters of neutral and ionized regions of the medium in these models are presented in tabular form for the characteristic medium states obtained by generalizing experimental data. /6

Depending on the precision required, the type of problem, and so on, given simplified, so-called working models of the medium are used in making calculations of the propagation of radio waves. For example, the working models of ionosphere N or USW and SW can differ widely from each other. Thus, in calculating the propagation of USW when the Earth-Space path extends above the maximum of N in the ionosphere region F<sub>2</sub>, details of the lower ionosphere regions need not be taken into account in working models of N. The errors in the calculations of effects for USW that develop are usually within the limits of units of percent.

In 1949-1951 the so-called working parabolically-exponential model of the ionosphere and exosphere was developed [18 19, 20], widely used at present. A particular example of it is in [21]. It agrees with present-day experimental data. The analytic representation of this model is as follows:

$$N(z, x_0, y_0) = N_M \Psi(z, x_0, y_0), \quad (4)$$

where

$$\Psi(z, x_0, y_0) = \begin{cases} 0 & z \leq z_0 \\ \Psi_1(z) = 1 - (z - z_M)^2 z_M^{-2}, & z_0 \leq z \leq z_c \\ \Psi_2(z) = n_c \exp\left(-\int_{z_c}^z \frac{dz}{H_p}\right), & z \gg z_c, \end{cases}$$

$\Psi$  is the so-called shape function (defines the distribution of N over z), z is the instantaneous altitude above the earth's

surface;  $x_0$  and  $y_0$  are fixed horizontal coordinates;  $z_0$ ,  $z_M$ , and  $z_c$  are the altitudes of the lower limit, maximum, and conjugate point of parabola  $\psi_1$  with exponential of  $\psi_2$  of model (4),  $z_m$  is the half-thickness of the parabolic section of  $\psi_1$ , and  $H_p$  is the reduced altitude of the outer ionosphere, determined by the familiar formula:

$$H_p = \frac{T}{\frac{dT}{dz} + \frac{\bar{m}_i g(z)}{2k}}. \quad (5)$$

In (5),  $T = \frac{1}{2}(T_e + T_i)$ ,  $\bar{m}_i$  is the mean-weighted mass of the mixture

of ions in the outer ionosphere,  $g(z)$  is acceleration due to gravity, and  $k$  is the Boltzmann constant. The parameter  $H_p$  increases with altitude  $z$ , which is related to the decrease of  $\bar{m}_i$ , and also related to the increase of  $T$  with altitude. When  $H_p$  is constant in some interval  $z$ , the function  $\psi_2$  takes on the familiar simple form:

$$\psi_2(z) = n_c \exp\left(-\frac{z - z_c}{H_p}\right). \quad (6)$$

The parameters  $z_c$  and  $n_c$  are determined from the condition of conjugation of the functions  $\psi_1$  and  $\psi_2$  in (4) (the functions  $\psi_1$  and  $\psi_2$  are equated to their derivatives in  $z$ ). Thus, for specified  $z_0$ ,  $z_M$ , and  $H_p$ , we get:

$$z_c = z_M - H_p + \sqrt{H_p^2 + z_m^2}, \quad n_c = 2H_p z_m (z_c - z_M). \quad (7)$$

In the actual calculation of the propagation of USW, instead of the variable  $H_p$ , as an extension of model (6) and simplification (4), the outer part of the ionosphere up to altitudes of several thousands of kilometers can be approximated, for  $z > z_c$  with two exponents [1, 21], and up to altitudes of 600-700 km -- by single exponent with constant  $H_p$ . Initially, the model (4, 6) was derived by the author of [18, 19], based on semi-empirical considerations using then-inadequate (1949-1951) data on the outer ionosphere. Importantly, even then the lower-ionosphere  $N_0$  was smaller than for the outer. Later, this model was found to agree with accumulating experimental data. So situations were also encountered when models (4) and (6) were interpreted theoretically with the aid of Eq. (5). Sometimes the exponent (4, 6) commenced directly from the altitude  $z_M$  ( $z_c \simeq z_M$ ). However, this model was not physically realistic ( $dN/dz$  suffers a discontinuity when  $z = z_M$ ), and for small  $H_p z_m^{-1}$ , the value of  $H_p$  can differ widely from its value in (4, 6). To allow for the possible asymmetry of the profiles of  $N(z)$  relative to  $z_M$  in the neighborhood of  $N_M$ , in (6) we can replace  $z_m$  when  $z_M \leq z \leq z_c$  by a larger value than for  $z \leq z_M$ .

A further approximation to the actual situation is including in (6) and (4) the horizontal gradients of the model parameters.

Since the parameter  $N_M$  is usually the most important and subject to the greatest changes, to the first approximation, considering only the gradients of the latter, we can write:

$$N(x, y, z) = N_M(x, y) \psi(z). \quad (8)$$

Typically, in this case the relative horizontal gradient  $\gamma(z)$  does not depend on altitude. Therefore, it can be determined by the VS method for the value  $\gamma_M = \gamma(z_M)$ . The function of  $N_M$  in (8), just like other parameters of the models ( $z_M$ ,  $z_m$ ,  $H_p$ ) can be approximated to any precision from the horizontal coordinates using a broken line.

Two models have been used for the major inhomogeneities of the medium: the quasiundulating and the triaxial ellipsoid, forming or not forming a statistical ensemble along the beam [7, 22, 23, 24].

The parameters of these ionosphere models must be taken from statistically reliable data for the characteristic ionosphere states: depending on the geographical position of the path (for example, middle, high, and low geomagnetic latitudes, polar cap regions, high latitudinal and equatorial depressions), time of the day (day, night, sunrise, sunset, and time of pre-sunset depression), season (winter, summer, and equinox), and solar activity (high, low, and average), with or without the presence of magnetic perturbations in the ionosphere, and so on. The model (4, 6) is not unique.

## 2. Development of the Theory in Calculation of the Effects in the Propagation of Radio Waves. Starting Ratios of Methods of Measurement and Processing of Experimental Data<sup>3</sup>

Various orthogonal coordinate systems were used. One is the rectangular system ( $X_1, X_2, X_3$ ) with its origin at the observation point A (the axis  $X_1$  is directed along the tangent to the beam at A,  $X_2$  -- from A to the atmosphere in the vertical plane, and  $X_3$  is horizontal). Coordinates taken along the beam (length  $s$ ) are related to each other by the equation of the beam. As the independent variables,  $s$  (conveniently for SW) or one of the three coordinates are selected.

From the eikonal equations (EE), using the method of characteristics, one converts to the systems of ordinary differential equations of geometrical optics (SODEGO) equivalent to EE. Further, by the method of iterations, the EE or the SODEGO

---

<sup>3</sup> This problem is examined in more detail in [25, 28] and also in [7, 20, 26, 27].

are solved and working formulas are obtained for the effects described. For specific models of the medium, its inhomogeneities, and the magnetic field, calculations were made by the numerical solution of the SODEGO on an electronic computer. The initial conditions of the SODEGO were specified dually: at observation point A [5, 20, 25, 26, 27] or at the location of the radiator B [5]. The final solutions to the problems of the first and second types naturally must agree, but the approaches and difficulties of calculations differ. The simplicity of obtaining solutions to the SODEGO by iterations depends on the choice of the zero iteration. For example, when the ray is near-linear (for example, USW in the earth's atmosphere and in the interplanetary medium), it is convenient to take as the zero iteration the solution for the homogeneous medium (in particular, the vacuum), and for the SW beam -- the solution for the stratified medium. In subsequent iterations, corrections can be introduced for the horizontal gradients. To obtain the first iteration, the values of the sought-for functions in the zero iteration are substituted in the right side of the SODEGO and the SODEGO is integrated. The subsequent iterations are obtained by repeating the operations described. /8

As a result of solving the SODEGO, two groups of approximate formulas of the effects were obtained [5, 18, 19, 25, 26, 21] of different precision levels: the so-called iteration formulas (I, II, and subsequent iterations) and the formulas of approximations (first, second, and so on). The formulas of approximations were derived from the iteration formulas, leaving in the expansion the sought-for quantities and  $n(1-3)$  in a series in powers of  $\alpha_{0,e}$  and its derivatives in coordinates. Owing to the cumbersome nature of the formulas, let us limit ourselves to the simplest case of quasi-longitudinal and the first high-frequency approximation in  $\alpha$  and  $\alpha b_L$  (3) in the rectangular coordinates  $X_{1,2,3}$ . Allowing for the determination of the effects (see [5, 25, 26]), the following expressions were obtained:

$$\begin{aligned} \Delta R = & -\frac{1}{2} \int_0^R \alpha_{00} dX_1 \pm \int_0^R \alpha_{00} b_L^{(0)} dX_1; \quad \Delta L = \frac{1}{2} \int_0^R \alpha_{00} dX_1 \mp \frac{1}{2} \int_0^R \alpha_{00} b_L^{(0)} dX_1, \\ \Delta \beta, \Delta \varepsilon = & -\frac{1}{2} \int_0^R \alpha_{10,01} \left(1 - \frac{X_1}{R}\right) dX_1 \pm \frac{1}{2} \int_0^R (\alpha b_L)_{10,01} \left(1 - \frac{X_1}{R}\right) dX_1 \mp \\ & \mp \frac{1}{2R} \int_0^R \alpha_{00} b_{L2,3}^{(0)} dX_1, \\ -2c_f^{-1} F_{da} = & v_R \alpha_B + v_B R^{-1} \int_0^R \alpha_{10} X_1 dX_1 + v_e R^{-1} \int_0^R \alpha_{01} dX_1 \pm v_R \alpha_{BB} b_{LB}^0 \pm \\ \pm v_B R^{-1} \int_0^R (\alpha b_L)_{10} X_1 dX_1 \pm v_e R^{-1} \int_0^R (\alpha b_L)_{01} X_1 dX_1 \pm v_B R^{-1} \int_0^R \alpha_{00} b_{T2}^{(0)} dX_1 \pm \end{aligned} \quad (9)$$

$$\begin{aligned}
& \pm v_e R^{-1} \int_0^R \alpha_{00} b_{T3}^{(0)} dX_1 \pm \int_0^R \frac{\partial(\alpha b_L)}{\partial t} dX_1 + \int_0^R \frac{\partial \alpha}{\partial t} dX_1, \\
2cF\phi f^{-1} = & \alpha_B b_{Lb}^{(0)} v_R + v_B R^{-1} \int_0^R (\alpha b_L)_{10} X_1 dX_1 + v_e R^{-1} \int_0^R (\alpha b_L)_{01} X_1 dX_1 + \\
& + v_B R^{-1} \int_0^R \alpha_{01} b_{T2}^{(0)} dX_1 + v_e R^{-1} \int_0^R \alpha_{00} b_{T3}^{(0)} dX_1 + \int_0^R \frac{\partial(\alpha b_L)}{\partial t} dX_1; \Phi = \\
& = \frac{\omega}{2c} \int_0^R \alpha_{00} b_L^{(0)} dX_1.
\end{aligned}$$

Here  $\alpha = \alpha(X_1, X_2, X_3, t)$ ,  $R$  is the distance from the observer A to the radiator B, the subscript B refers to B,  $\alpha_{00} = \alpha(X_1, 0, 0, t)$ ,  $v_{R,B,e}$  is the projection of the velocity of the radiator on R ( $X_1$ ),  $X_2$ , and  $X_3$ , respectively.  $c$  is the speed of light in vacuum,  $\alpha_{10,01} = \partial\alpha/\partial X_{2,3}$  when  $X_{2,3} = 0$ , (similar to  $(\alpha b_L)_{10,01}$ ),  $b_{T,23}$  are the projections onto  $X_{2,3}$  of the quantity  $b_T$ ,  $f_T$  is the Larmor frequency component that is normal to the rectified ray (line AB), the superscript  $0$  refers to the zero iteration (rectified beam); the sign  $\pm$  (or  $+$ ) refers to the ordinary (upper sign) and extraordinary (lower sign) rays. In particular, it is of interest to note that the ratio of the first approximation  $\Delta L = -\Delta R$  known for an isotropic plasma no longer appears in (9). By neglecting the magnetic fields, the resulting ratios transform into the familiar formulas for an isotropic medium [5, 25, 26]. For the "infinitely removed" radiator (including for the case of "astronomical refraction"), it is sufficient to let  $R \rightarrow \infty$  in (9). Recursion ratios were derived, for determining more correctly -- than has usually been done until the present time, at what iteration one must stop in order to obtain the formulas of these effects in any of approximation in  $\alpha$ .

/10

TABLE 1. MAXIMUM RELATIVE ERRORS ( $D_{\max}$ , PERCENT) OF CALCULATION ACCORDING TO THE APPROXIMATE FORMULAS OF THE FIRST APPROXIMATION, ITERATIONS I AND II OF THE EFFECTS  $\Delta\beta$ ,  $\Delta\epsilon$ ,  $\Delta L$ ,  $\Delta R$  FOR VARIOUS ELEVATION ANGLES  $\beta$  AND THE PARAMETER  $b^*$  WITH AND WITHOUT CONSIDERATION OF HORIZONTAL GRADIENTS \* ++

Gradient, $\text{cm}^{-3}$	$b^*$	$\beta^\circ$	Method of calc.	$\gamma_1 = 7,14 \cdot 10^{-4}$ ; $\gamma_2 = \mu_1 = \eta_1 = 0$				$\mu_1 = 1,79 \cdot 10^{-4}$ ; $\gamma_1 = \mu_2 = \eta_1 = 0$				$\gamma_2 = 7,14 \cdot 10^{-4}$ ; $\mu_2 = 7,14 \cdot 10^{-4}$			
				$D_{\max} \Delta\beta, \%$	$D_{\max} \Delta\epsilon, \%$	$D_{\max} \Delta L, \%$	$D_{\max} \Delta R, \%$	$D_{\max} \Delta\beta, \%$	$D_{\max} \Delta\epsilon, \%$	$D_{\max} \Delta L, \%$	$D_{\max} \Delta R, \%$	$D_{\max} \Delta\beta, \%$	$D_{\max} \Delta\epsilon, \%$	$D_{\max} \Delta L, \%$	$D_{\max} \Delta R, \%$
$3,134 \cdot 10^3$	0	(I)**	(I)	2,3	1,0	2,2	7	28,6	2,2	25,6	12	7	12	7	5,2
			(II)	2,1	0,9	2,0	4	18	15	17	17	5,2	7,6	5,2	1,5
		(II)	(I)	0,9	—	—	—	5,7	—	—	—	1,7	1,7	1,7	1,5
			(II)	0,90	0,40	0,85	4,5	19,8	9,2	9,6	9,6	9,5	9,5	9,5	5,1
	20	(I)	(I)	0,85	0,35	0,80	1,0	10	7,0	8,2	8,2	2,4	2,4	2,4	2,0
			(II)	0,50	—	—	—	3,5	—	—	—	0,9	0,9	0,9	0,8
		(II)	(I)	0,40	0,15	0,30	1,2	9,8	5	5,8	3	3	3	3	1,2
			(II)	0,40	0,15	0,30	0,5	4,2	3,6	3,7	1,0	0,6	0,6	0,6	0,5
	45	(I)	(I)	0,2	—	—	—	3	—	—	—	—	—	—	0,5
			(II)	0,2	0,1	0,2	0,6	3,5	2,5	3,0	1	1	1	1	0,5
		(II)	(I)	0,15	0,1	0,2	0,2	2,5	2,0	2,2	0,6	0,6	0,6	0,6	0
			(II)	0,15	—	—	—	1,5	—	—	—	—	—	—	0
	60	(I)	(I)	28	18	24	35,6	28	17,4	25	25	50	31	35	35
			(II)	23	11	19	21	19	11,5	18	18	31	31	24	24
		(II)	(I)	3	—	—	—	4	—	—	—	9,8	9,8	9	9
			(II)	12	5,0	11	25	14,6	6,3	12,2	12,2	37,7	37,7	33	33
0,1	20	(I)	(I)	6	2,0	5	13	4,8	3	5,6	8,4	8,4	8,4	8,1	8,1
			(II)	1,5	—	—	—	30	—	—	—	2,5	2,5	2,5	2,0
		(II)	(I)	7,0	3,3	6,0	6,2	9,2	4	8,1	8,1	19,6	19,6	18,2	18,2
			(II)	3,2	0,5	2,0	2,0	3,1	1,8	4,1	4,1	4,7	4,7	4	4
	45	(I)	(I)	1,0	—	—	—	15	—	—	—	0,6	0,6	0,6	0,2
			(II)	—	—	—	—	—	—	—	—	—	—	—	—
		(II)	(I)	—	—	—	—	—	—	—	—	—	—	—	—
			(II)	—	—	—	—	—	—	—	—	—	—	—	—
	60	(I)	(I)	—	—	—	—	—	—	—	—	—	—	—	—
			(II)	—	—	—	—	—	—	—	—	—	—	—	—
		(II)	(I)	—	—	—	—	—	—	—	—	—	—	—	—
			(II)	—	—	—	—	—	—	—	—	—	—	—	—

\*  $f_0$  is the critical frequency of the F2-region,  $f$  is the frequency of radiation; horizontal gradients:  $\gamma_1, \gamma_2$  is the maximum of the electron concentration NM in the F2-region;  $\mu_{1,3}$  is the altitude of the ionization maximum  $z_M$ ;  $\eta_{1,3}$  is the altitude of the beginning of the  $z_0$  layer in the plane of incidence of the beam (superscript 1) and perpendicular to it (superscript 3). The parameters of the working parabolically-exponential model of the ionosphere in the section above the observation point A:  $z_0 = 180$  km, half-thickness  $z_M = 140$  km, and reduced altitude  $A = 300$  km. \*\* In the parentheses the Arabic numbers denote the approximation, and the Roman numbers denote the iteration.

++ Translator's Note: Commas represent decimal points.



TABLE 2. ABSOLUTE AND RELATIVE CORRECTIONS  $\delta\Delta\beta$  AND  $\delta\Delta R$  FOR THE HORIZONTAL EXTENDED GRADIENTS OF THE ELECTRON CONCENTRATION IN THE IONOSPHERE

Angle of loc. (deg)	Cor-rec-tions	z, km						
		240	320	400	600	800	1000	2000
10	min	10	37	52	51	39	27	-10
	$\delta\Delta\beta\%$	75	88	88	70	52	37	-15
	km	0,8	3,6	6,0	8,8	9,9	10	11
	$\delta\Delta R\%$	65	74	74	70	69	68	67
20	min	3,6	13	18	15	6	-1,6	-25
	$\delta\Delta\beta\%$	37	43	42	28	12	-33	-64
	km	0,3	1,9	3,9	7,3	9,4	11	12
	$\delta\Delta R\%$	42	58	66	78	85	90	96
45	min	0,7	1,8	1,6	-1,2	-4,7	-7,4	-16
	$\delta\Delta\beta\%$	15	12	8	-6	-23	-39	-127
	km	0,1	0,4	0,8	1,6	2,1	2,5	2,9
	$\delta\Delta R\%$	16	20	23	28	32	34	38
60	min	0,1	0,1	-0,4	-3,0	-5,4	-7,4	-13
	$\delta\Delta\beta\%$	8	2	-4	-23	-45	-69	-186
	km	0,003	0,2	0,4	0,8	1,0	1,2	1,4
	$\delta\Delta R\%$	9	12	13	16	18	20	22

The ionosphere parameters are the same as in Table 1:  $b^2 = 2.82 \cdot 10^{-2}$ ,  $\gamma = 7.14 \cdot 10^{-4} \text{ km}^{-1}$ . The values of the corrections are absolute and are expressed in percentages of the values of the effects for a stratified atmosphere.

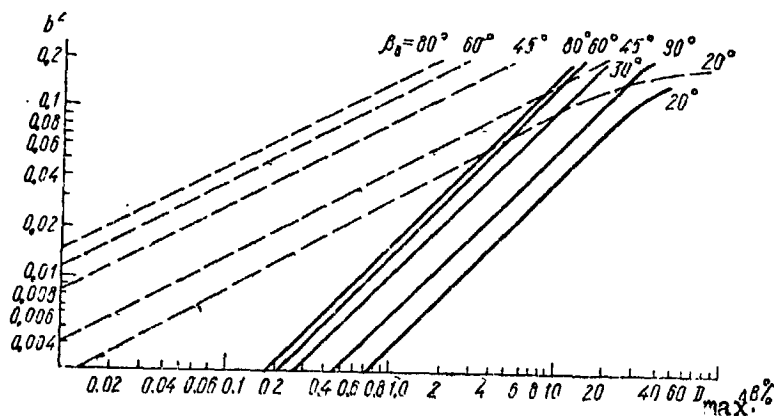


Fig. 1. Dependence on  $b^2$  of the maximum relative error  $D_{\max} \Delta\beta$  of the calculation of the vertical refraction  $\Delta\beta$  by the formulas of the first (—) and (---) approximations for different elevation angles of the ray  $\beta_A$  (see the ionosphere model in the remark to Table 1).

The errors of these derived approximate formulas are determined by comparing the calculation of the effects according to them with an exact calculation by a numerical solution of the SODEGO on an electronic computer, and also by comparison with data of measurements taken under the same (or similar) conditions (Tables 1 and 2; Figures 1 and 2,

and also [13, 12]). The errors of the formulas of the first and second approximations and the range of applicability for a spherically stratified ionosphere are illustrated for refraction (similarly for other effects) (Fig. 1). We can see that the errors of formulas of the first approximation become appreciable when  $b^2 \geq 0.1$  and  $\beta_A \leq 30^\circ$ . This trend can also be traced in the dependence of  $\Delta\beta$  on the coordinates calculated by the formula of the first approximation and iteration I and "exactly" by the solution to the SODEGO (Fig. 2). Here, the large decrease of  $\Delta\beta$  and the errors of the calculation based on these formulas, with increase in  $\beta_A$ , is typical. The presence of positive gradients of  $\gamma_1$  and  $\mu_1$  (Table 2) leads to a decrease (and in the case of positive gradients -- to an increase) in the calculation precision, presented in Table 2, of effects both according to the formulas of the first approximations as well as those in iteration I compared with the calculation for the stratified ionosphere. Even for a relatively small  $b^2$  ( $b^2 = 3.134 \cdot 10^{-3}$ ), the errors according to formulas of the first approximation and iteration I, when horizontal gradients are present, can sometimes exceed by more than one order of magnitude the errors of the formulas for the stratified ionosphere. For a large incoming ray angle  $\beta_A$  ( $\beta_A \approx 45^\circ$ ), the formulas under the first approximation and iteration I (even when horizontal gradients are present) give a relative error  $\leq 5$  percent for  $b^2 \sim 10^{-3}$  and  $\leq 10$  percent for  $b^2 \sim 10^{-1}$ .

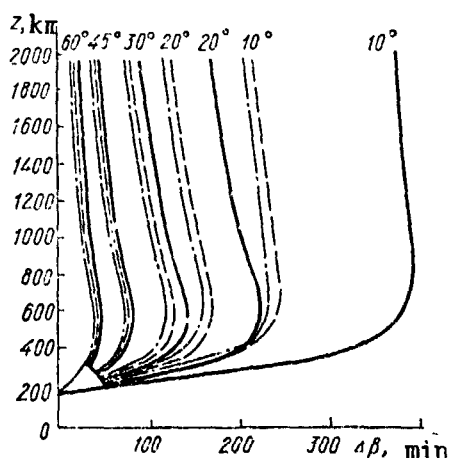


Fig. 2. Dependence on altitude  $z$  (km) of the vertical refraction  $\Delta\beta$  (angular minutes) for different beam elevation angles  $\beta_A$  obtained by exact calculation by [Continued on following page] Fig. 2.

It was found that the role of the terms in effect formulas of higher order relative to  $\alpha$  for inhomogeneities is greater than for the formulas presented in Figs. 1 and 2 and in Table 1 for regular ionosphere models. Exact and approximate formulas of these effects for the stratified ionosphere reduce to quadratures. They were also obtained and analyzed in [29]. Of interest is the fact that ionospheric refraction  $\Delta\beta$  as the function of the elevation angle  $\beta_B$  for a finitely removed irradiator reaches a maximum not at  $\beta_B = 0$ , but for the infinitely removed irradiator -- at  $\beta_B = 0$ , and also of interest is the principle that at some finite altitude for a fixed  $\beta_B \neq 0$  the refraction reaches the maximum. This can be seen in

[Continuation of Fig. 2  
on preceding page]

solving SODEGO on an electronic computer (\_\_\_\_) and by calculation according to formulas of the first approximation (\_\_\_\_) and in the first iteration without allowing for horizontal gradients (cf. parameters of the working model of the ionosphere in the remark to Table 1).

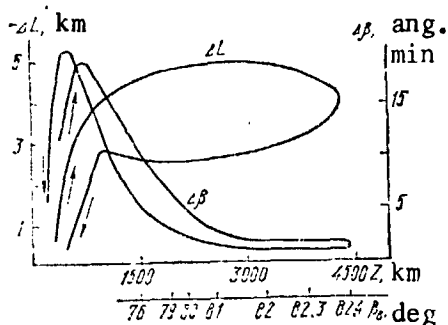


Fig. 3. Dependence of the vertical refractive  $\Delta\beta$  (angular minutes) and phase lag  $\Delta L$  (km) on altitude  $Z$  (km), and the elevation angle  $\beta_B$  (deg) in an ascent ( $\uparrow$ ) and descent ( $\downarrow$ ) of a VSP [13, 5] that the frequency 48 MHz. The time of the experiment was 12 October 1967 from 18:15 to 19:07, local time.

rapid rise in the elevation angle of the VSP and agree closely with calculated data.

These theoretical and experimental studies of the errors in the approximate formulas made it possible to develop universal plots that are convenient for practical use [20] (for example, for the isotropic plasma they are virtually independent of the parameter  $b^2$ ) and permitted the determination of their range of applicability.

In an integrated experiment [13, 12] using rocket (VSP) simultaneously with several techniques (EP, ED, IS, and VS), these effects were measured along with the vertical profiles of the ionosphere parameters for the first time with allowance for their horizontal gradients and transients for virtually the entire range of the elevation angles and up to the altitude  $\sim 4000$  km. Here, incidentally, for the first time it was possible to solve the difficult problem of allowing for the horizontal gradients in the determination of the effects [5].

To illustrate, Fig. 3 presents the experimental dependences of  $\Delta\beta$  and  $\Delta L$  on altitude  $z$  and elevation angle  $\beta_B$  (VSP). The nonuniqueness of the values of  $\Delta\beta$  and  $\Delta L$  in the ascent and descent of VSP is accounted for by the nonsteady state nature of the medium in the transitional time of the day. A well-defined sharp maximum of  $\Delta\beta$  at the altitude  $\sim 650$  km as  $\beta_B \sim 30^\circ$  and the strong decrease in  $\Delta\beta$  with increase in altitude are caused by the

/12

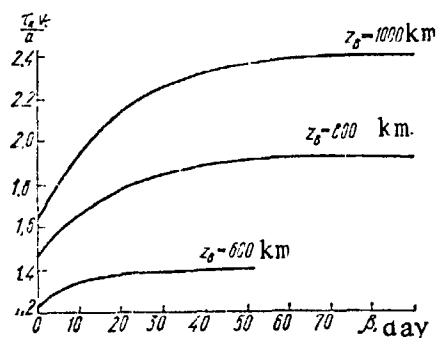


Fig. 4. Dependence of the correlation interval  $\tau_{CF}$  of fluctuations in the Faraday angle on the satellite elevation angle  $\beta$  for fixed altitudes  $z$  ( $(v_T \tau_{CF})/a$  is a dimensionless parameter,  $v_T$  is the velocity of the AES transverse to the beam, and  $a$  is the size of the inhomogeneities along  $v_T$ ). When  $\beta \geq 20-30^\circ$ , the parameter of  $(v_T \tau_{CF})/a$  is virtually independent of  $\beta$ .

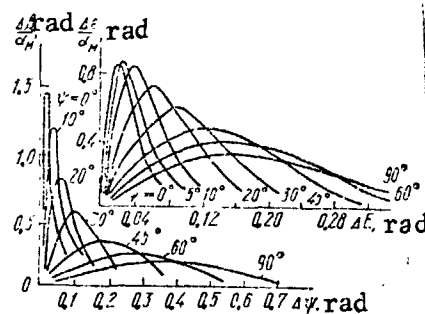


Fig. 5. Dependence of the local-angular  $\Delta\beta$  and lateral  $\Delta\epsilon$  refractions on the local angle  $\beta_B$  ( $\Delta\psi = \psi - \beta_B$ ) and azimuth  $\epsilon_B$  ( $\Delta\epsilon = \epsilon - \epsilon_B$ ) of an irradiator due to ellipsoidal inhomogeneity for a fixed azimuth and several angles of the location sign of the inhomogeneity center. The altitude of the inhomogeneity is 300 km, the horizontal distance is 120 km, the frequency is 20 MHz, the concentration in the inhomogeneity center  $N_M = 10^5$  electrons. $\text{cm}^{-3}$  ( $\alpha_M = 8.07f^{-2} N_M$ , where  $f$  is in MHz, and  $N_M$  is in  $10^5$  electron. $\text{cm}^{-3}$ ). The height of the irradiator was 1000 km.

Detailed studies were made of the effect of horizontal gradients ( $\gamma_i, \mu_i, \eta_i$ ) of the main ionosphere parameters ( $N_M, z_M, z_0$ ) and the geomagnetic field ( $\vec{H}$ ) on the effects described in the propagation of SW [5, 25, 27] and USW [25, 27]. The effect of elongated horizontal gradients  $\gamma_1$  on the propagation of USW is illustrated by Table 2. The allowance for magnetic field in the calculations of the effects is appreciable in several cases. Thus,  $\Delta\beta$  and  $\Delta L$  obtained with and without allowance for  $H$  at the altitude of ionization maximum when  $\beta_B \approx 10^\circ$  for  $f = 20$  MHz can differ by 25 percent. At other elevations and for  $\beta_B > 10^\circ$ , this difference becomes less. It was found that in order of decreasing influence on the effects, we have: horizontal gradients of the critical frequency ( $\gamma_i$ ), gradients of geometrical parameters of the ionosphere models ( $\mu_i, \eta_i$ ), major inhomogeneities, and geomagnetic fields.

Interest in sporadic components of the effects and in the inhomogeneities of the medium has grown in the course of time. There are inadequate experimental data on their statistical characteristics. We derived formulas for coupling statistical characteristics of fluctuations in effects (dispersion D and correlation functions K) with the parameters of ionosphere inhomogeneities, with which the latter could be determined based on recordings of sporadic components of the effects (ED and EP) [5, 28]. From data of a calculation made of the dispersion of effects for a statistically inhomogeneous region in the form of several statistically homogeneous layers, the dispersions were found equal to the sum of the dispersions due to each layer if the interval of the correlation of fluctuations in N in each layer is somewhat smaller than its thickness.

/13

Similarly, from the coupling of the correlation functions of the fluctuations of effects and of N, it was possible over the experimental time interval of the correlation of effects  $\tau_K$  to determine the inhomogeneity dimensions [16]. Fig. 4 shows this possibility when  $\beta \geq 30^\circ$ .

Major isolated inhomogeneities can be encountered in the atmosphere, including also artificial inhomogeneities, when the statistical approach to analyzing effects caused by these inhomogeneities is inapplicable [2, 5, 23, 20]. Fig. 5 illustrates the calculation of the local-angular  $\Delta\beta$  and lateral  $\Delta\epsilon$  refractions for a "fine" ellipsoidal inhomogeneity for different local angles  $\psi$  of its center. Typical of the Doppler frequency shift  $F_d$  are the large values of  $|F_d|$  if the irradiator is within the inhomogeneity. More detailed calculations of the effects for undulating inhomogeneities are given in [22, 24], and for ellipsoidal -- in [22, 24].

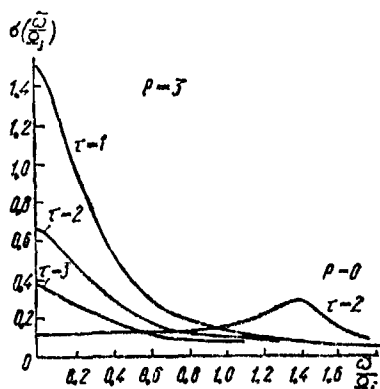


Fig. 6. Spectrum of incoherent scattering for various ratios  $\tau = T_e/T_i$  of electronic and ionic temperatures [Continued on following page]

Owing to advances in experimental IS methods, it became necessary to develop the theoretical basis [5, 28]. The effect of collisions on the spectrum  $\sigma(\omega)$  and the integrated diameter  $\sigma$  of incoherent scattering were examined. In contrast to earlier studies, the problem was solved on the general assumptions, with allowance for the magnetic field, and without employing the Nyquist theorem that is debatable for use in ionospheric conditions. Fig. 6 illustrates the effect of  $\nu$  on  $\sigma(\omega)$ . Clearly,  $\sigma(\omega)$ , with allowance for collisions, is much narrower than in the collisionless case in which

[Continuation of Fig. 6 on preceding page] and various values of the collision parameter  $P = \nu/\Omega_i = 3$  ( $P = 0$ , collisionless case)

there is no "peak" at the frequency  $\Omega_i$  of the ionoacoustic waves, which hampers the use of the ordinary technique of spectral interpretation. However, even in this case from the shape of the spectrum one can estimate  $T_e$ ,  $T_i$ ,  $\nu$ , and  $N$  [28].

The studies [5, 28] also examine a function appearing in  $\sigma(\omega)$  and caused by the intrinsic oscillations of ions (including gyroresonance). It was shown that in the D and E layers ( $\nu \gg \Omega_i$ ), the magnetic field weakly affects this function, and therefore, gyroresonances disappear even in transverse propagation. A calculation was made of  $\sigma(\omega)$  for the nonmaxwellian function of the distribution of electrons by velocity. Preliminary "heating" of the atmosphere leading to a different distribution function is evident only when there is a significant excess of the Debye radius  $d$  over  $\lambda$ , and in the case of practical importance  $\lambda \gg d$ , the "peak" in  $\sigma(\omega)$  increases only at a frequency  $\Omega_i$ . At the same time, signals appear at the combination frequencies  $\omega_k = \omega_1 \pm \omega_2$ , where  $\omega_{1,2}$  are the frequencies of the "warming" and sounding fields, respectively. In this case,  $\sigma$  in the Born approximation at the frequency  $\omega_k$  depends [7, 28] on the relative orientation of the electric field of vectors of the "warming" and sounding radio waves and is proportional to the plasma gradient  $\epsilon$ .

### 3. Illustrations of Measurements and Comparison With Theory

In measurements at widely scattered points using EP and ED of coherent signals from vertically travelling rockets, it was possible to obtain and taken to consideration the profiles of horizontal gradients and transients of  $N$  and  $N_0$ , and also the magnetic field inhomogeneity, sphericity of the earth, and when necessary, also the curvature of rays [1, 7, 13, 12]. The corresponding profiles of  $N_0$ ,  $N$ ,  $\partial N_0/\partial t$ ,  $\eta_0$ , and  $\gamma_0$ , that we obtained up to great altitudes ( $\approx 4500$  km) are in [5, 13, 12]. Evidently, for the first time measurements of  $\Delta\beta$  and  $\Delta L$  over wide range of angles  $\beta_E$  and altitudes is illustrated by Fig. 3 from [5], with allowance for horizontal gradients and transients.

/14

In satellite measurements, transients cannot be taken into account up to sufficiently high altitudes [21, 1] or a correction can be introduced in approximate terms for it from experimental data [1, 13, 10, 30, 12].

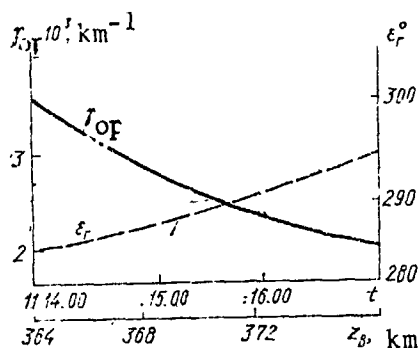


Fig. 7. Time function of the pass of the Kosmos-321 satellite (26 February 1970) of the total relative horizontal gradient  $\gamma_{op}$  (—) and azimuth  $\epsilon_r$  (---) in the ML

Our satellite measurements of total relative horizontal gradients of  $N_0$  (the quantity  $\gamma_{op}$  and azimuth  $\epsilon_r$ ) at middle and upper latitudes [5, 13, 15, 31], carried out through the availability of widely scattered observation points, are essentially the first that are as complete and integrated. These measurements in EP and ED also open up the possibilities of obtaining statistical characteristics of effect fluctuations,  $N_L$  and  $N$  [1, 5, 7, 13, 16, 32, 33]. Figs. 7-9 show the dependence of  $\gamma_{op}$  (its magnitude and the azimuth  $\epsilon_r$ ) on the orbital pass time of the AES in the ML (Fig. 7), the relative gradient  $\gamma_0$  in the direction of the satel-

lite's pass in the HL (Fig. 8), and the mean-monthly relative longitudinal gradient as a function of the time of day (morning) in the ML (Fig. 9). Evidently, these data can be regarded as typical and we can generalize it as follows: in the ML, in the daytime  $\gamma_{op} \lesssim 5 \cdot 10^{-3} \text{ km}^{-1}$  and is directed approximately northwest; at night it is approximately one order of magnitude less and has no specific direction. In the HL, at night a  $\gamma_{op} \simeq (1-3) \cdot 10^{-3} \text{ km}^{-1}$ . It was found (in particular, in spring of 1970) that during the sunrise in the ML the direction of  $\gamma_{op}$  changes from southwest (at 5:00 local time) to the southeast (at 7:00) and again approaches the southwest at 9:00. The gradient  $\gamma_0$  along the satellite orbit in the HL change from  $3 \cdot 10^{-3} \text{ km}^{-1}$  (the flight was approximately west to east) to  $1 \cdot 10^{-3} \text{ km}^{-1}$  (flight to southeast). An individual case, anomalously large gradients were observed in the HL (for example,  $1.5 \cdot 10^{-2} \text{ km}^{-1}$ ). The longitudinal gradient  $\gamma_{0l}$ , which is at an extremum in the transitional time of the day, can in the seasonal and cyclic trend change in the ML by approximately one order -- from  $(1-5) \cdot 10^{-3}$  to  $(2-4) \cdot 10^{-4} \text{ km}^{-1}$ , and less, in the HL. The latitudinal gradient is smaller than the longitudinal; it is smaller in the ML than in the HL; it is observed at any time of the day; and from night to day in the ML it changes from  $(1-2) \cdot 10^{-4}$  to  $(5-7) \cdot 10^{-4} \text{ km}^{-1}$ . The gradients  $dN_L/ds$ , measured with a high precision by the differential ED technique made it possible to trace quite subtle changes in  $N_L$ , (including long-scale quasiundulating and cloud formations) and to obtain the statistical characteristics [1, 13, 15, 34, 11].

Diurnal and seasonal dependences of  $N_0$ , which we obtained during the cycle of solar activity (SA) in the ML and HL of both

hemispheres from EP and ED signals of the AES, and also most completely in the ML at a high SA by the IS technique are described in [5, 15, 13, 14, 35]. We agree with the data of other reliable investigations. In particular,  $N_0$  in the ML at equinox was much larger than during the summer [15]. Latitudinal depressions of  $N_0$ , and their diurnal shifts in the HL and ML were reliably traced. The depressions evidently account for, first of all, the nonmonotonicity in the inclined profiles of  $N$  first reliably traced by Ya. L. Al'pert and ourselves, obtained by satellite measurements using the EP and ED techniques. To obtain approximate values of  $N$  along the orbit of the AES, we developed the so-called method of the equation chain proposed by Ya. L. Al'pert -- see [1] -- [21] (the necessary and sufficient conditions were derived and verified theoretically and experimentally). Also developed was a method of determining  $N$  in satellite and rocket measurements by solving equations of the Volterra type relating the frequencies  $F_{da}$  and  $F$  with  $N$  [36, 5, 7, 15].

/15

To increase the precision of measurements based on EP and ED, the components of EP and ED were investigated at three and four frequencies experimentally and theoretically, along with other effects proportional to  $f^{-1}$ ,  $f^{-2}$ ,  $f^{-3}$ , and  $f^{-4}$  [15, 31, 26, 20, 5, 25]. It was shown concretely that for reliability and a considerable rise in the precision of measurements, at low coherent frequencies (for example, 20, 30, and 40 MHz) the difference ED technique must be used at three and more frequencies or, by limiting oneself to a single pair of frequencies, one must convert to higher frequencies, taking some special measures to preserve the high resolving power of the techniques in so doing [37].

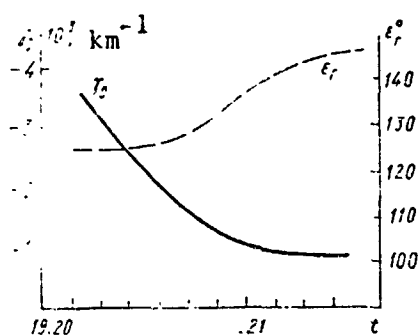


Fig. 8. Relative horizontal gradient  $\gamma_0$  in the direction of flight (azimuth  $\epsilon$ ), obtained from recordings of EP at Arkhangel'sk and Murmansk ( $z_B = 330$  km) as functions of the orbital pass time of the Kosmos-21 satellite (1 February 1970)

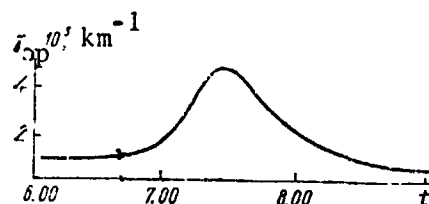


Fig. 9. Gradient  $\gamma_{01}$  of the night electron concentration beneath the satellite (altitude  $\gamma_{01}$  1000-1300 km) in the ML (we illustrate the maximum of  $\gamma_{01}$  ( $\approx 6 \cdot 10^{-3}$  km $^{-1}$ ) in the region of the sunrise (7:30)) as a function of the orbital pass time of the explorer-27 satellite (March 1970)



Quite full measurements of  $\Delta\beta$  and  $\Delta L$  were similarly published in [1, 5, 10, 13, 15, 31, 38, 11]. Typical of the dependences of  $\Delta\beta$  and  $\Delta L$  in individual satellite passes in the HL is the weak (compared with the ML [13]) asymmetry of these curves relative to the parameter point of the satellites [15], indicating the smaller effect of the horizontal gradients on these measurements in the HL than in the ML.

Of the quantitative studies during the SA cycle of statistical characteristics (dispersions and correlation functions C) of the fluctuations in  $N_L$ , N, and in effects for propagation in the ML and the UL, using AES (noted in the introduction), the following were most reliably traced [5, 13, 16]:

1) elongation of the major ionosphere inhomogeneities in the direction "north-south" (the most probable dimensions of the inhomogeneities in the "north-south" direction during the solar cycle in the day is 170 km, at night -- 130 km, in the "west-east" direction in the day -- 120 km, and at night -- 90 km);

2) seasonal and diurnal functions of inhomogeneity characteristics;

3) intensified (especially when perturbations were present) nonregularity of the ionosphere in the HL compared with the ML. (In the HL the correlation intervals  $\tau_k$  are smaller, and the relative fluctuations in N,  $dN_L/ds$ , and  $N_0$  are greater than in the ML, therefore the random gradients in the HL are larger, but the dimensions are smaller than in the ML (Fig. 10); and

4) a possibility of approximating the normalized autocorrelation function  $R(\tau)$  of fluctuations in  $N_L$  when they pass through zero in the form  $R(\tau) = \cos \gamma \tau \exp(-\alpha \tau)$  [5, 13, 16, 32] and more exactly, especially near zero -- in the gaussian form (the probable values of the parameters  $\gamma$  and  $\alpha$  were determined for characteristic ionosphere states in the HL and ML) [5, 6].

16

Measurements by the IS technique first begun by us in the USSR [2, 3, 4, 5, 7] have been steadily improved; their precision has been increased and the scope of studies has been expanded [6, 35, 30, 40]. Errors in measurements of regular N and  $N_L$  are usually of the order of units of percent in the altitude range 150-700 km, while the errors in the measurement of temperature and ion composition are of the order of tenths of percent and higher -- outside this range. But for the measurement of irregularities of these parameters, the requirements imposed on the characteristics of IS facilities have been much increased. The appropriate recommendations have been developed for this purpose in [5, 40, 41] and are noted in [6].

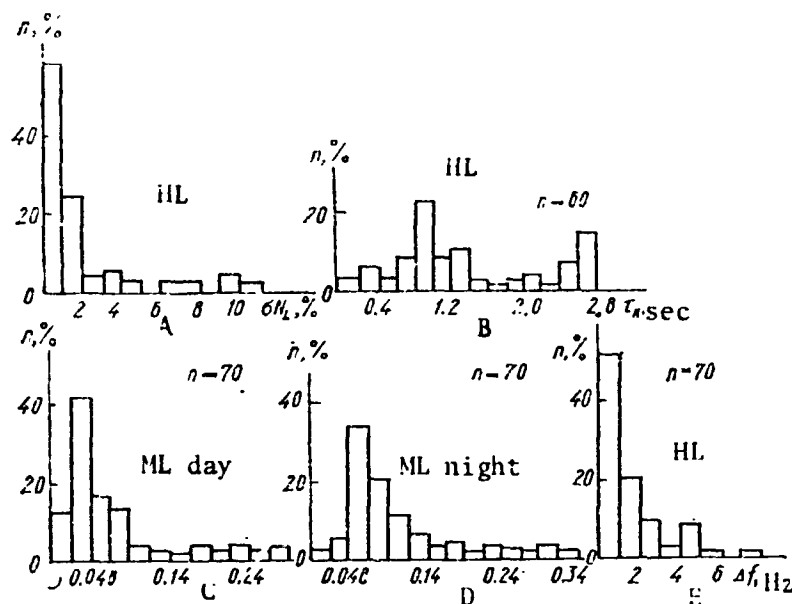


Fig. 10. Histograms of root mean square relative values of  $\sigma_{N_L}$  and time intervals

of the correlation  $\tau_C$  of fluctuations in  $N_L$  in the range of small scales and frequency bands  $\Delta f$  (Hz) of the energy spectra  $\delta N_L$  for the middle and high latitudes (A -- for  $\sigma_{N_L}$ , B -- for  $\tau_C$  in the HL; C and D -- frequency bands of the energy spectra  $\delta N_L$  for day and night, respectively, in the ML, and E -- as above for the region of polar lights in a period of strong disturbances)

grated ionospheric measurements using different radiophysical techniques, including IS, is presented in [4, 5, 6, 12, 13], and measurements in the same region using different IS facilities simultaneously have thus far been conducted only by ourselves [35].

As a result of systematic measurements (several days in each season since 1965), functions of  $T_e$ ,  $T_i$ ,  $\tau = T_e/T_i$ ,  $N$ ,  $N_0$ , and  $N_L$  have been obtained (evidently, the only ones in the USSR), as well as altitude-time functions of  $\Delta L$  and  $\Delta \beta$  for different seasons at higher and moderate SA. The simultaneity of the measurements throughout the region of the near-earth plasma described makes them especially valuable for analyzing physical processes in the ionization and temperature balances, as well as the dynamics of the atmosphere as a whole [2, 8, 5,

These studies by the IS technique began to be integrated in themselves; they are conducted with different facilities with different spatial and time resolution and with different nature of operation and in total embrace altitudes from 60 to 1000 to 1200 km. It has been possible to episodically obtain the details of the profiles of  $N$  in the D-, E-,  $E_s$ -,  $E_1$ -, and  $E_2$ - regions and in the "valley" between these regions, and also to investigate major ionospheric inhomogeneities and their motion [31, 40]. One of the two known [2, 8, 4] inte-

7, 13, 4, 35, 39, 40, 41]. Fig. 11 illustrates the diversity of the profiles we obtained for  $N$ ,  $T_e$ ,  $T_i$ , and  $\tau$  by the IS technique where different seasons and characteristic times of the day. In the profile of  $T_e$ , here the presence of a maximum in altitude, which can be  $\lesssim 3000^\circ \text{K}$  during the day, is typical of high SA. It is most strongly evident in the morning and lies somewhat lower than the maximum of  $N_{MF2}$ , decreases with time, and by evening lies in the vicinity of the maximum  $N$ , even higher, which agrees qualitatively with the theory of the thermal balance of the atmosphere. The maxima of  $T_e$  can vary with time quite rapidly (the initiation and disappearance of a maximum can appear in 10 minutes). The maximum  $T_e$  in our experiments, prepared with other measurements at the ML (France, United States), shows up more distinctly and more often. The cyclic change of  $T_e$  in F2 (in contrast to  $N$ , is not clearly evident, which is related to the characteristics of the thermal balance (the increase in  $N$  in some time interval correlates with the decrease of  $T_e$ ). At the same time, with stronger SA  $T_i$  increases relatively more strongly.

/17

The temperature equilibrium ( $T_e \simeq T_i$ ) is attained usually approximately at the elevation  $\sim 500$ - $700$  km. However, not infrequent are cases (not only in sunset or sunrise) when in the altitude interval in which the spectra are measured ( $\leq 700$  km), in the day the temperature equilibrium cannot be established. At night, as a rule, the ratio  $\tau = T_e/T_i$  is not unity; its maximum value can be 1.2-1.5 and as high as 1.8. In summer (31 July to 1 August 1969), an increase of  $\tau$  from 1 to 2 three hours before sunset was observed. This cannot be explained by the transfer of photoelectrons from the magnetically conjugate region (here the sunset occurs much later than in the region of measurement). At equinox this effect is more weakly manifested. In the diurnal trend of  $\tau_{\max}$ , a tendency of a change in  $\tau_{\max}$  in the "counter-phase" with the altitude of  $\tau_{\max}$  and with the altitude of the ionization maximum [35].

/18

The IS method, in contrast to satellite measurements, can easily obtain  $N_0$  values as a function of time up to any fixed altitude in the measurement interval and trace several interesting effects [35]. Thus, in the diurnal dependence, at the spring equinox (1969), at sunset  $N_0$  even increases somewhat up to altitudes in the vicinity of the ionization maximum, with time, but decreases at greater altitudes, which indicates a certain diffuse "streaming" of electrons in the region of increasing  $N_0$ . At night and before sunrise, the increase of  $N$  at different altitudes causes a corresponding increase in  $N_0$  up to these altitudes. Variations in  $N_0$  from day to day are observed, by a factor 1.5.

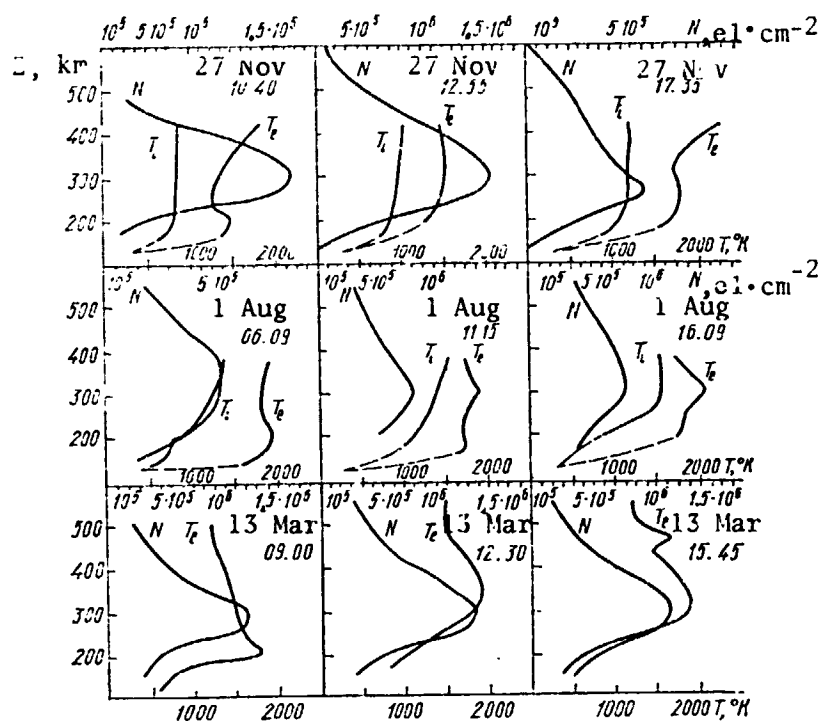


Fig. 11. Examples of diversity of the profiles of  $N$ ,  $T_e$ , and  $T_i$  obtained by the autumn - winter (27 November), summer (31 July - 7 May [sic]), spring (13 March), and time of day: local morning, midday, and evening.

to night in order of magnitude from 10 to 2  $\text{deg} \cdot \text{km}^{-1}$ . At greater altitudes (500-600 km), the gradient  $\partial T_e / \partial z$  is constant during the day and on the average approximately 2  $\text{deg} \cdot \text{km}^{-1}$ , which indicates the existence of a stream of electrons from the magnetosphere. The gradient of  $\partial T_i / \partial z$  in the altitude trend is positive with a mean of the order of 2  $\text{deg} \cdot \text{km}^{-1}$  in the 200-600 km interval. Sometimes, at altitudes of 200-300 km isothermicity of  $T_i$  is observed.

From the measurements by IS technique of quantities appearing in the ionization and heat balances, the parameters of micro-processes of the latter were investigated and determined [5, 6, 7, 39]. In the period of the 24 September 1968 solar eclipse, from measurements of  $N$ ,  $\partial N / \partial t$ ,  $N_0$ ,  $T_e$ , and  $T_i$ , using known models of the neutral atmosphere and the calculated function of solar eclipse, vertical profiles of the characteristics of electron diffusion  $D$  ( $D = \text{div } Nv$ ,  $v$  is the rate of diffusion),

The transiency of  $\partial N / \partial t$  in the diurnal course and also in altitude can have an extreme (up to ten electrons per  $\text{cm}^3 \cdot \text{sec}^{-1}$ ). The transiency and vertical gradients of  $T_e$  compared with  $T_i$  are subject to stronger and more complicated changes. At all times of the day (except at night)  $\partial T / \partial t$  has characteristic extrema, reaching a value of the order  $10^{-1} \text{ deg} \cdot \text{sec}^{-2}$ , and the profile of the relative transiency  $\eta_e$  disclose extrema of the order of  $10^{-4} \text{ km}^{-1}$  only in the transition of time. The profiles of  $\partial T_i / \partial t$  are analogous (their extrema are smaller). The maximum values of the vertical gradients of  $\partial T_e / \partial z$  are attained usually below the ionization maximum, decreasing from day

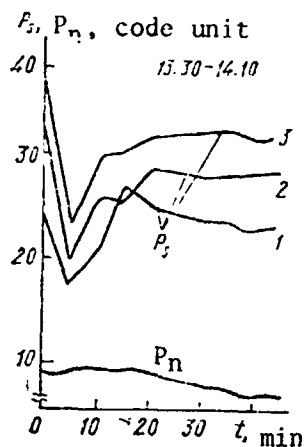


Fig. 12. Simultaneous measurements on 26 February 1969 (13:30 - 14:10) of the noise intensity  $P_n$  and scattering intensity  $P_s$  by the IS technique (in units of code). The strobes for 40 minutes were placed at the altitudes of 105 (1), 110 (2), and 115 (3) km. A flaw  $P_s$  was detected that was not observed in  $P_n$ ; therefore, it is of ionospheric origin.

intensity of ion formation  $q$ , and effective coefficient of streaming  $\beta$  (allowing for D and  $q$ ) were determined for the low and outer ionosphere. It was found that the predominant effect of the eclipse was the relatively high temperature changes in these characteristics.  $N_M$  shows virtually no change, but  $N_0$  changes appreciably (with a lag in the minimum relative to the maximum phase of the eclipse), indicating the major role of diffusion and transport in the ionization and heat balances in most of the ionosphere.

IS measurements of the fine structure of the lower ionosphere regions, its inhomogeneities and motions are generally scanty. Our measurements (especially in the D-region) [5] are among the first. Characteristics, possibilities, and difficulties have been analyzed, as well as the requirements imposed on IS facilities for these measurements [5, 13, 40] and illustrations of the latter have been presented [5, 40]. Fig. 12 shows the initiation of a burst in the scattering intensity  $P_s$  owing to a shifting type  $E_s$  inhomogeneity. At the velocity and direction of inhomogeneity drift anticipated in the experimental conditions ( $v_0 \approx 40$  m·sec<sup>-1</sup>, west to east), the dimensions of the inhomogeneity were estimated from the period of fluctuations  $P_s$ : horizontal -- 14-24, and vertical -- 5-10 km.

The principal interfering factor of a theoretical major in measuring inhomogeneities by the IS technique is the partially coherent component  $P_s$  deriving from scattering by small nonthermal plasma fluctuations and medium turbulences, and also the neglected influence of collisions, etc. Here also serious instrumental difficulties arise. The following recommended characteristics of the IS facilities were established [5, 6, 31]: range -- the short-wave section of the decimeter wavelength range, special resolutions -- hundreds of meters, and units of minutes, and smaller; and impulse intensity -- tens of megawatts and stronger. For a complete correlational analysis, the use of multibeam and multibase facilities is most radical [sic].

From EP signals reflected from the Moon, in 1962-1966 investigations [13, 18-19], the rate  $dN_0/dt$  of the change in  $N_0$  between the Moon and the Earth and the mean electron concentration  $\bar{N}$  in the interplanetary space (between the ionosphere of the Earth and the Moon) were determined. At the possible limits to the values of  $N_0$  from Earth up to 20,000 km (from  $10^{13}$  to  $6 \cdot 10^{13}$  electrons. $\text{cm}^{-2}$ ), the values of  $\bar{N}$  at night in March-April 1966 vary from units to tens of electrons per  $\text{cm}^3$ , and the maximum value of  $\partial N_0/\partial t$  reached  $5 \cdot 10^8 \text{ cm}^{-2} \text{ sec}^{-1}$ .

# REFERENCES

1. Misyura, V. A., in the collection: Ionosfernyye issledovaniya (Ionospheric Research), No. 18, 120-135 (1969).
2. Misyura, V. A. et al., in the collection: Ionosfernyye issledovaniya, No. 18, 136-163 (1969); No. 20, 85-93 (1972); No. 21, 80-89, 93-103 (1972).
3. Misyura, V. A., Tkachev, G. N., Yerokhin, Yu. G., et al., in the collection: Geomagnetizm i aeronomiya (Geomagnetism and Aeronomy), 7(2), 535 (1967); 9(1), 75 (1969).
4. Misyura, V. A. et al., in the collection: Kosmicheskiye issledovaniya (Space Research), 6(7), 726 (1969).
5. Misyura, V. A. et al., in the collection: IX Vsesoyuznaya konferentsiya po rasprostraneniyu radiovoln. Avtoreferaty dokladov (Ninth All-Union Conference on the Propagation of Radio Waves, Authors' Abstracts of Papers), Parts I and II, published by the USSR and Ukrainian SSR Academies of Sciences, 1969.
6. Misyura, V. A., Yerokhin, Yu. G., et al., "Ionosphere of Middle Latitudes From Incoherent Scattering Studies," Doklad na XIII sessii Kospar (Paper at the 13th Session of COSPAR), Leningrad, 1970 -- in the collection: Space Research, No. 11, 1027-1038 (1971).
7. Misyura, V. A. et al., in the collection: Tezisy dokladov yubileynoy nauchno-tekhnicheskoy konferentsii (Abstracts of Papers Presented at the Anniversary Scientific-Technical Conference), Radiophysical Department of Khar'kov State University, 1970.
8. Evans, J. V., Proc. IEEE, 57(4), 469-530 (1969).
9. Misyura, V. A. et al., in the collection: Kosmicheskiye issledovaniya, 3(4), 64 (1965).
10. Misyura, V. A., Krokhmal'nikov, Ye. B., Zinchenko, G. N., et al., in the collection: Geomagnetizm i aeronomiya, 10(2), 244 (1970).
11. Misyura, V. A. et al., in the collection: Issledovaniye kosmicheskogo prostranstva (Studies of Space), "Nauka", Moscow, 1965, p. 136.

12. Misyura, V. A., in the collection: Geomagnetizm i aeronomiya, 9(3), 453 (1969).
13. Misyura, V. A. et al., "Results of Radiophysical Ionospheric Studies During the Solar Cycle on the Propagation of Radio Waves From Space Objects," Doklad na XIII sessii Kospar, Leningrad, 1970.
14. Misyura, V. A., Solodovnikov, G. K., and Migunov, V. M., in the collection: Geomagnetizm i aeronomiya, 7(2), 284 (1967).
15. Misyura, V. A. et al., "Ionospheric Measurements at Scattered Stations in the Middle and High Latitudes on the Propagation of Radio Waves From Artificial Earth Satellites," Doklad na XV General'noy assambleye MGGS (Paper Presented at the 15th General Assembly of the International Union of Geodesy and Geophysics), Moscow, 1971.
16. Misyura, V. A. et al., "Statistical Characteristics of Large-Scale Ionospheric Inhomogeneities, From Observations of Signals From Satellites During the Solar Cycle in the Middle and Upper Latitudes," ibid.
17. Misyura, V. A. et al., "Portable Radio Technical Ionospheric Complex for Studying the Ionosphere and the Propagation of Radio Waves," Doklad na 10-6 Vsesoyuzn. konf. po rasprostraneniyu radiovoln (Paper at the 10th All-Union Conference on the Propagation of Radio Waves), 1972.
- 18-19. Misyura, V. A., "Composition, Temperature, and Reduced Altitude of the Upper Ionosphere," Doklad na Vsesoyuzn. seminare po fizike ionosfery (Paper at the All-Union Seminar on Ionospheric Physics), Tomsk, 1953.
20. Misyura, V. A., "Theory and Techniques of Calculating Reflection, Delay, and Doppler Shift in the Frequency of Radio Waves in the Earth's Atmosphere, Whose Index of Refraction Depends on Three Coordinates," Doklad na 4-y Vsesoyuzn. konf. MBSSO (Paper at the Fourth All-Union Conference of the Ministry of Higher and Secondary Special Education), Khar'kov, 1960.
21. Misyura, V. A., Solodovnikov, G. K., and Migunov, B. M., Kosmicheskiye issledovaniya, 5(1), 82 (1967).
22. Misyura, V. A. et al., Raschet neregulyarnykh effektov radiovoln, obuslovlennykh krupnomasshtabnymi neodnorodnostyami ionosfery (Calculation of Sporadic Effects in Radio Waves Caused by Large-Scale Ionospheric Inhomogeneities), Khar'kov, 1960.

/20



23. Misyura, V. A., and Yanovitskiy, E. G., Raschet neregulyarnykh effektov pri rasprostraneni radiovoln, obuslovlennykh krupnomasshtabnymi neodnorodnostyami ionosfery kvaziperiodicheskoy volnistoy struktury (Calculation of Sporadic Effects in the Propagation of Radio Waves Caused by Large-Scale Ionospheric Inhomogeneities With Quasiperiodic Undulating Structure), Khar'kov, 1960.
24. Misyura, V. O. et al., Visnik Khark. un-tu, radiofizika i elektronika, 80(1), 3-14 (1972).
25. Misyura, V. A., "Theory and Calculation on the Effects Arising in the Propagation of Radio Waves in the Near-Earth Gyrotropic Spatially Inhomogeneous Quasisteady Plasma," Doklad na simpoziume URSI po teorii elektromagnitnykh voln (Paper Presented at the Symposium of the URSI [transliterated] on the Theory of Electromagnetic Waves), Tbilisi, 1971.
26. Misyura, V. A., Bazhenov, G. M., and Krokhmal'nikov, Ye. B., Trudy 8-y Vsesoyuzn konf. po rasprostraneniyu radiovoln (Transactions of the Eighth All-Union Conference on the Propagation of Radio Waves), Ashkhabad, 1967.
27. Misyura, V. A., and Krokhmal'nikov, Ye. B., "Results of Investigating the Trajectory of Short Wave Rays in a Spatially Inhomogeneous Ionosphere," *ibid.*
28. Misyura, V. A. et al., Raschet nekotorykh statisticheskikh kharakteristik, fluktuatsiy effektov, voznikayushchikh pri rasprostraneni radiovoln v ionosfere (Calculation of Several Statistical Characteristics and Fluctuations of Effects Arising in the Propagation of Radio Waves in the Ionosphere), Tbilisi, 1971.
29. Misyura, V. A., and Yanovitskiy, E. G., Metodika rascheta i raschetnyye formuly refraktsii i zapazdyvaniya radiovoln, prokhodyashchikh cherez sloistuyu atmosferu (Calculation Methods and Working Formulas for the Refraction and Delay of Radio Waves Passing Through a Stratified Atmosphere), Parts I and II, Khar'kov, 1960.
30. Misyura, V. A. et al., Geomagnetizm i aeronomiya, 9(3), 445 (1969).
31. Misyura, V. A. et al., "Ionospheric Studies on the Propagation of Radio Waves From the Interkosmos-2 and Kosmos-321 Satellites," Doklad na Mezhdunarodn. seminare "Interkosmos" (Paper Presented at the International Symposium "Interkosmos"), Moscow, Institute of Terrestrial Magnetism, the Ionosphere, and Radio Wave Propagation of the USSR Academy of Sciences, 1970.

32. Misyura, V. A. et al., "Investigation of Large-Scale Ionospheric Inhomogeneities and Effects in the Propagation of Radio Waves From the Interkosmos-2 and Kosmos-321 Satellites in Recording the Faraday and Doppler Effects of Coherent Signals at Widely Separated Stations in the Middle and Upper Altitudes," *ibid.*
33. Misyura, V. A. et al., "Results of Studies on the Solar Cycle Using the Correlation Interpretation of Artificial Earth Satellite Signals of Large Ionospheric Inhomogeneities," *ibid.*
34. Misyura, V. A. et al., Radiotekhnika, No. 6, 24 (1968).
35. Misyura, V. A. et al., "Temperature of Electrons and Ions, Electron Concentrations, and Content of Ionosphere at Middle Latitudes During High Solar Activity From Incoherence Scattering Measurements," Doklad na XV General'noy assambleye MGGS (Paper Presented at the 15th General Assembly of the International Union of Geodesy and Geophysics), Moscow, 1970.
36. Misyura, V. A. et al., "Use of the Faraday Effect of Radio Signals From Artificial Earth Satellites and Rockets for Determining the Electron Concentration in the Upper Ionosphere, Part I," Doklad na 4-y Vsesoyuzn. konf. MVSSO (Paper Presented at the Fourth All-Union Conference of the Ministry of Higher and Specialized Secondary Education), Khar'kov, 1960.
37. Misyura, V. A. et al., Doklad na X Vsesoyuzn. konf. po rasprostraneniyu radiovoln. Tezisy dokladov, sektsiya I, III (Papers Presented at the Tenth All-Union Conference on the Propagation of Radio Waves, Abstracts of Papers, Sections I and III), "Nauka", Moscow, 1972.
38. Misyura, V. A. et al., in the collection: Ionosfernyye Issledovaniya, No. 20, 85, 118, 122 (1972).
39. Misyura, V. O. et al., Visnik KhDU, radiofizika i elektronika No. 1, 89-102 (1972).
40. Misyura, V. A. et al., Radiofizika, 1973 [no issue number given].
41. Misyura, V. A. et al., "Possibilities of Studying Inhomogeneities and Dynamics of the Ionosphere by Incoherence Scattering," Doklad na Mezhdunarodnom simpoziume po dreyfam i neodnorodnostyam v ionosfere (Paper Presented at the International Symposium on Drifts and Inhomogeneities in the Ionosphere), IZMIRAM, Moscow, 1971.

N74-28274

STUDY OF THE MOON AND PLANETS AT THE KHAR'KOV  
STATE UNIVERSITY ASTRONOMICAL OBSERVATORY

N. D. Barabashov, deceased

The 20th century has been marked by the vigorous growth of stellar astronomy. This led to a reexamination of the views of stellar evolution and the nature of the internal energy of stars. The human eye, aided with enormous telescopes, began to penetrate into space to unimaginable distances -- billions of light years. The most distant stellar systems were discovered. Deeper study of galaxies began. /21

The planetary world -- our solar system and near space -- had been studied very little and only few researchers had devoted themselves to this field of astronomy.

This was caused by the desire to arrive at an idea of the Metagalaxy as a whole at the regions of the universe lying beyond its limits. This situation was also furthered by the fact that the study of stars, as self-luminous objects, is much easier and gives more reliable results than the study of planets reflecting solar light.

However, from the beginning of the space age, which the Soviet Union initiated, by launching the world's first artificial satellite, the position has changed dramatically. Interest in planets is steadily rising and their study from the space in their direct proximity or even by use of spacecraft launched from the surface of the Moon and the planets provides us with altogether indisputable unambiguous results. Of special value are the results obtained simultaneously from Earth and from space.

Photometric and spectrophotometric studies of the Moon and the planets have proven highly productive. The photographic photometry of these bodies is through different light filters with special treatment of the observational material began to be first employed at the astronomical observatory of Khar'kov University by the author of this article. The investigation of the physical properties of the Moon and the planets at the astronomical observatory of Khar'kov University has acquired, during the years of Soviet power, such a broad development that it elevated this institution into the ranks of the leading observatories, both in the USSR and abroad, in this research area.

The study of the Moon and the planets, as well as the properties of interplanetary space makes it possible not only to form an idea of our nearest cosmic bodies and their evolution, but also to solve several practical problems associated with the Earth. These problems include refining our knowledge of the configuration of the Earth and its internal structure, finding locations of minerals, improving long-range weather forecasting, and also studying processes taking place in the Earth's atmosphere, and warning of the appearance in different parts of our planet of storms and hurricanes sometimes erupting in populated areas and bringing enormous destruction and human losses.

Even before the beginning of the space age, attempts were made to investigate the Earth by methods that would permit studying several of its properties as if the observations have been taken out from the Earth's surface, but from space.

For example, V. G. Fesenkov, studying the photometric characteristics of the upper layers of the Earth's atmosphere at twilight, found variations in the density with altitude. By measuring the brightness of different points on the lunar disk in a number of penumbra using spectrophotometer or light filters, he determined the concentration of ozone in the Earth's atmosphere, and so on.

The photometric method made it possible to determine also the reflectivity of the Earth as a whole, since it seemingly was observed from space. The author set out to achieve this as early as 1918. It was done by comparing the brightness of sections of the Moon directly illuminated by the Sun with the sections illuminated by the Earth, which scattered at different sides and therefore also onto the Moon the light from the Sun. The illumination of the Moon by the Earth is especially intense and readily discernible at the time when the Moon appears to us as a narrow crescent. During this time the rest of the Moon not illuminated directly by the Sun is also visible and is faintly luminous in the so-called earthshine. After the first quarter, the earthshine is so weakened that it is difficult to detect. This occurs because the phases of the Moon observed from the Earth, and the phases of the Earth observed from the Moon are mutually reciprocal. When the Moon appears to us as a narrow crescent, the light from the nearly entirely illuminated hemisphere of the Earth falls on it. After the first quarter, the illuminated part of the Earth is much smaller and scatters onto the Moon much less light. By comparing the brightnesses of the regions of the lunar surface illuminated by the Sun with the same regions in earthshine at different phases, and by conducting the appropriate calculations, we found the so-called spherical albedo of the Earth, which is the ratio of the amount of light scattered by a celestial body in all directions to the amount of

/22

light reaching it from the Sun. It was found that as a whole, the Earth scatters 43 percent of the sunlight reaching it and this value can vary by several percent, depending on what part of the Earth -- dry land, oceans, or snow or cloud cover -- reflects sunlight.

To determine the albedo of the Earth, we must find the law of reflection of light from the lunar surface, which at that time was not known. The author's observations showed that this law differs sharply from the law used up to that time. All the characteristics of the law of reflection of light from the lunar surface observed were explained by the author on the basis of theoretical and experimental studies, as a consequence of the extreme porosity and pitted character of the lunar surface. It was shown that the characteristics of the law of reflection from the Moon are caused not by major irregularities of the crater type, but by fine pores and fragments, whose dimensions vary from fractions of a millimeter to several millimeters, and that this porosity was so great that the ratio of the area of the surface covered by the pores to the overall surface is 80 percent.

Further observations conducted at the KhAO [Khar'kov Astronomical Observatory] showed that the lunar surface is made up of spongelike, porous, and fragmented volcanic rock.

All these conclusions were confirmed by the data of Soviet automatic stations, the first to soft-land on the lunar surface -- Luna 9, Luna 13, and also by the American Surveyor craft. They were also confirmed by American astronauts, landing on the lunar surface and bringing samples of lunar rock back to Earth.

The concepts of the American scientist T. Gold that the surface of the Moon is covered with a thick layer of dust proved incorrect.

It must be noted that work was carried out in the interpretation and development of details and processing of the photographs of the far side of the Moon transmitted to Earth by the interplanetary automatic station Luna 3 in Moscow, independently of other groups (GAISH [State Astronomical Institute imeni P. K. Shternberg]) under the supervisor of Yu. N. Lipskiy, in the Pulkovo Observatory (GAO AN SSSR [Main Astronomical Observatory of the USSR Academy of Sciences]) under the supervision of A. V. Markov, and in Khar'kov (KhAO) under the supervision of N. P. Barabashov. From these materials, the world's first map of the far side of the Moon was compiled, then a globe and the atlas, of which the author of this article was one of the editors. A total of 1198 newly discovered formations of the lunar surface were entered onto the map.

On 18 July 1965 a space rocket was launched from a satellite; the rocket injected the Zond-3 Automatic Station into a heliocentric orbit. This station obtained very clear photographs of the far side of the Moon. The photographs taken with Luna 3 and Zond 3 covered 95 percent of the far side of the Moon. In the eastern sector of the far side of the Moon, 3374 formations were captured on the photographs taken by Zond-3, about 200 of which were named. It was found that in the Khar'kov that the lunar surface is quite uniform, however there are regions on it where the uniformity is more or less disturbed. From analysis it was established that this disruption can be accounted for not only by the different microrelief, but also by more essential factors, for example, the presence of formations with different thermal conductivity and dissimilar chemical composition. No major, very discernible changes that would have strong influence on the appearance of any region of the lunar surface were observed.

In October-November 1958, at the Krymskaya [Crimean] Astrophysical Observatory, Doctor of Physico-mathematical Sciences, N. A. Kozyrev, together with Khar'kov astronomer V. I. Yezer'skiy, made spectrophotometric observations of several lunar craters. In a spectrogram of crater Alphonsus, in the spectrum of its central ridge N. A. Kozyrev detected a bright glow, which evidently was caused by the escape of a gaseous jet. As a result of studying the spectrogram taken in the Pulkovo Observatory, the presence of compounds of carbon in the products of the gaseous eruption on the Moon could be suggested. American astronomers Greenacre and Barr in 1963 observed color effects in the area of the crater Aristarchus, indicating, in their view, its volcanic activity. /23

It must be noted that American astronomer K. E. Healey considers that short-lived phenomena on the Moon, such as: the appearance of red spots and patches, cloud patches, and bright flashes in polarized light -- are an indication of the tidal action of the Earth leading to fractures and shifts in the lunar crust and the escape of gases with an abrupt change in the thermal regime of regions of the Moon. In periods of eclipses, this could be associated with the action of corpuscular streams from the Sun causing the luminescence of the lunar surface, the appearance of volcanic activity, and the fall of meteor bodies.

Some Soviet and foreign astronomers maintained the view that the lunar surfaces of the same type and its different regions have no color gradations at all. The author was able to show that this conclusion stems from inadequate precision of measures of observation used by them. In 1923 and in subsequent years, the author made a series of determinations of the colors of different areas of the lunar surface. It was found that colors on the moon are very distinguishable.

Based on our observations, we can in general outline represent the distribution of color on the lunar surface as follows. The southern part of the Sea of Crises appears greenish, and the northern -- rust-colored. The Sea of Plenty, in contrast, is rust-colored in the southern region, and greenish in the northern. The Sea of Tranquility is bluish. The Sea of Serenity is reddish in the center, but greenish bands are observed along its southern and northern margins. The structure of the Sea of Rains is mottled with reddish, greenish, and rust-colored regions. The dimensions of these patches vary. The Sea of Storms is greenish, and only its southern extremity appears brownish. The Sea of Moisture is reddish, and the Sea of Clouds in which greenish patches are detectable. Along the Crater Tycho distinct reddish tones can be seen. The Sea of Cold is reddish. In the center of the lunar disk and along its southern limb are reddish regions, and the highland regions adjoining the Sea of Tranquility are greenish. The bottom of the Cirque Plateau is reddish. South of the Sea of Rains, five very intense green patches can be seen. It must be noted that many parts of lunar maria have a mosaic structure where small regions with highly variegated hues lie closely together. The author was able to photograph the color of lunar formations even on ordinary color film.

In 1889-1890, the French astronomer Landerer based on his polarimetric observations, concluded that vitrophyre, sand, salt, and many other rocks not of volcanic origin may be on the lunar surface.

In 1923, the author of this article, conducting longer and more exact observations, showed that Landerer's method of investigation was erroneous. On the basis of long-term observations, we concluded that the lunar surface must consist of highly porous and fragmented volcanic rock. Turfaceous lava and basalts are most similar to lunar rock.

Later, students of the author also participated in observations -- V. I. Yezerkiy, V. A. Fedorep, A. T. Chekirda, and L. A. Akimov, who confirmed and supplemented all these conclusions. A photometric catalog of 172 points on the lunar surface was piled and formulas were derived for calculating, with sufficient accuracy, the illumination at any point of the lunar surface at different phase angles. The latter feature is necessary for the successful photography of formations of the lunar surface from both Earth and space, as well as when landing on the lunar surface.

/24

Investigations of samples of lunar rock brought back to Earth by American astronauts wholly confirmed the results of the author's ground observations. They showed that the lunar rocks are not monocolored, but differ very markedly in coloration:

they are black, whitish, reddish, greenish, bluish, rust-colored, and other tones. It can be assumed that the color differences in the surface layer of the Moon are appreciably blurred by the action of exogenic factors. The reduction in color contrasts on the lunar surface could be a consequence of its bombardment with solar wind hydrogen ions, since atomic hydrogen at a high temperature is one of the most powerful reducing agents.

Thus, the direct study of rocks comprising the lunar surface completely confirmed the results of the ground observations of the author and his students in that the lunar surface consists of highly porous and fragmented rock and that the rock color differs appreciably. Study of these samples showed that they are similar to terrestrial basalts and gabbros. In content of basic components, they are closer to the chemical composition of feldspar achondrites (eucrites). Lunar rock also contains about 16 percent iron and an increased content (compared with primitive basalts on Earth) of elements such as titanium and several others.

Let us assume that by comparing the chemical composition of rocks of the Earth and the Moon one can resolve the question as to whether the Moon was captured by the Earth or whether it separated from it in the very remote past. If the composition of the material in the mantle of the Earth and the depths of the Moon coincide, it can be assumed that the Moon was formed by separating from the Earth. Today there is every reason to assume that the Moon was formed not less than 4 billion years ago. Since the study of the Moon is of exceptional interest, it will continue with the aid of spacecraft and from ground. The latter will make it possible to compare the photometric features of different areas of the lunar surface and thus to facilitate selecting areas as the most suitable for spacecraft landings, as well as of particular interest.

An exceptional achievement of our science was the landing on the lunar surface of history's first Lunokhod-1, which was driven by Earth command over the lunar surface for a good many thousands of meters and conducted highly valuable analyses of lunar soil at considerable distances.

In 1919 the author began photometric observations of Venus with light filters. During processing of the photographs of Venus it was noted that maximum brightness at the intensity equator of the planet corresponds to a point for which the angle of incidence of solar light and its angle of reflection to the Earth are nearly equal, where the incident and reflected rays lie in different sides of the normal to the visible surface of Venus. In other words, the reflection of light from Venus is



mirror-like to some extent. Later, this conclusion was confirmed by V. I. Yezerkiy and other observers. We also showed that a low-density atmospheric layer lies over the opaque cloud layer of Venus. It was found as well that the light of Venus changes in relation to phase angle. This is associated with the scattering of light in the upper layers of the Venusian atmosphere and its cloud layer, as well as with fluctuations in the altitude of these layers. The author assumed that most of the mirror effect is caused by ice crystal particles in the clouds of Venus, similar to altocirrus.

As our observations showed, the distribution of brightness on the disk of Venus is associated with the appearance on it of dark and light patches. An enormous dark patch on Venus was detected by the author and observed by him and colleagues at KhAO on 30 August - 20 September 1964; its area was 20 million km<sup>2</sup>. The analysis of photometric characteristics of the observed spot, 125 made by us for the first time, suggested that this was an enormous interruption in the upper part of the cloud layer of Venus through which could be seen the lower-lying layer of reddish hue or a cloud of some relatively large particles ejected from the surface of the planet into its upper cloud layer and differing from them in color. It is also possible that these particles were formed in the cloud layer itself owing to changes in some conditions, for example, temperature. In any case, the appearance of the enormous formations observed at KhAO indicates that some powerful processes covering large expanses occur on Venus. Thus far we have only very hazy ideas of what is happening about the cloud layer of Venus in the region inaccessible to optical observations. Several alternative models of the Venusian atmosphere have been constructed. The principal models can be taken as the greenhouse, eolospheric, and ionospheric. Without describing these models, let us say that at present after the flight of the Soviet Automatic Interplanetary Station Venera-4, the ionospheric model lost any basis, since it was found that the planetary surface is at a high temperature. Also, the results of direct measurements of the ionospheric plasma made by the equipment of the APS Venera-4 showed that over the night side the ionosphere of Venus is much thinner than the Earth's.

To extend the investigations of Venus and to refine already obtained results, in January 1969 two interplanetary stations were launched in the USSR -- Venera-5 and Venera-6. On 16 May the first station, completing a flight of about 350 million km in 130 days successfully made an interplanetary space voyage and descended smoothly into the atmosphere of Venus.

On 17 May, the Venera-6 station also completed a many months'-long flight along the Earth-Venus route. The station entered the atmosphere of the planet approximately 300 km from

the entry site of the Venera-5 station. The descending craft of the station continued in the Venusian atmosphere for 51 minutes. During the descent, measurements were made of the characteristics of the Venusian atmosphere. Data obtained by the automatic stations Venera-5 and Venera-6 essentially revised our knowledge of the Venusian atmosphere. Whereas up to the surface of the planet the temperature changes adiabatically, at the level of the surface determined by the radar altimeter of the Venera-6 station (10-12 km), the temperature and pressure are about 400° C and 60 atm, while at the level of the surface determined by the altimeter of the Venera-5 station (24-25 km), temperature and pressure can reach values of the order of 530° C and 140 atm. The Venera-6 and Venera-5 stations brought to the planet a pennant with a bas-relief of V. I. Lenin and a representation of the State Code of Arms of the Soviet Union.

The automatic station Venera-7 landed on the surface of Venus in December 1970 and transmitted scientific information directly from the planetary surface for another 23 minutes. In this way was finally established that Venus has an unusually strongly heated atmosphere. The temperature at its surface is about  $475 \pm 20^\circ \text{C}$ , and the pressure is  $90 \pm 15 \text{ atm}$ .

Therefore, the conditions on Venus are very different from those on Earth. However, to resolve the question as to the nature of the surface of the planet itself and to revise our knowledge about physical conditions on it requires further, particularly well-organized observations both from Earth, space, as well as from the surface of the planet itself, which of course involves great difficulties.

The planet Mars, as the planet of the solar system most similar to Earth, has also been intensively studied at the Astronomical Observatory of the Khar'kov State University. There the first detailed photometric and colorimetric investigations of Martian photographs were made by the author of this article as early as 1932. Later, these investigations were increasingly extended and made it possible to reach the following conclusions. The Martian atmosphere is relatively highly rarefied. However, the results obtained by different authors using different methods differ widely. Thus, long-term photometric observations gave a mean pressure of 60-70 mm, spectrophotometric measurements gave a mean pressure of 8-25 mm, while observations taken by the American space station Mariner-4 sent to Mars gave a mean pressure of less than 5 mm. The reason for these discrepancies is that photometric observations are based on total absorption and scattering of light by both gases and atmospheric aerosol. Spectrophotometric observations pertain only to the gaseous constituent and are therefore more reliable. Results obtained by Mariner-4 cannot be regarded as wholly trustworthy, since the determination of the altitude to which this result relates is

unreliable. The author, excluding the effect of the aerosol with all possible precision from his photometric observations found that the pressure at the Martian surface is 18-37 mm. For long time neither water vapor or oxygen could be detected on Mars. Recently, small amounts of both constituents were finally detected, while carbon dioxide on Mars is probably present in amounts several times greater than on Earth. One can approximately present the following composition of the Martian atmosphere: nitrogen -- 98.5; oxygen -- 0.1; argon -- 1.2; and carbon dioxide gas -- 0.25 percent.

Photometric observations made by the author of reddish light regions on Mars (so-called highlands) established that when these are observed in red light it appears very level and smooth. Our later investigations suggest that the "continents" of Mars are covered with fine dust or sand with more or less transparent grains, perhaps even slightly specular. In color they correspond to ground iron ore or limolite, and also red sandstone or reddish tufa. Perhaps these ordinary sands with an admixture of iron oxide.

On 1 November 1962, for the first time in history, the interplanetary station Mars-1 was launched in the Soviet Union as part of a program of investigation of space and the planets of the solar system. The principal mission of the launch of this station was to conduct long-term investigations of space during a flight to the planet Mars and to establish interplanetary radio communications. The station transmitted information about streams of ionized gas ejected from the surface of the Sun, the intensity of magnetic fields, and the distribution of meteoric matter in space. It twice passed across meteor showers, one of which had not been known earlier. The frequency of collision with meteorites in passing through the meteor shower was approximately one collision every 2 minutes.

These results made a major contribution to the study of space. The flight of Mars-1 station made it possible for the first time to establish radio communications over an enormous distance -- 105 million km. Beyond this the communications were lost.

On photographs of Mars taken with the spacecraft Mariner-4, Mariner-6, and Mariner-7 (United States) from a close distance one can see numerous craters ranging diameter from several kilometers to several hundred kilometers. In the view of American specialists, the clearly discernible details at the location of the canals do not refute and do not confirm the hypotheses that life exists on this planet.

On the basis that craters were discovered on Mars, several astronomers assumed that the Martian surface must reflect light just as does the Moon. However, this conclusion is wholly unsupported. First of all, all photographic and spectrophotometric observations contradict this. Secondly, our studies of the lunar and Martian surfaces, as well as calculations based on theoretical considerations, show that even on the Moon where the craters are much denser than are Mars, the law of reflection of light is basically caused by fine irregularities (microrelief), and not by large irregularities of the types of craters and cirques (macrorelief).

The American astronomer A. Young, from a distribution of brightness along the disk of Mars based on photographs obtained by Mariner-4, found that the altitude of the homogeneous Martian atmosphere is approximately  $10^{-5}$  km, while the optical thickness for the wavelength  $0.6 \mu$  is  $\tau = 0.03$ . This same investigator also confirmed the author's conclusions that the reddish regions of Mars are relatively smooth and probably covered with sand. The low pressure in the planetary atmosphere was also confirmed by the American automatic stations Mariner 6 and Mariner 7. 127

Observations at the KHAO also showed that the dark patches on Mars called maria are much more uneven and pitted than the highlands. The reasons for this phenomenon have not yet been found.

Of particular interest are the seasonal changes in the maria, lakes, oases, and canals on Mars. All these changes are inseparably associated with a decrease in the dimensions (thawing) of the polar caps. With the onset of spring and summer, the polar cap begins to thaw, and from it toward the equator at the rate of about 40 km per day the darkening wave spreads, which causes the change in the shape and color of the maria and other dark formations, improving their visibility. This wave reaches the equator, and in autumn passes into the opposite hemisphere of the planet. Here the oncoming darkening wave begins to advance soon from the other polar cap.

We found that some regions of the Martian maria located in the equatorial zone, and therefore for the entire Martian year situated approximately in the same climatic conditions, for most of the year are bluish, gray-bluish, and gray-greenish. Between spring and autumn, some regions in these maria take on a greenish color, and sometimes in the summer a brownish hue appears here. In some sections of the maria and bays located in the middle latitudes of Mars, the greenish and bluish colors observed only in summer, on days when the Sun at noon day climbs highest in the sky and the days become the longest. Additionally, it was found that the closer a dark region is to the pole,

the shorter the period during which it appears greenish. The brownish and grayish-brownish tones are noted on the shortest days. Objective methods of investigation used by the author at the astronomical observatory of the Khar'kov State University establish that the Martian maria in general are reddish, but much less so than their surrounding light highlands. Therefore, the blue and bluish coloring of the dark Martian regions noted in visual observations must to a considerable extent be considered as resulting from simultaneous color contrast; color detail against a colored background is more contrasty. The contrasty color, as a rule, is close to the complimentary color. Thus, for example, a yellow detail against the red background must appear bluish or greenish.

Observations show that in spring and summer some maria become less red, while others (true, small sections) take on a greenish hue. The areas that only darken, but whose colors remain unchanged, are perhaps only humidified locations. They only darken in spring and turn pale in autumn. Photometric measurements showed that with the change in the times of the year there is also a change in the roughness (pitted nature) of the maria, and also evidently of the highlands.

A fair number of hypotheses have been advanced about the nature of the Martian maria. However, many of them are only of historical interest, while others have been rejected as inconsistent. It is quite clear that the Martian maria are not open bodies of water. The idea that these are humidified locations evidently is only partially true. The hypothesis of the American scientist, McLaughlin, stating that the Martian maria are deposits of volcanic ash and their outlines repeat the wind directions in the Martian atmosphere, is artificial and unsupported. The seasonal changes are interpreted by him as the result of changes in the intensity of wind, humidity, and temperature. Some scientists suggest that the dark regions -- Martian maria -- are some kind of elevations of the plateau type. However, this hypothesis is quite artificial. The seasonal changes occurring in the Martian maria are more naturally accounted for by the existence in these regions of some organic life, whose development depends to a greater extent on the incursion of moisture from the thawing polar caps. We can only hypothesize about the forms of organic life on Mars. Naturally, there is no agreement on this problem.

Academician L. I. Oparin believes that life on Mars is represented by low-organic microbes that do not require free oxygen for their existence. In the view of the French investigator A. Dolfuss, on Mars there are only the simplest algae, protected by a shell against the destructive action of solar

short-wave and hard radiation. J. Kuiper and the author of this article believe that the simplest plants of the type of mosses and lichens exist on Mars.

G. A. Tikhov suggested that there is plant life on Mars in its higher forms -- deciduous and coniferous.

Interesting considerations on the presence of plant life on Mars have been made by M. Kuchеров and Ye. Epik: "If there were no plant life on Mars in Martian maria, with the course of time they would have been filled over with dust swept in by the winds from the deserts of Mars during dust storms." In their view, the Martian maria after the end of dust storms rapidly take on their form appearance, since the dust is shaken off by the upper parts of plants and streams downward. We have been witnesses of appearance of a new dark region on Mars. Our observation was confirmed by the Czech scientists Rykl, Sadil, and Kalaba. The region located at the site of the canal Gota and Nepentes and called the Laocoon Node thereupon became even larger and more active.

The polar caps, about 3000-4000 km in diameter in winter, almost completely disappear in summer. In our view, they consist of two components -- a thin and noncontinuous cover of snow or frost, through which the reddish land of the planet can be seen, and the atmospheric constituent -- fog and light clouds -- developing in the thawing of the polar caps. Sometimes both components are observed, and sometimes only one. Sometimes both components disappear. Quite often light formations appear in the Martian atmosphere; they are at an altitude of about 10 km and have, as shown by the author and his colleagues, a thickness of only 8-10 m. Observations showed that cloud formations on Mars travel at the speed of 4-8 m/sec, that is, at a rate much slower than on Earth (30-40 m/sec). Relatively dense clouds appear on Mars fairly infrequently; therefore, the detailed study of the atmospheric circulation on Mars is made difficult. In addition to clouds and haze, sometimes yellow clouds appear on Mars. They are of the same color as the light regions of Mars. There is full reason to assume that they consist of fine dust lifted by the winds from the surface of the Martian atmosphere. Sometimes these formations spread for more than half the visible disk of the planet, covering from the observer enormous expanses of its surface. The dust entering into the clouds evidently is very fine and light, since otherwise it could not be held for long time in the rarefied Martian atmosphere. A particularly intense dust storm in its atmosphere was observed on 1-15 September 1956, where not only the dark details of the surface were covered, but also the southern polar cap, which at the moment of disappearance had still appreciable dimensions. Interestingly, the

onset of the dust storm on Mars was preceded by the appearance of large light formations. Thus, on 23 August at 23 hours 10 minutes Moscow time, the author at the Khar'kov Astronomical Observatory, and subsequently astronomers of other observatories, detected a significant lightening of the region on Mars which is called Argyrus. In the days following, the light formation extended to neighboring regions and was not less bright than the polar cap.

In analyzing the results, the astronomers concluded that in this case hoarfrost or rime, and in part fog, had formed on the surface of the planet. The light cloud formations are usually discernible also in the morning and evening parts of the planet's disk. It is probable that these very high morning and evening fogs, which are similar to our cirrus clouds and are often accompanied by the precipitation of rime. /29

Based on all the observations of Jupiter made at the astronomical observatory of Khar'kov State University, we arrived at the following general conclusions concerning the physical conditions on this planet. In our view, there is a very thin layer of gas over the visible surface of the cloud layer of Jupiter. The dark and light bands constituting its visible surface lie nearly at the same level. Rapid and appreciable changes on Jupiter can be accounted for by the fact that certain gases that are part of the atmosphere on this planet are at the limit of condensation and evaporation. Therefore, even very small changes in solar radiation cause them to pass from the liquid into the gaseous state, and vice versa. Thus, the extent of the gaseous layer over the cloud cover can change quite intensely. This must alter the distribution of brightness values over the planet's disk, which has in fact been detected by our investigations. Our view of the Jovian atmosphere agrees with the opinion expressed by several other authors, according to which the clouds forming the visible surface of Jupiter can to a large extent consist of methane droplets and ammonia crystals. Gases boiling at very low temperatures can exist in the cold atmosphere of Jupiter (it is 5.2 times farther from the Sun than is the Earth). This point of view, the large red patch observed on Jupiter is most likely (as indicated by R. Hoyle (United States)) is a stable, vertically oriented column of gas or liquid. How valid this hypothesis is we find it difficult to state.

After examining sketches and photographs of the surface of Jupiter obtained by various observers, beginning in 1874, the author concluded that in spite of certain deviations, the following general regularity is noted. There the solar activity maxima (usually 1.5 years before or 1.5 years after these maxima), a broad dark band lies at the equator, and in the intervals between these two maxima the distance between the margins of

the equatorial bands becomes greatest. The perturbing action of radiation during the period of the maximum solar activity evidently causes the formation of the dark equatorial band, which when viewed through a telescope appears first pale, consisting of numerous patches and inclined bands, and then increasingly darker, more dense, and compact. In mass, Jupiter is intermediate between a star and planet, since the body with a sufficiently large mass exceeding one-hundredth of the solar mass according to modern concepts is no longer a planet; its own sources of energy must originate on it. Radio emissions from Jupiter were first detected in 1955. Various investigators attempted to explain the source of the sporadic radio emissions from Jupiter. However, thus far there has been no wholly satisfactory answer. The temperature of the regions lying at the level of the cloud layer from which the radio emissions issue at wavelength shorter than 3-5 cm, as well as the infrared radiation was found to be 140° C.

In 1963, in spite of the enormous distance of Jupiter from Earth (590-600 million km), Academician V. A. Kotel'nikov and his colleagues picked up a radar signal reflected by this planet. It reached the radar 1 hour 6 minutes after it was sent from Earth.

Much about the nature of Jupiter has already known to us, but still there are quite a few controversial questions that await resolution.

All observations made of Saturn at the astronomical observatory of Khar'kov State University convince us that this planet is quite similar to Jupiter. These observations indicate that the layer of free atmosphere over the cloud cover of Saturn is thicker than on Jupiter. This can be a consequence of the lower temperature of Saturn promoting the greater freezing of ammonia and its transition into the solid state. On falling out from the atmosphere and entering the cloud layer, it liberates an atmosphere that must consist generally of hydrogen and methane. Dark bands, as our observations showed, evidently lie above the light regions of its visible surface. Saturn is very far from the Sun -- 1.4 billion km; the temperature of its visible surface is very low. At its upper limit it is approximately -120° C, and based on radiometric observations -- -155° C. In spite of this, sometimes very significant changes occur on the planet. Thus, in 1932 an enormous white patch splitting into two parts and soon disappearing appeared in the equatorial zone of Saturn. However, the photographs taken through a red light filter the author was able even over the course of a year to observe the subsequent reduction of its brightness. It is possible that here a large mass of freezing gas appeared, subsequently dissolving or descending into the lower-lying strata of

/30



the cloud layer. Later very light patches and bands were also observed to appear in the equatorial and other regions of Saturn.

In 1926, the American astronomer W. Wright suggested that on the photographs of Saturn that he had taken in ultraviolet light the Crepe Ring projected onto the disk of Saturn in the form of a dark zone of the width which corresponds to the distance from the inner margin of Ring B to the surface of the planet. However, this hypothesis was not confirmed. In 1933, photometric measurements made by the present author firmly established that the interval between the inner margin of the Crepe Ring and the sphere of Saturn was filled with small particles very appreciably scattering light at short wavelengths; that the interval in question had appreciable brightness not equal to zero, as in regions surrounding the rings externally. This made it possible to conclude that the rings of Saturn extend to the very sphere itself. In recent years, this conclusion was confirmed by N. A. Kozyrey and M. S. Bobrov. Confirmation of the presence of a highland between the sphere of Saturn and its Crepe Ring was found in the report that in October 1969 the French astronomer P. Heren discovered a fourth, the innermost, ring of Saturn.

The more distant planets, the Uranus, Neptune, and Pluto, have visible disks so small that their surface area has never been large enough to study either visually or photographically. However, today when interplanetary automatic stations are being sent to Venus and Mars, there is no doubt that they will also visit the more distant planets and that the entire solar system will be fully studied by us.

1474-28275

# ELECTROMAGNETIC PROCESSES IN THE ATMOSPHERE OF PULSARS

/30

A. K. Yukhimuk

Pulsars were discovered in 1968 by Hewish in [1]. At the present time more than 55 pulsars are known [2]. The most typical feature of pulsars distinguishing them among other sources of radio emission is the repetition period of their pulses  $P$ . The radio emission of pulsars received at some frequency  $\nu$  (for a detector passband width  $\Delta\nu \ll \nu$ ) consists of pulses of complex structure and with a total duration  $\Delta\tau$  of the order of 5-50 msec. The periods of all currently known pulsars lie in the interval of values 0.033-3.7 seconds. The shortest period is shown by the pulsars associated with the Crab Nebula NP 0532 --  $P_0 = 0.033$  sec, and the pulsars associated with the Nebula Vela x PSR 0833 --  $P_0 = 0.0892$  sec. The longest period is shown by the Pulsar NP 0525 --  $P_0 = 3.7455$  sec. Longer and more exact measurements show that the natural periods of pulsars  $P_0$ , even though vary slightly, nonetheless do vary with time. For example, for the pulsars CP 1919,

/31

$$\frac{dP_0}{dt} \approx 10^{-15}.$$

The periods of all currently known pulsars are growing longer.

In a detailed investigation of radio emission pulsars, it was found [2] that their structure is highly complex. It turned out that each pulse consists of a series of sub-pulses, the exact shape of which can change from one pulse to the other. Variations in the amplitudes of the pulses occur more rapidly at low frequencies. Thus, at the frequency 81.5 MHz, the pulsar CP 1919 emits relatively strong pulses only for 1 minute, while at the frequency 408 MHz the burst of signal intensity lasts for half an hour longer [4].

At the present time there are several hypotheses accounting for the strict periodicity of pulsar radio emission. All these hypotheses can be classed in three groups. The first group includes models based on the assumption that the pulsations in emission intensity are due to oscillations of the star. The second group includes hypotheses suggesting that the periodicity of emission is due to the orbital motion of a binary system of stars. The third group of hypotheses includes those whose basis is the assumption that the periodic nature of emission is associated with the rotation of the star under study. Most investigators believe that a pulsar is a rotating neutron star with an

enormous magnetic moment  $\mu$ , where the axis of rotation  $\Omega$  does not coincide with the axis of the magnetic moment  $\mu$ . The rotation of the magnetic moment  $\mu$  at the frequency  $\Omega = 2\pi/P_0$  leads to the emission of electromagnetic waves at the intensity

$$W = \frac{2\mu_{\perp}\Omega^4}{3c^3}.$$

Here  $\mu_{\perp} = \mu \sin \theta$  is the perpendicular (relative to the axis of rotation) component of the magnetic dipole.

In the present work we attempt to account for certain observational data [1-4].

### Fine Structure of Pulsar Radio Pulses

In discussing the nature of pulsars, it is usually maintained that radio emission emanates from an object with dimensions  $L \sim 10^8$  cm. This conclusion is based on the fact that in neutral stars with a period of oscillations  $T_0 = 10^{-2}$  sec, the radius of the total neutral and plasma portion of the star are  $r \geq 10^7$  cm, while the rarefied plasma shell and the magnetosphere reaches dimensions  $r \geq 10^8$  cm. Assuming that the strength of pulsar radio emissions  $N \sim 10^{30}$  erg/sec, the pulse duration  $\Delta\tau \sim 10^{-2}$  sec [4], we obtained the energy density of electromagnetic radiation  $w \sim 3 \cdot 10^2$  erg/cm<sup>3</sup>. The presence of a high density of electromagnetic radiation must lead to the excitation of different kinds of oscillations in the plasma, and also to a rise in the fluctuations of electron density. Let us assume that the pulsar is a rotating neutron star with a magnetic moment  $\mu$ , where the axis of rotation  $\Omega$  does not coincide with the axis of the magnetic moment  $\mu$ . The motion of particles in a coordinate system rotating at the velocity  $\Omega$  is equivalent to the motion in a fixed coordinate system which the equivalent magnetic field is active [15]:

$$B = B + \frac{2m_e c^2}{\hbar} \Omega \quad (1)$$

The kinetic equation for the function of electron distribution in the field of an electromagnetic wave is of the form

$$\frac{\partial f_e}{\partial t} + (\mathbf{v} \nabla) f_e - \frac{e}{m_e} \left( E + \frac{1}{c} \mathbf{v} \times B + \frac{2m_e c}{\hbar} \Omega \times \mathbf{v} \right) \frac{\partial f_e}{\partial \mathbf{v}} = \nu (f_0 - f_e), \quad (2)$$

where  $\nu$  is the effective frequency of electron collisions with surrounding particles, and  $f_0$  is the Maxwellian function of electron distribution.

The corresponding linearized equation is

$$i(k_0 v_z - \omega_0 - i\nu) f_{1e} + (\omega_{Be} - 2\Omega) \frac{\partial f_{1e}}{\partial v} = \frac{e}{m_e} E_0 e^{\mp i\Phi} \frac{\partial f_0}{\partial v_1}, \quad (3)$$

where  $k_0$ ,  $\omega_0$ , and  $E_0$  are the wave vector, frequency, and amplitude of the electromagnetic wave:

$$E_x = \frac{1}{2} E_0 \exp i(k_0 z - \omega_0 t) + \text{c. c.}, E_y = \mp i E_x,$$

$$B_x = -\frac{k_0 c}{\omega_0} E_y, B_y = \frac{ck_0}{\omega_0} E_x, \omega_{Be} = \frac{e B_0}{m_e c},$$

$\phi$  is the polar angle in the velocity space.

By integrating Eq. (3), we get:

$$f_{1e} = -i \frac{e E_0}{m_e} \frac{e^{\mp i\Phi} e^{i(k_0 z - \omega_0 t)}}{k_0 v_z - \omega_0 \mp (\omega_{Be} - 2\Omega)} \frac{\partial f_0}{\partial v_1}. \quad (4)$$

To find the steady-state increment to the Maxwellian and distribution function caused by the propagation of the electromagnetic wave, let us write the second-approximation equation:

$$\begin{aligned} \frac{\partial f_{2e}}{\partial t} + (\mathbf{v} \nabla) f_{2e} - \frac{e}{m_e} \left( E_1 + \frac{1}{c} \mathbf{v} \times B_1 \right) \frac{\partial f_{1e}}{\partial \mathbf{v}} - \mathbf{v} \times \\ \times (\omega_{Be} - 2\Omega) \frac{\partial f_{2e}}{\partial \mathbf{v}} = -\nu f_{2e}. \end{aligned} \quad (5)$$

Averaging Eq. (5) over time, we get:

$$\nu f_{2e} - \mathbf{v} \times (\omega_{Be} - 2\Omega) \frac{\partial f_{2e}}{\partial \mathbf{v}} = \frac{e}{m_e} \left( E_1 + \frac{1}{c} \mathbf{v} \times B_1 \right) \frac{\partial f_{1e}}{\partial \mathbf{v}}. \quad (6)$$

Let us assume that the electromagnetic wave of circular polarization propagates parallel to the external magnetic field  $B_0$ . Then, by substituting  $f_{1e}$  in (6) and setting  $\nu = k s_e \ll |\omega_0 \pm (\omega_{Be} - 2\Omega)|$ , we get

$$f_{2e} = \frac{2e^2 E_0^2 k_0^2}{m_e^2 \omega_0 [\omega_0 \pm (\omega_{Be} - 2\Omega)]^2} \left\{ \frac{\omega_0}{k_0} \left( \frac{v_1^2}{s_e^2} - 1 \right) + v_z \right\} \frac{\partial f_0}{\partial s_e}. \quad (7)$$

Let us compute using the total steady-state function  $F = f_0 + f_{2e}$  the mean electron velocity

$$\begin{aligned} \mathbf{v} = \frac{2e^2 E_0^2 k_0^2}{m_e^2 \omega_0 [\omega_0 \pm (\omega_{Be} - 2\Omega)]^2} \mathbf{n} \equiv v_0 \mathbf{n}, \\ \mathbf{n} = \frac{k_0}{k_0}. \end{aligned} \quad (8)$$

Thus, when an electromagnetic wave propagates in a magnetized plasma, a steady drift of electrons relative to ions occurs. We know that excitation of longitudinal oscillations can be observed in this plasma.

The system of equations describing plasma effects in a magnetized rotating plasma, when external electromagnetic emission is present, is of the form

433

$$\begin{aligned} \frac{\partial f_e}{\partial t} + (\mathbf{v} \nabla) f_e - \frac{e}{m_e} \mathbf{E} \frac{\partial f_e}{\partial v} - \mathbf{v} \times (\omega_{Be} - 2\Omega) \frac{\partial f_e}{\partial v} &= 0, \\ \frac{\partial f_i}{\partial t} + (\mathbf{v} \nabla) f_i + \frac{e}{m_i} \mathbf{E} \frac{\partial f_i}{\partial v} + \mathbf{v} \times (\omega_{Bi} + 2\Omega) \frac{\partial f_i}{\partial v} &= 0, \\ \operatorname{div} \mathbf{E} &= 4\pi e \left( \int f_i d\mathbf{v} - \int f_e d\mathbf{v} \right). \end{aligned} \quad (9)$$

Hence we obtain the dispersion equation for longitudinal oscillations

$$\begin{aligned} 1 + \sum_n \frac{1}{k^2 a_e^2} \left\{ 1 - e^{-\frac{\beta_e^2}{2}} \sum_n \frac{z_{en}}{z_{en}} I_n \left( \frac{\beta_e^2}{2} \right) [\varphi(z_n) - i \sqrt{\pi} z_{en} e^{-z_{en}^2}] \right\} - \\ - \frac{2\omega_0 z_0}{k^2 a_e^2 z_0^2} Q(z_{en}) = 0, \end{aligned} \quad (10)$$

where

$$\begin{aligned} Q(z_{en}) &= 1 + e^{-\frac{\beta_e^2}{2}} \sum_n \left( 1 - \frac{k_{\perp} s_e}{\omega_0} z_{en} \right) I_n \left( \frac{\beta_e^2}{2} \right) - e^{-\frac{\beta_e^2}{2}} \times \\ &\times \sum_n \left\{ \frac{k_{\perp} s_e}{2\omega_0 z_{en}} I_n - \frac{\beta_e^2}{2} \left[ I_n + \frac{1}{2} (I_{n-1} + I_{n+1}) \right] \right\} [\varphi(z_{en}) - i \sqrt{\pi} z_{en} e^{-z_{en}^2}], \\ a_e^2 &= \frac{T_e}{4\pi e^2 n_0}, \beta_e = \frac{k_{\perp} s_e}{\omega_{Be}}, s_e = \frac{2T_e}{m_e}, \varphi = 2ze^{-z^2} \int_0^z e^{x^2} dx, \\ z_{en} &= \frac{\omega + n(\omega_{Be} - 2\Omega)}{k_{\perp} s_e}, \end{aligned}$$

$I_n(x)$  is a modified Bessel function of the  $n$ -th order,  $k_{\parallel} = k \cos \theta$ ,  $k_{\perp} = k \sin \theta$ ,  $\theta$  is the angle between the vectors  $\mathbf{k}$  and  $\mathbf{B}_0$ .

The observed intense polarization of pulsar radio emission from linear to circular indicates that in the pulsar atmosphere there exists a quite strong magnetic field, that is, electrons and ions are magnetized ( $k_{\perp} s_e / \omega_{Be} \ll 1$ ). Assuming that  $k s_e \cos \theta \ll \omega \ll k s_e \cos \theta$ , we get the solution to Eq. (10)

$$\omega_{1,2} = \frac{1}{2} [\omega_s^2 + (\omega_{Bi} + 2\Omega)^2] \pm \frac{1}{2} \sqrt{[\omega_s^2 + (\omega_{Bi} + 2\Omega)^2]^2 - 4\omega_s^2 (\omega_{Bi} + 2\Omega)^2 \cos^2 \theta}, \quad (11)$$

$$\gamma_{1,2} = \sqrt{\frac{\pi}{8} \frac{m_e}{m_i}} \frac{\omega_{1,2}^2 \omega_s^2 [\omega_{1,2}^2 - (\omega_{B_i} \pm 2\Omega)^2]}{k^2 v_{Te}^2 |\cos \theta| [2\omega_{1,2}^2 - \omega_s^2 - (\omega_{B_i} \pm 2\Omega)^2]} \times \\ \times \left(1 - \frac{v_0}{v_{\phi 1,2}} \cos \theta\right), \quad (12)$$

where

$$\omega_s = \frac{k v_{Te}}{1 - k^2 v_{Te}^2}, \quad v_0 = \sqrt{\frac{T_e}{m_i}}, \quad v_{\phi 1,2} = \frac{\omega_{1,2}}{k}.$$

From Eq. (11) it follows that when  $v_0 \cos \theta > v_{\phi 1,2}$ , oscillations with frequencies  $\omega_{1,2}$  are excited in the plasma shell of a pulsar. Using the explicit expression for  $v_0$ , let us find the critical amplitude of the electromagnetic wave, which when exceeded leads to the generation of oscillations:

$$L_{cr} = \frac{v_0}{\epsilon} [\omega_0 \pm (\omega_{B_i} - 2\Omega)] \left[ \frac{v_{\phi 1,2}}{\cos \theta \sqrt{1 - \frac{\omega_{1,2}^2}{\omega_0 (\omega_0 \pm (\omega_{B_i} - 2\Omega))}}} \right]^{\frac{1}{2}}. \quad (13)$$

134

The propagation in the plasma shell of a pulsar of strong electromagnetic waves also leads to an increase in the fluctuations of electron density. To find the correlation functions with allowance for the self-consistent field between particles in accordance with the general theory of fluctuations, let us introduce into the right sides of the kinetic equations the random forces [7]:

$$\frac{\partial f_e}{\partial t} + (v \nabla) f_e - \frac{e}{m_e} E \frac{\partial f_e}{\partial v} - v \times (\omega_{B_e} - 2\Omega) \frac{\partial f_e}{\partial v} = y + v_e (f_{0e} - f_e), \quad (14)$$

$$\frac{\partial f_i}{\partial t} + (v \nabla) f_i + \frac{e}{m_i} E \frac{\partial f_i}{\partial v} + v \times (\omega_{B_i} + 2\Omega) \frac{\partial f_i}{\partial v} = y_i + v_i (f_{0i} - f_i).$$

Here  $y_\alpha$  represents the random forces. By normalizing the random forces

$$\langle y_\alpha(r, v, t), y_{\alpha'}(r', v', t') \rangle = \\ = 2v_\alpha \delta_{\alpha\alpha'} f_{0\alpha} \delta(v - v') \delta(r - r') \delta(t - t'),$$

from system (14) we obtain an expression for the correlator of the longitudinal electric field (8)

$$\langle E^2 \rangle_{k\omega} = \frac{(8\pi^2 e)^2}{m_e^2 \omega^2 (\omega, k)} \pi \delta[\text{Re } \xi_e(\omega, k)] \times \\ \times \sum_{\alpha, n} \int_0^\infty v_\perp dv_\perp \int_{-\infty}^\infty dv_\parallel f_{0\alpha}(v_\parallel, v_\perp) J_n^2(\beta_\alpha) \delta[\omega - k_\parallel v_\parallel - n(\omega_{B_\alpha} + 2\Omega)]. \quad (15)$$

From Eqs. (10), (14), and (15) we get

$$\langle E^2 \rangle_{k\omega} = 8\pi^2 \omega \frac{T_e}{|1 - (v_0/v_{\phi 1,2} \cos \theta)|} \frac{k^2 a_e^2 |\omega^2 - (\omega_{Bi} + 2\Omega)^2|}{|\omega_1^2 - \omega_2^2| (1 + k^2 a_e^2)} \times \\ \times \{ \delta(\omega^2 - \omega_1^2) + \delta(\omega^2 - \omega_2^2) \}. \quad (16)$$

Let us consider the scattering of electromagnetic waves in a plasma when an external magnetic field is present, which occurs mainly in electron density fluctuations. The scattering cross-section [7] is

$$d\Sigma = \frac{1}{2\pi} \frac{e^4}{m^2 c^4} \frac{\omega_0^2 \omega^2}{\omega_{Le}^2} R(\eta) \langle \delta n_e^2 \rangle_{q\Delta\omega_0} d\omega_0 d\tau, \quad (17)$$

where

$$\langle \delta n_e^2 \rangle_{q\Delta\omega_0} = \frac{2\pi n_0 e^2}{|1 - (v_0/v_{\phi 1,2} \cos \theta)|} \times \frac{1}{\Delta\omega (1 + q^2 a_e^2)} \times \\ \times \frac{\Delta\omega |\Delta\omega^2 - (\omega_{Bi} + 2\Omega)^2|}{|\omega_1^2 - \omega_2^2|} [\delta(\Delta\omega^2 - \omega_1^2) + \delta(\Delta\omega^2 - \omega_2^2)],$$

the quantities  $q$  and  $\Delta\omega_0$  denote change in wave vector and frequency in the wave scattering.

Data of pulsar observations [1-5] indicate that pulses of radio emission consist of series of subpulses. Variations in pulse amplitude occur more rapidly at lower frequencies. The effects observed can be associated with processes occurring in the plasma shell of a pulsar upon the passage of a strong electromagnetic wave. According to [11], when  $\omega > E_{cr}^2/8\pi$ , oscillations are excited in the plasma shell of a pulsar. Part of the energy of the electromagnetic wave will be lost in the excitation of longitudinal oscillations. Fluctuations in electron density and the scattering cross-section of the electromagnetic waves will be correspondingly increased. The fine structure of the pulsar radio pulses will develop (each pulse consists of a series of subpulses). For these phenomena to occur, it is necessary that the inequalities  $\omega > E_{cr}^2/8\pi$  be satisfied. Setting  $T_e \sim 10^6 - 10^7$  °K,  $\omega_0 \sim 10^8 - 10^9$  sec<sup>-1</sup>, we get  $E_{cr}^2/8\pi \sim 1-10$  erg/cm<sup>3</sup>. The intensity of pulsar radio emission  $N \sim 10^{30}$  erg/sec [4-5]. The total energy in the pulse  $\epsilon \sim 3 \cdot 10^{28}$  erg. The emitting volume  $V \sim 10^{26}$  cm<sup>3</sup>. The density of emission energy  $W \sim 10^2$  erg/cm<sup>3</sup>. These estimates show that the inequality  $W > E_{cr}^2/8\pi$  is satisfied over a wide frequency range.

#### Nature of Pulsar Radio Emission

In the preceding section, in analyzing the fine structure of pulsar radio pulses, we were not interested in the mechanisms

of radio emission. Here let us examine one of the possible radio emission mechanisms. Some authors [6, 8-10] have attempted to account for pulsar radio emission. In [6] radio emission caused by plasma oscillations of a stream emanating from the poles of a neutron star is examined; in [8] -- electromagnetic emission of a thin current layer at the borderline of vacuum and relativistic plasma oscillating at a low frequency. The study [9] examines a pulsar model in which the main radio emission mechanism is turbulence of anisotropic plasma which forms owing to two-beam instability in the neighborhood of a light cylinder of a rotating magnetic star. In most studies, beam or helical instability is considered as the radio emission mechanism, leading to the generation of plasma waves, which after conversion give off radio emission. Below we examine the mechanism that directly produces radio waves, in particular, the mechanism of the rotating and pulsating star, which is a neutron star with a dipolar or more complex magnetic field. There is no rigorous support for this model. However, certain qualitative considerations can be in favor of it. We know that at least some pulsars have two periods. Usually, the longer is associated with the rotation of the pulsar, and the shorter -- with its pulsations. In a pulsating magnetic field charge particles must undergo acceleration. First of all, the acceleration can occur in the time of "magnetic pumping": if the field of intensity changes slowly, the pulse components obey the relations

$$\frac{P_{\perp}}{B} = \text{const}, P_{\parallel} = \text{const}.$$

With increase in the magnetic field, the pulse component perpendicular to the field (and therefore, the total pulse) increases [11]. Secondly, particles can accelerate due to dynamic dissipation of the magnetic field [12]. Accelerated particles lead to the formation of radiation belts; particles from the radiation belts are flung off in the form of "jets" during the period of pulsations. How the pulsation of the entire surface of the star actually occurs, we do not know. However, we can imagine that the oscillating surface produces in the stellar atmosphere a pressure wave; then, when the wave enters the more rarefied atmosphere, the pressure wave changes into a shock wave, under whose effect the particles in the radiation belts are "flung off" in the polar regions owing to a disturbance of the adiabatic invariant. As a result, relativistic electron streams are produced in the polar regions of the upper atmosphere, which will travel in spiral orbits around curved force lines of the magnetic field issuing from the magnetic poles of the pulsars. Therefore electromagnetic streams in the general case are curved.



We have considered the model of the rotating and pulsating star which is a neutral star with a dipolar or more complicated magnetic field. In order for relativistic electron streams to be produced in the pulsar atmosphere, it is not necessary that the star be pulsating. For example, in the study [16], the basis of examination is taken as the model of a rotating magnetic neutral star whose magnetic field is symmetric relative to the axis of rotation. It is shown in this study that electrons accelerate along curved force lines of the magnetic fields. Other models of pulsars can also be proposed and can be shown that the generation of electron streams along force lines of the magnetic field issuing from the magnetic poles of pulsars will occur. Thus, our results (cf. below) are not a consequence of choosing a particular pulsar model. /36

To describe the instability dynamics, let us use the relativistic equation for electrons

$$\frac{d\mathbf{v}}{dt} + (\mathbf{v} \cdot \nabla) \mathbf{v} = - \frac{e}{m_e} \sqrt{1 - \frac{v^2}{c^2}} \left\{ E + \frac{1}{c} \mathbf{v} \times \mathbf{B} - \frac{v}{c} (\mathbf{v} \cdot \nabla) E \right\} \quad (18)$$

and the Maxwell equation for the electromagnetic field

$$\begin{aligned} \text{rot } \mathbf{B} &= \frac{1}{c} \frac{\partial \mathbf{B}}{\partial t} - \frac{4\pi e}{c} \rho \mathbf{v}, \quad \text{rot } \mathbf{E} = - \frac{1}{c} \frac{\partial \mathbf{B}}{\partial t}, \\ \text{div } \mathbf{E} &= -4\pi e (\rho - \rho_0), \quad \text{div } \mathbf{B} = 0, \end{aligned} \quad (19)$$

where  $\rho_0$  is the density of the compensating ions. The dispersion equation of the system (18) - (19) has been analyzed in [13]. The increment of instability built-up is of the form

$$\gamma = \omega_L \omega_H \beta_{\parallel} \beta_{\perp} [(k^2 v_{\parallel}^2 + \omega_H^2 \kappa^2) / (-\xi_- \xi_+)]^{\frac{1}{2}}, \quad (20)$$

where

$$\begin{aligned} \omega_L^2 &= \frac{4\pi e^2 \rho_0}{m \kappa}, \quad \beta_{\perp, \parallel} = \frac{v_{\perp, \parallel}}{c}, \quad \kappa = (1 - \beta_{\parallel} - \beta_{\perp})^{-\frac{1}{2}}, \\ \omega_H &= \frac{e B_0}{m_e c}, \quad \xi_{\pm} = (\omega \pm \omega_H)^2 - \beta_{\parallel}^2 \omega^2. \end{aligned}$$

From this it follows that instability occurs in the frequency range

$$\frac{\omega_H}{1 + \beta_{\parallel}} < \omega < \frac{\omega_H}{1 - \beta_{\parallel}}.$$

Pulsar emission is observed over a wide frequency range. For example, the pulsar CP 1919 is observed in the frequency range from 40 MHz ( $\lambda = 7.5$  m) to 3000 MHz ( $\lambda = 10$  cm) [4].

The pulsar MP 0628 is observed at the frequency 86 and 105 MHz [14]. To obtain the observed frequency band, we must set  $B = (10-10^2)$  gauss. For a relatively light neutron star with a radius of the compact core  $r \sim 10^7$  cm and a field  $B \sim 10^8$  gauss, the intensity of the dipolar magnetic field  $B \sim 10$  gauss at the surface of the plasma shell of the star at the distance  $r \sim 10^8$  cm.

# REFERENCES

1. Hewish, A. et al., Nature, 217, 709 (1968).
2. Hewish, A. Zemlya i Vselennaya, 2, 19 (1971).
3. Craft, H., Comella, J., and Drake, F., Nature, 218, 1122 (1968).
4. Hewish, A., UFN, 98, 715 (1969).
5. Ginzburg, V. L., Zheleznyakov, V. ., and Zaytsev, V. V., UFN, 98, 201 (1969).
6. Ginzburg, V. L., and Rukhadze, A. A., Volny v Magnitoaktivnoy Plazme (Waves in Magnetically Active Plasma ), Nauka Press, 1970.
7. Sitenko, A. G., Elektromagnitnyye Fluktuatsii v Plazme (Electromagnetic Fluctuations in Plasma), Khar'kov University Press, 1965.
8. Lerche, J., Astrophys. J., 159, 229 (1970).
9. Gold, T., Nature, 218, 335 (1968)
10. Good, M., Nature, 221, 250 (1968).
11. Al'fven, G., and Fel'tkhammar, K.-G., Kosmicheskaya Elektrodinamika (Space Electrodynamics), Mir Press, Moscow, 1967.
12. Syrovatskiy, S. N., Astr. zhurn., 43, 340 (1966).
13. Kotsarenko, N. Ya., Koshevaya, S. V., and Yukhimuk, A. K., Geomagnetizm i aeronomiya, 10, 715 (1970).
14. Vitkevich, V. V., and Shishov, Yu. P., DAN SSSR, 195, 53 (1970).
15. Lenert, B., Dinamika Zaryazhennykh Chastits (Dynamics of Charged Particles), Atomizdat, Moscow, 1967.
16. Goldreich, P., and Julian, W., Astrophys. J., 157, 869 (1969).

# DIURNAL AND SEASONAL TRENDS IN THE INCIDENCE OF SUDDEN COMMENCEMENTS (SC) AND SUDDEN IMPULSES (SI)

/37

E. I. Nesmyanovich

It has now been established that sudden commencements and impulses are caused by disturbances of the interplanetary plasma. In particular, in the study [11], of 19 disturbances considered, 11 were unambiguously identified with geomagnetic phenomena. Here, SC corresponded to seven cases of shock waves, and SI -- to four discontinuities of the interplanetary plasma. In eight cases, no unique correlation of disturbances (five shock waves and three discontinuities) with geomagnetic events could be made, since from ground station observations they were produced by both SC and SI, simultaneously.

This situation is typical of many geomagnetic disturbances. Therefore, SC and SI are similar in their nature. This means that in the incidence of SI, we can expect the same features as for SC. The paper [2] shows that there is a diurnal and seasonal trend in the incidence of SC. A similar investigation was made for SI. This work presents the findings, as well as a fuller analysis of the diurnal and seasonal trends in the incidence of SC and SI.

Table 1

Таблица 1																
Geomag- netic Disturb.	Year															Total
	1955	1956	1957	1958	1959	1960	1961	1962	1963	1964	1965	1966	1967	1968		
$SC_1$	13	62	61	46	52	59	39	23	23	33	38	44	39	44	576	
$SC_{1k}$	9	27	32	20	24	36	20	9	7	15	19	20	23	24	285	
$SC_2$	4	9	11	44	—	—	33	22	23	22	30	37	52	31	318	
$SC_1 + SC_2$	17	71	72	90	52	59	72	45	46	55	68	81	91	75	894	
$SI_1$	25	35	111	186	61	61	38	34	39	31	40	47	54	50	812	
$SI_2$	62	46	38	36	89	84	100	83	97	98	132	133	162	180	1340	
$SI_1 + SI_2$	87	81	152	222	150	145	138	117	136	129	172	180	216	230	2152	

From 1  
January 1955  
to 31 December  
1968, informa-  
tion was col-  
lected on 894  
cases of SC  
and 2152 cases  
of SI from the  
data published  
in [3, 4].

All SC  
and SI are  
subdivided  
into two groups,  
by the confi-  
dence level.  
The first SC<sub>1</sub>  
and SI<sub>1</sub> were  
recorded simul-  
taneously at

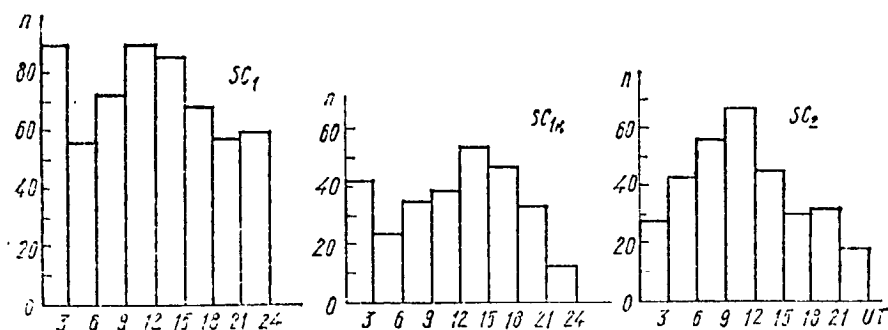


Fig. 1. Diurnal trend of  $SC_1$ ,  $SC_{1k}$ , and  $SC_2$

and  $SI_2$  detected by a small number of stations.

From the  $SC_1$  group, a subgroup of the most reliable  $SC_{1k}$  was singled out, which were entered on the covers of  $K_p$ -indexes, also published in [3, 4]. The data on each group of SC and SI, beginning from 1961, are found in [3] individually. For preceding years, the separation was made independently.

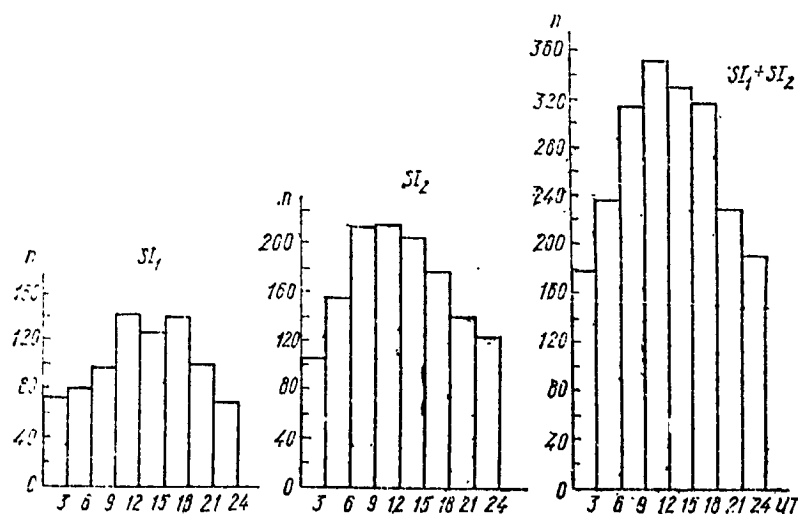


Fig. 2. Diurnal trend of  $SI_1$ ,  $SI_2$ , and  $SI_1 + SI_2$

Table 1 presents the annular numbers of events for each group of SI and SC. Clearly, the variation in the number of cases with the cycle of solar activity is more pronounced for  $SI_1$  and  $SI_{1k}$ , and  $SI = SI_1 + SC_2$ . When a comparison is made of the annual numbers of  $SC_1$ ,

$SC_{1k}$ , and SI with the data on the different manifestations of solar activity [3], it is clear that they correlate more closely with the trend in the annual numbers of cosmic, subcosmic, and protonic flares, and also with the number of atmospheric flares in a single hour of observations.

magnetic stations located at different longitudes. These events are of the general-planetary kind and are usually recorded by no fewer than 50-60 stations. The second group includes  $SC_2$

Table 1

Geomagnetic disturbance	Month											
	I	II	III	IV	V	VI	VII	VIII	IX	X	XI	XII
$SC_1$	53	51	51	49	46	47	48	40	56	39	50	45
$SC_{1k}$	22	27	19	30	33	20	33	27	24	18	18	14
$SC_2$	28	26	31	22	21	32	24	26	28	31	26	22
$SC_1 + SC_2$	81	77	82	71	67	79	72	66	84	70	76	67
$SI_1$	61	71	67	63	7	85	67	71	77	63	54	66
$SI_2$	108	137	124	120	119	131	99	112	116	96	82	92
$SI_1 + SI_2$	169	208	191	183	190	216	166	183	193	159	136	158

Таблица 2

The increase during these years of the activity maximum is well-defined for all these events. To find the diurnal trend in the incidence of SC and SI recording, a count was made of the number of these events in each three-hour interval of world time.

Fig. 1 presents distribution histograms for  $SC_1$ ,  $SC_{1k}$ , and  $SC_2$ , respectively.

The diurnal trend exists for all distributions. Here the maximum in the incidence of  $SC_{1k}$  recording is shifted by one three-hour interval.

Fig. 2 gives the distribution histograms of  $SI_1$ ,  $SI_2$ , and  $SI$ .

/39

The diurnal trend is also well-defined for the sudden impulses, but it differs somewhat from the diurnal trend of  $SC_1$ , and  $SC_{1k}$ , and has a single maximum, as does  $SC_2$ . For  $SI$  and  $SI_1$  it occurs at (09-18)<sup>h</sup> UT; for  $SI_2$ , the maximum is shifted by a single three-hour interval and occurs at (06-15)<sup>h</sup> UT.

The similarity of the histogram of the diurnal trend for all distributions SC and SI, and especially for  $SC_2$  and  $SI_2$  once again indicates the close similarity of the geomagnetic disturbances.

To resolve the question of the reliability of the resulting distributions, a check was made of the hypothesis of the uniform distribution, using the Kolmogorov agreement criterion [6]. All distributions with a 0.98 probability do not satisfy the uniform distribution.

Table 3

Таблица 3

Period of year	Geomagnetic disturbance	Interval of day								Period of year	Geomagnetic disturbance	Interval of day							
		Interval of day										Interval of day							
		1	2	3	4	5	6	7	8			1	2	3	4	5	6	7	8
I	$SC_1$	48	27	38	46	47	30	25	27	II	$SC_1$	41	29	34	44	38	31	33	
	$SC_2$	10	22	27	40	22	18	19	7		$SC_2$	18	21	29	27	23	12	12	11
	$SC_1 + SC_2$	58	49	65	86	69	43	44	34		$SC_1 + SC_2$	59	50	63	71	61	50	43	44
	$SI_1$	37	38	51	67	70	73	45	31		$SI_1$	36	44	48	72	55	65	46	38
	$SI_2$	57	71	114	121	102	91	86	63		$SI_2$	48	75	100	94	103	87	54	60
	$SI_1 + SI_2$	94	109	165	183	172	164	131	94		$SI_1 + SI_2$	84	119	148	166	158	152	100	98

Thus, the diurnal trend in the incidence of recordings of SC and SI is real, although in [7, 8] the dependence of the time of the appearance of SC on the hour of the day was not detected.

From these same data, a study was made of the seasonal trend of the recording frequency of SC and SI.

Table 2 gives the distributions of the days of the month for all SC and SI groups. From the table it follows that the seasonal trend for all distributions of SC and SI, except for SC<sub>1k</sub>, is practically absent. These distributions satisfy the uniform distribution with the probability of 0.99. As for the distribution of SC<sub>1k</sub> events, they are more probable in spring and summer.

The seasonal character is more pronounced in the variation of the diurnal trend of SC with sign. This conclusion follows from Table 3, where the diurnal trend is given for two periods of the year. The first -- equinox -- covers February, March, April, August, September, October, and second -- the rest of the year. The diurnal trend of SC is more pronounced during the first period. This variation in diurnal trend as a function of season was not detected for SI.

Thus, the recording frequency of SI, as well as SC, is controlled by world time.

This result can be accounted for by the selection of observations, as a result of which the diurnal trend based on world time is the result of superimposing the diurnal trend in local time upon the nonuniform distribution of magnetic stations considered by longitude.

Most stations are in Europe; here SC and SI are recorded most frequently. But this assumption can be made only relative to the events SC<sub>2</sub> and SI<sub>2</sub>. SC<sub>1</sub> and SI<sub>1</sub> are general-planetary in nature, and the diurnal trend cannot be explained by observational selection. In addition, our results can be accounted for by the infiltration of some of the events SC and SI by the Earth's magnetosphere, which can be due to the asymmetry of the geomagnetic field relative to the axis of rotation and the plane of the Earth's equator.

/40

The second explanation is more applicable for the events SC<sub>1</sub> and SI<sub>1</sub>.

These results lead to the conclusion that the presence or the absence of SC and SI during geomagnetic storms is determined not only by the nature of the corpuscular stream, by the presence of shock waves and tangential discontinuities, but also by purely terrestrial conditions (independently of the explanation of the nature of the diurnal trend). And this once again confirms that



the division of storms into two types by the nature of their commencement -- sudden or gradual -- is highly arbitrary and cannot be a criterion for determining the nature of the corpuscular source. Evidently, there are no appreciable differences between sources responsible for sporadic and recurrent storms, since a sudden commencement is equally probable for both kinds of storms.

# REFERENCES

1. Burloga, L. F., and Ogilvie, K. W., J. Geophys. Res., 74(11), 2815 (1969)
2. Nesmyanovich, A. T., and Nesmyanovich, E. I., Geomagnitizm i aeronomiya, No. 1, 181 (1971).
3. JAGA Bulletin, No. 12k, (1959); No. 12l, (1960); No. 12n 2, (1963); No. 12o 2, (1965); No. 12p 2, (1966); No. 12q 2, (1967); No. 12r 2, (1967); No. 12t 2, (1968); No. 12u 2, (1969); No. 12w 1, (1970); No. 12w 2, (1971).
4. "Geomagnetic and Solar Data," J. Geophys. Res., 1955-1969.
5. Afanas'yeva, V. I., Geomagnitizm i aeronomiya, No. 9, 699 (1969).
6. Shchigolev, V. M., Matematicheskaya obrabotka nablyudeniy (Mathematical Treatment of Observations), Fizmatgiz, 1960.
7. Afanas'yeva, V. I., Geomagnitizm i aeronomiya, No. 9, 947 (1969).
8. Mishin, V. M. et al., Magnitnyye buri (Magnetic storms). USSR Academy of Sciences Press, 1963.

N. 2. 1.

CHROMOSPHERIC FLARES AND SUDDEN COMMENCEMENTS  
OF GEOMAGNETIC STORMS

/40

A. T. Nesmyanovich and E. I. Nesmyanovich

The relationship between geophysical phenomena and chromospheric flares has long been investigated, and many authors already this obvious and not requiring any argumentation.

As a rule, this relationship is sought for in time, that is, if there is a chromospheric flare in one - three days before a SC, then an effort is made to correlate it with this event [1, 2]. However, this correspondence is not free of contradictions. It must be noted that SC are observed also in those periods of time when there are no flares on the sun and, conversely, flares, even of scale 2-3, do not cause SE. The problem needs additional exploration.

This paper attempts to find statistical correlations of SC with chromospheric flares. The spatial correlation between SC and chromospheric flares appear to us more probable, that is, the relationship between SC and the moment of traversing across the center of mass of the corresponding active region in which the flares occurred.

After transiting the central meridian [CM] by an active flare region, a geomagnetic disturbance or storm begins on the second day [3, 4]. From these results it follows that chromospheric flares or processes accompanying them produce quasi-steady directional streams. The latter are responsible both for sporadic and recurrent storms in which the presence of sudden commencements is equally probable. The periodicity of the SC events cannot be correlated with the random nature of the distribution of flares in time.

/41

This study was made under two assumptions: that a time or spatial correlation exists between chromospheric flares and SE.

In order to make convincing correspondences, a great deal of observation material is needed. For this purpose, the authors compiled a catalog of daily flare activity over 10 years, from June 1957 to June 1967. The material for the catalog consisted of the following: they previously published Dodson catalog [5], which includes data on all flares since June 1957 to December 1962, and data from [6] for subsequent years. Included in the catalog, in addition information on the number of flares

61

observed daily (presented separately by scale division 1, 2, and 3), contains data on the number of flares in each meridional zone of  $14^\circ$  width, which corresponds to a change in heliographic latitude of one day. Data are presented both on the number of flares recorded during the entire period up to the traversing by the zone of the CM, including the day of transit, as well as the number of flares noted in the zone in the next six days. The flares were also divided into two groups, depending on the sign of the hemisphere, northern or southern. From the catalog one can easily single out the helio-effective longitudes that correspond to the transit across the CM of regions with maximum flare activity. A total of 28,456 flares were recorded in the catalog.

Table 1 presents the number of flares by years and the data on SC from [7].

Table 1

Year	No. of fl., scale div.				SC			
	1	2	3	Total	SC <sub>1</sub>	SC <sub>1,2</sub>	SC <sub>2</sub>	SC <sub>1</sub> + SC <sub>2</sub>
1957*	2271	168	19	2458	61	32	11	72
58	3580	299	20	4198	46	20	44	90
59	3118	233	30	3387	52	24	—	52
1960	2931	118	19	2168	59	36	—	59
61	1081	55	10	1129	39	20	33	72
62	631	32	2	665	23	9	22	45
63	1932	86	11	2029	23	7	23	46
64	1173	15	1	1189	33	15	22	55
65	1871	37	1	1909	38	19	30	68
66	4641	153	26	4820	44	20	37	81
67**	4316	156	32	4504	—	23	—	—
Total	26944	1341	171	28456	418	225	222	641

\* Flares during July-December 1957.

\*\* Flares during January-June 1967.

As we can see from Table 1, the trend is strongly correlated with the cycle. However, no absolute value can be given to the numbers, since the material is not uniform enough. As follows from [5], included among scale division 1 flares recorded is a pronounced diurnal trend, which indicates observational selectivity. Dur-

ing the winter periods there were no observations for certain intervals of time. Moreover, beginning from 1966, scale division 1 flares were included. However, the material is quite suitable for comparing SC events with chromospheric flares, since here short periods are investigated (six days before SF and six days thereafter) and during this time the data acquisition system remained practically unchanged.

The data presented on SC are sufficiently complete; they are based on materials of the international service. Here all SE are divided into two groups by the confidence level. The first includes SC<sub>1</sub> recorded at a large number of stations. They are general-planetary in nature. Of these, SC<sub>1k</sub> are singled out -- these are SC which are entered on the covers of the K<sub>p</sub>-indexes, being the most reliably recorded.

The second group is composed of SC<sub>2</sub> recorded only at several magnetic stations. In this work, only SC<sub>1k</sub> were used in the analysis, a total of 190 events. (If two SC occurred on the same day, the second was not considered.)

/42

To solve the problem of the reliability of any particular assumption, the nature of the flare activity during the period of the SC event was studied. For this purpose, a plot of the flare activity six days before and six days after the SC was constructed by the superimposed epoch technique (SET) for each SC. The zero day corresponded to the SC event. In Fig. 1 are presented the corresponding histograms for each scale division considered separately. Histograms were obtained by this method in Fig. 2. However, here in place of the daily number of flares, the number of flares in each 14-degree meridional zone was used. In the figure, the days are laid out along the axis instead of the longitudes. The zero day corresponds to the zone which transited across the CM on the day of the SC. Here, for Fig. 2 only the flares occurring in the given zone before its transit across the CM or on the day of transit were used.

From Fig. 1 a we see that the distribution of scale division 1 flares during the period preceding the SC satisfies the equiprobable distribution. A verification of the seven-day section using the Kolmogorov criterion  $\lambda$  shows that it satisfies the equilibrium distribution with a confidence level of 0.96. Some decrease on the 3<sup>d</sup> and subsequent days can be accounted for by the departure beyond the western limb of the corresponding active region which transited the CM on -3<sup>d</sup>. An individual correspondence of scale division 1 flares with C is in practice precluded, since on the average each day 10 flares were recorded. As for scale division 2 and 3 flares, a small maximum can be distinguished in the days preceding the SC. The statistical significance of the extremal values for the resulting distribution was estimated with the Student's t-criterion [8]. For scale division 2, the maximum in the distribution is statistically not significant, but for scale division 3, it is real with a confidence level 0.99.

/43

Nonetheless, this does not prove a close correlation of SC with scale division 3 flares. As we can see from Table 1, over the entire 11-year period 171 scale division 3 flares were recorded, about 30 percent of the number of SC events.

For a more detailed correspondence, an analysis was made of the incidence of scale division 2 and 3 flares on the eve of a SC (Table 2).

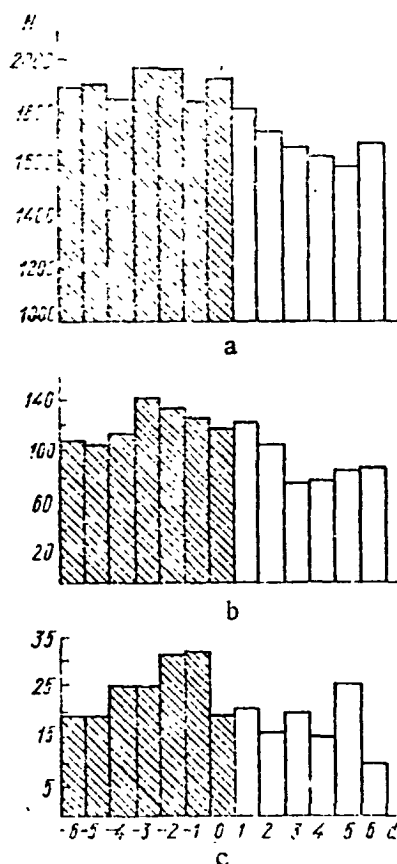


Fig. 1. Distribution of number of flares in a period of 190 cases of SC, plotted by the SET. The day of the SC is taken as zero. Histogram a was plotted for flares of scale division 1, b -- scale division 2, and c -- scale division 3.

From Table 2 we can also see that the incidence of flares in groups of six and seven and higher significantly exceed the anticipated value. It is possible that observational selection is at work here. This can also be accounted for by a rise in the histograms (Fig. 1 b and c). But this problem needs additional investigation, although it can be said that the number of bright flares here showed practically no increase. The complex situation in

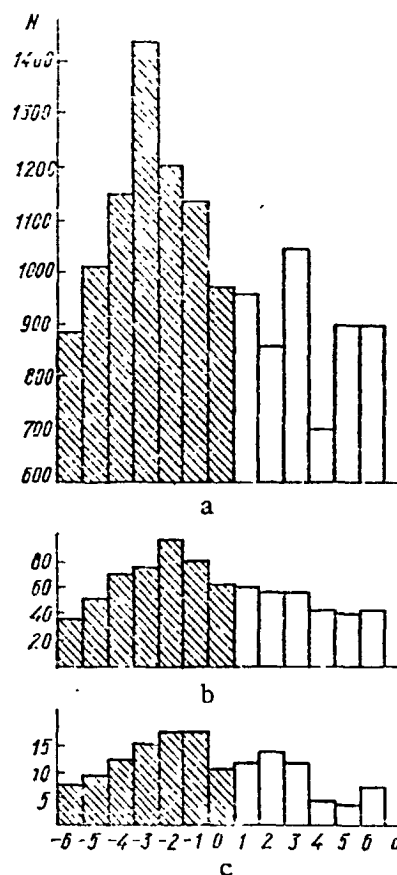


Fig. 2. Distribution of flares by 14-degree zones in the period of 190 cases of SC, plotted by the SET. The zero day corresponds to the zone that transited the CM on the day of the SC.

This distribution used only those flares that occurred in each zone before its presence across the CM or on the day of the transit. The histogram a was plotted for scale division 1 flares, b -- scale division 2, and c -- scale division 3.

Table 2

Number of flares	-3-1 <sup>d</sup>			-1-1 <sup>d</sup>			+1-+3 <sup>d</sup>			+1-+3 <sup>d</sup>		
	1	2	3	1	2	3	1	2	3	1	2	3
0	73	153	60	48	119	42	83	155	84	64	135	62
1	24	33	34	24	32	22	29	22	29	29	30	23
2	39	11	26	18	13	18	21	5	25	24	13	26
3	16	7	17	13	13	12	17	5	14	18	8	16
4	11	1	14	25	7	18	10	1	14	12	0	12
5	6		9	11	3	11	6	1	5	13	4	11
6	6		8	5	2	11	5		4	4	0	7
7 and higher	16		22	45	1	55	8		14	28	0	34

\* The figures 2-3 denote the scale division of the flares.

which a group of flares was recorded on the eve of a SC does not permit a unique correspondence of SC and the flares. In some studies, in the correspondence use was made of the additional criteria: the

position of the flares and their relationship with radio bursts, especially of the type IV [1]. Though these correspondences appear more convincing, the number of bright flares on the eve of the SC, already insufficient, is reduced in this procedure.

Thus, from this analysis it follows that it is virtually impossible to establish a dependable relationship between individual flares and SC, that is, there is no time correlation between these events. At the same time, an analysis of histograms obtained under the second assumption affords grounds for regarding it as quite justified. A maximum occurring on -3<sup>d</sup> is well defined on all distributions. And this means that the SC generally commences three days after the transiting across the CM of the geographic longitude, that is, of the zone with maximum flare activity. A check of the statistical significance of all extremal values using Student's t-criterion affords grounds to regard them as nonrandom with a confidence level 0.99.

The high statistical significance of all extremal values in the distributions (see Fig. 2) allows us to accept as wholly realistic a correlation between SC and the geoeffective longitude. Analysis of all individual distributions used as the basis for constructing the histograms (Fig. 2) shows that only in four out of 190 cases is there an absence of a well-defined maximum that would make it possible to establish the moment of transiting across the CM of the corresponding geoeffective longitude. In the remaining cases, we can establish this longitude, which as a rule transited the CM in three days, but in some cases earlier or later, so that the scatter between the extreme points corresponds to five days.

/44

When a comparison is made of each of the 47 cases (noted in Table 2) when scale division 3 flares were observed on the eve of the SC in one to three days, it is clear that they all coincide with the period of transiting across the CM of the geoeffective longitude, this means that using these cases in general one cannot draw unique conclusions on the correlation between flares and SC. Here both assumptions are probable. This must be anticipated, since the absence of any correlation and with the random nature of the flare distribution in time, 25 percent of them occur in each three-day interval, including also on the eve of a SC (the flare region is observed on the disk on the average in 13 days). As for the four cases for which there is no possibility of determining the geoeffective latitude from the data seven days before the SC, they are readily accounted for if one considers the situation during the preceding seven days.

Based on this analysis, one can find the following conclusions:

1. There is no statistically significant time correlation between SC and chromospheric flares. Therefore, during the period of lag of the SC with respect to any closest flares, no conclusions of any kind can be made about the rate of propagation of shock waves or of the solar plasma in the space between Sun and Earth, as is done in [2].

2. Assuming that a shock wave is responsible for SC propagates over the entire hemisphere [9] is in no way supported and contradicts the fact that SC are often associated with the current storms that can be caused only by quasisteady oriented corpuscular streams.

3. A statistically significant spatial correlation has been established between SC and flares. These results agree closely with those obtained earlier in [3, 4], where it was shown that on the second day after the transiting by a flare-active region of the CM a geomagnetic storm with gradual or sudden commencement began.

Chromospheric flares or processes accompanying them produce quasisteady oriented corpuscular streams -- quasisteady in the sense that the accelerated outflowing of plasma from the flare region will last much longer than the flare duration. Direct measurements of interplanetary plasma shows that the velocity of the solar wind continues to rise even after the transiting of the helium-enriched plasma, which most likely was generated by the flare [10].

4. The SC are caused by shock waves or tangential discontinuities that form at the western boundary of the corpuscular stream or at the boundary between the sectors. Here the shock



---

wave cannot be the result of an isolated explosion associated with the flare, since a 27-day periodic repetition is characteristic of SC.

Conditions of the continuous generation of shock waves exist at the boundary of the stream. This conclusion agrees well with those drawn in [11]. The latter study showed that high-energy protons are also continuously generated and are observed only in the oriented streams which the Earth encounter every 27 days.

# REFERENCES

1. Levitskiy, L. S., Izv. KrAO, No. 41-42, 203 (1970).
2. Gaylor, A. E., Solar Physics, 6(2), 320 (1969).
3. Nesmyanovich, A. T., Astron. vestnik, 2(1), 48 (1968).
4. Nesmyanovich, A. T., and Chmil', A. V., Astron. vesnik, 3(3), 45  
1951 (1961).
5. Dodson, R. R., and Hedeman, E. R., Solar Activity Report Series,  
No. 12, (1960); No. 15, (1961).
6. "Solar and Geophysical Data," J. Geophys. Res., 1957-1967.
7. Nesmyanovich, A. T., and Nesmyanovich, E. I., Geomagnitizm i  
aeionomiya, 11(1), (1971).
8. Brukts, K., and Karuzers, N., Primeneniye statisticheskikh  
metodov v meteorologii (Statistical Methods in Meteorology),  
GMI, Leningrad, 1963.
9. Parker, Ye., Dinamicheskiye protsessy v mezhplanetnoy srede  
(Dynamic Processes in the Interplanetary Medium), "Mir",  
1965.
10. Hirshberg, J., J. Geophys. Res., 75(1), 1 (1970).
11. Pick, M., Solar Terrestr. Phys., 1970; Proc. Int. Symp.,  
Leningrad, 1970; Dordrecht, 1972, pp 1, 61.

N74-28271

ACCELERATION OF SOLAR COSMIC RAYS  
DURING CHROMOSPHERIC FLARES

/45

L. I. Dorman, L. B. Raychenko, and A. K. Yukhimuk

In considering the acceleration of charged particles at the Sun, we have in mind that it occurs during periods of solar flares. Without dwelling on the mechanisms of solar flares, we note only the fact that during these periods the rapid transformation of magnetic energy into the energy of accelerated particles is observed [1]. Several studies deal with the acceleration of charged particles at the Sun [2-4]. The article [2] examines the acceleration of charged particles due to the dynamic dissipation of the magnetic field. In [3] the acceleration of particles by electromagnetic waves with variable velocity of propagation is investigated. The paper [4] discusses the acceleration of particles when plasma microinstabilities are present in the current layer. A flare is a discontinuity in the current layer followed by the generation of cosmic ray particles [4]. The present work considers one of the possible processes of the acceleration of solar cosmic rays, namely: the acceleration of charged particles by fluctuational electric fields of the low-frequency turbulence of solar plasma. In the conditions of space there are several mechanisms of the generation of longitudinal oscillations. Thus, the generation of longitudinal oscillations can be associated with the presence of the anisotropic velocity distribution of plasma particle [5]. Additionally, longitudinal oscillations can be generated by shock waves [6]. In this study we assume that the generation of longitudinal low-frequency oscillations in the solar atmosphere is due to the propagation of intense electromagnetic radiation generated during chromospheric flares. From experimental data [7-8], the presence of longitudinal waves in the plasma is often correlated with the presence of high-energy ions. Therefore it is useful to consider the acceleration of solar cosmic rays by the fluctuational fields of longitudinal waves.

We will assume that an electromagnetic wave of circular polarization is propagated in a plasma that is in a constant magnetic field  $H_0 = (0, 0, H)$ :

$$\begin{aligned} E_z &= \frac{1}{2} E_0 \exp i(k_0 z - \omega_0 t) + \text{c. c.}, \\ E_x &= \pm i E_0, \quad H_x = \pm \frac{CK_0}{\omega} F_y, \quad H_y = -\frac{CK_0}{\omega_0} E_x, \end{aligned} \quad (1)$$

where

$$K_0 = \frac{\omega_0}{c} \sqrt{\epsilon_z}, \quad \epsilon_z = 1 - \frac{\omega_{pe}^2}{\omega_0(\omega_0 \pm \omega_H + i\nu)}, \quad \omega_H = \frac{eH_0}{mc},$$

$\omega_{pe}$  is the Langmuir frequency of electrons, and  $\nu$  is the effective frequency of collisions of electrons with surrounding particles. The upper sign in (1) corresponds to the ordinary wave, and the lower -- to the extraordinary wave.

The propagation of the electromagnetic wave (1) is accompanied by the appearance of an increment in the electron distribution function to the Maxwellian function  $f_0$ : /46

$$f_1 = -i \frac{e}{mc} E_1 \frac{\frac{\partial f_0}{\partial v_1} e^{\pm i\varphi}}{k_0 v_z - \omega_0 \pm \omega_H - i\nu}, \quad (2)$$

where  $\phi$  is the polar angle in the velocity space.

The second-approximation equation for the electron distribution function is of the form:

$$\frac{\partial f_2}{\partial t} + (\mathbf{v} \nabla) f_2 - \frac{e}{m_e} [E_1 + \frac{1}{c} \mathbf{v} \times \vec{H}] \frac{\partial f_1}{\partial v} - (\mathbf{v} \times \omega_H) \frac{\partial f_2}{\partial v} = -\nu f_2. \quad (3)$$

Averaging Eq. (3) with respect to time, we get:

$$\nu f_2 - [\mathbf{v} \times \omega_H] \frac{\partial f_2}{\partial v} = \frac{e}{m} \left[ E_1 + \frac{1}{c} \mathbf{v} \times H_1 \right] \frac{\partial f_1}{\partial v}. \quad (4)$$

Substituting  $f_1$  in  $E_0$  from (1) and (2) in (4) and assuming  $ks_e \ll |\omega_0 \pm \omega_H|$ ,  $\nu \ll |\omega_0 \pm \omega_H|$ , we get the increment to the steady electron distribution function caused by the electromagnetic wave

$$f_2 = v_0 \left[ \frac{\omega_0}{k_0} \left( \frac{v_1^2}{s_e^2} - 1 \right) + v_z \right] \frac{2}{s_e^2} f_0, \quad (5)$$

where

$$v_0 = \frac{e^2 E_0^2 k_0}{m^2 \omega_0 (\omega_0 \pm \omega_H)^2}, \quad s_e = \sqrt{\frac{2T_e}{m}}. \quad (6)$$

Then the steady distribution function is of the form:

$$F_0 = \left\{ 1 + v_0 \left[ \frac{\omega_0}{k_0} \left( \frac{v_1^2}{s_e^2} - 1 \right) + v_z \right] \frac{2}{s_e^2} \right\} f_0. \quad (7)$$

We calculate the mean electron velocity by using the total steady function  $F_0 = f_0 + f_2$ :

$$\langle v \rangle = v_0 n, \quad n = \frac{\vec{k}_0}{k_0}. \quad (8)$$

Similarly, the calculated mean electron energy is

$$\langle \frac{mv^2}{2} \rangle = \frac{3}{2} T_e + \frac{mu^2}{2}, \quad (9)$$

where

$$u^2 = \frac{e^2 E_0^2}{m^2 (\omega_0 \pm \omega_H)^2}.$$

Let us consider longitudinal oscillations of the magnetized plasma when applied electromagnetic radiation is present. Let us write the kinetic equations of electrons and ions, with reference to the self-consistent field, as:

$$\begin{aligned} \frac{\partial f_e}{\partial t} + (v \nabla) f_e - \frac{e}{m_e} E \frac{\partial f_{0e}}{\partial v} + (\omega_{He} \times v) \frac{\partial f_e}{\partial v} &= 0, \\ \frac{\partial f_i}{\partial t} + (v \nabla) f_i + \frac{e}{m_i} E \frac{\partial f_{0i}}{\partial v} - (\omega_{Hi} \times v) \frac{\partial f_i}{\partial v} &= 0, \\ \text{div } E &= -4\pi e \left\{ \int f_e d\mathbf{v} - \int f_i d\mathbf{v} \right\}. \end{aligned} \quad (10)$$

47

The dispersion equation of system (10) is of the form:

$$\begin{aligned} 1 + \frac{1}{k^2 a_e^2} \left\{ 1 - e^{-\frac{\beta_e^2}{2}} \sum_{n=-\infty}^{\infty} \frac{Z_{e0}}{Z_{en}} I_n \left( \frac{\beta_e^2}{2} \right) [\varphi(Z_{en}) - i] \sqrt{\pi} Z_{en} e^{-Z_{en}^2} - \right. \\ \left. - \frac{2v_0 \omega_0}{s_e^2 k_0} Q(Z_{en}) \right\} + \frac{1}{k^2 a_e^2} \sum_{n=-\infty}^{\infty} \left\{ 1 - e^{-\frac{\beta_i^2}{2}} \frac{Z_{i0}}{Z_{in}} I_n \left( \frac{\beta_i^2}{2} \right) \times \right. \\ \left. \times [\varphi(Z_{in}) - i] \sqrt{\pi} Z_{in} e^{-Z_{in}^2} \right\} = 0, \end{aligned} \quad (11)$$

where

$$\begin{aligned} a_{e,i}^2 &= \frac{T_{e,i}}{4\pi e^2 n_0}, \quad \beta_{e,i} = \frac{k_{\perp} s_{e,i}}{\omega_{He,i}}, \quad s_{e,i}^2 = \frac{2T_{e,i}}{m_{e,i}}, \\ Z_{e,i,n} &= \frac{\omega + n\omega_{He,i}}{k_{\parallel} s_{e,i}}, \quad \varphi(Z) = 2Ze^{-Z^2} \int_0^Z e^{x^2} dx, \\ Q(Z_{en}) &= 1 + e^{-\frac{\beta_e^2}{2}} \sum_{n=-\infty}^{\infty} \left( 1 - \frac{k_0 s_e}{\omega_0} Z_{en} \right) I_n \left( \frac{\beta_e^2}{2} \right) - e^{-\frac{\beta_e^2}{2}} \sum_{n=-\infty}^{\infty} \left\{ \frac{k_0 s_e}{2\omega_0 Z_{en}} I_n - \right. \\ &\quad \left. - \frac{\beta_e^2}{2} [I_n + \frac{1}{2} (I_{n-1} + I_{n+1})] \right\} i [\varphi(Z_{en}) - i] \sqrt{\pi} Z_{en} e^{-Z_{en}^2}, \end{aligned} \quad (12)$$

$I_n(x)$  is a modified Bessel function of the  $n$ -th order;  $k_{\parallel} = k \cos \theta$ ,  $k_{\perp} = k \sin \theta$ ;  $\theta$  is the angle between  $k$  and  $H$  (the vector  $k$  lies in the  $xy$  plane).

For relative weak magnetic fields when electrons are magnetized ( $k_{\perp} s_e \ll \omega_{He}$ ), and the ions are not magnetized ( $k_{\perp} s_i \gg \omega_{Hi}$ ), the solution of the dispersion equation in the frequency range  $k_{\perp} s_i \ll \omega \ll k_{\perp} s_e$  is of the form:

$$\omega \equiv \omega_s(k) = \frac{kv_s}{\sqrt{1 + k^2 a_e^2}},$$

$$\gamma = \sqrt{\frac{\pi}{8} \frac{m_e}{m_i}} \frac{kv_s}{|\cos \theta| (1 + k^2 a_e^2)^{3/2}} \left(1 - \frac{v_0}{v_{\phi}} \cos \theta\right), \quad (13)$$

where

$$v_s = \sqrt{\frac{T_e}{m_i}}, \quad v_{\phi} = \frac{\omega_s}{k}.$$

For stronger magnetic fields, the ions can also be considered to be magnetized ( $k_{\perp} s_i \ll \omega_{Hi}$ ). Assuming that

$$s_i \ll \frac{\omega}{k \cos \theta} \ll s_e, \quad \frac{(\omega - \omega_{Hi})}{k s_i \cos \theta} \gg 1,$$

we can represent the solution of Eq. (11) as:

$$\omega_{1,2}^2 = \frac{1}{2} (\omega_s^2 + \omega_{Hi}^2) \pm \frac{1}{2} \sqrt{(\omega_s^2 + \omega_{Hi}^2)^2 - 4\omega_s^2 \omega_{Hi}^2 \cos^2 \theta},$$

$$\gamma_{1,2} = \sqrt{\frac{\pi}{8} \frac{m_e}{m_i}} \frac{\omega_{1,2}^2 \omega_s^2 (\omega_{1,2}^2 - \omega_{Hi}^2)}{k^3 v_s^3 |\cos \theta| (2\omega_{1,2}^2 - \omega_s^2 - \omega_{Hi}^2)} \left(1 - \frac{v_0}{v_{\phi 1,2}} \cos \theta\right). \quad (14)$$

Eqs. (14) give an expression for frequencies at the increment in longitudinal low-frequency waves in plasma, increasing when  $v_0 \cos \theta \gg v_{\phi 1,2}$ . From Eqs (6) and (14), let us find the critical amplitude of the high-frequency field  $E_{cr}$ , above which low-frequency longitudinal oscillations are written:

/48

$$E_{cr} = \frac{m_e}{e} |\omega_0 \pm \omega_{He}| \left\{ \frac{cv_{cp}}{\cos \theta \sqrt{1 - \frac{\omega_{pe}^2}{\omega_0 (\omega_0 \pm \omega_{He})}}} \right\}^{\frac{1}{2}}. \quad (15)$$

It must be expected that the propagation of electromagnetic waves in a plasma leads to a rise in the density fluctuations. To find the correlation functions with reference to the self-consistent

interaction between particles, under the general theory of fluctuations let us introduce into the right sides of kinetic equations (10) the random forces [10]

$$\begin{cases} \frac{\partial f_e}{\partial t} + (\mathbf{v} \nabla) f_e - \frac{e}{m_e} \left( E + \frac{1}{c} \mathbf{v} \times H \right) \frac{\partial f_e}{\partial v} = y_e - \nu_e (f_e - f_0), \\ \frac{\partial f_i}{\partial t} - (\mathbf{v} \nabla) f_i + \frac{e}{m_i} \left( E + \frac{1}{c} \mathbf{v} \times H \right) \frac{\partial f_i}{\partial v} = y_i - \nu_i (f_i - f_0), \end{cases} \quad (16)$$

where  $y_{e,i}$  are random forces and  $\nu_i$  make allowance for collisions of particles. We will solve system (16) jointly with the Poisson equation:

$$\operatorname{div} E = -4\pi e \left\{ \int f_e d\mathbf{v} - \int f_i d\mathbf{v} \right\}. \quad (17)$$

Normalizing the random forces

$$\langle y_\alpha(\mathbf{r}, \mathbf{v}, t), y_\alpha(\mathbf{r}', \mathbf{v}', t') \rangle = 2\nu_\alpha \delta_{\alpha\alpha} f_{0\alpha}(\mathbf{v}') \delta(\mathbf{v} - \mathbf{v}') \delta(\mathbf{r} - \mathbf{r}') \delta(t - t'),$$

from system (16) and (17) we get an expression for the correlator of the longitudinal electric field

$$\begin{aligned} \langle E^2 \rangle_{k\omega} &= \frac{8\pi^2 e}{|\operatorname{Re} \epsilon_e(\omega, k)| k^2} \delta[\operatorname{Re} \epsilon_e(\omega, k)] \sum_k \sum_n \int_0^\infty v_\perp dv_\perp \times \\ &\times \int_{-\infty}^\infty dv_\parallel f_{0\alpha}(v_\parallel v_\perp) I_n^2 \left( \frac{v_\parallel v_\perp}{\omega_{H\alpha}} \right) \delta(\omega - k_\parallel v_\parallel - n\omega_{H\alpha}), \end{aligned} \quad (18)$$

where  $\epsilon_e$  is the longitudinal component of the dielectric constant of the plasma. For weak magnetic fields when  $k_\perp s_e \ll \omega_{He}$ ,  $k_\perp s_i \gg \omega_{Hi}$ , the correlator  $\langle E^2 \rangle_{k\omega}$  is of the form:

$$\langle E^2 \rangle_{k\omega} = 4\pi^2 T_{\Phi\Phi} \frac{k^2 a_e^2}{1 + k^2 a_e^2} [\delta(\omega - \omega_s) + \delta(\omega + \omega_s)], \quad (19)$$

where

$$T_{\Phi\Phi} = \frac{T_e}{\left| 1 - \frac{e^2 E_0^2 k_0}{2m^2 \omega_0} \cos \alpha \sqrt{1 + k^2 a_e^2} \right| \left| \omega_0 \pm \omega_{Hi} \right|^2 v_s}.$$

For some magnetic field ( $k_\perp s_{e,i} \ll \omega_{He,i}$ ), assuming that  $ks_i \ll \omega \ll ks_e$ , from (19) we get:

$$\langle E^2 \rangle_{k\omega} = 8\pi^2 \frac{T_{\Phi\Phi}}{\omega} \frac{k^2 a_e^2}{1 + k^2 a_e^2} \frac{|\omega^2 - \omega_{Hi}^2|}{\omega_1^2 - \omega_2^2} [\delta(\omega^2 - \omega_1^2) + \delta(\omega^2 + \omega_2^2)]. \quad (20)$$

Here  $\omega_{1,2}$  is determined by Eq. (14).

Let us examine the interaction of charged particles with fluctuational fields induced in the solar atmosphere. The equation describing the change in particle energy due to interaction with electric fluctuation fields is of the form [9]:

$$\frac{d\varepsilon}{dt} = \frac{1}{\rho^2} \frac{d}{d\rho} \rho^2 D(\rho) \frac{d\varepsilon}{d\rho}, \quad (21)$$

where

$$D(\rho) = \frac{q^2}{8\pi(\pi v)^2} \int \frac{\omega^2}{k^2} \langle E^2 \rangle_{k,\omega} dk.$$

Here  $q$  is the charge on the particle.

Let us assume that the longitudinal waves are propagated along the magnetic field. Then substituting (20) into (21), after integrating in  $k$  we get:

$$\frac{d\varepsilon}{dt} = \beta \varepsilon^{-1/2}, \quad (22)$$

where

$$\beta = \frac{4\pi}{9} \frac{1}{2} \frac{e^4 E_0^2 n_e}{m_i n_e^2 [T_i \omega_0 (\omega_i \pm \omega_H)]^2}.$$

When charged particles are in motion in the solar atmosphere, their energy decreases due to the ionization losses:

$$\frac{d\varepsilon}{dt} = \frac{\sqrt{m_e} e^2 \omega_{ie}^2}{2\varepsilon^{1/2}} \ln \frac{\varepsilon}{\hbar \omega_{ie}}, \quad \omega_{ie}^2 = \frac{4\pi e^2 n_0}{m_e}. \quad (23)$$

From Eqs. (22) and (23) let us estimate the mean energy to which particles are accelerated under the action of this mechanism:

$$\varepsilon_{sp} = \frac{1}{27} \frac{1}{m_i^3 T_i^2} \cdot \left( \frac{e E_0}{\omega_0} \right)^6. \quad (24)$$

From (23) and (24) it follows that owing to the inverse dependence of the rate of acceleration by fluctuational fields on energy, its critical value  $\varepsilon_c$  corresponds to the maximum energy to which the particles are accelerated. This is accounted for by the fact that for particles with energy  $\varepsilon > \varepsilon_{cr}$  the forces of deceleration begin to dominate over the forces of acceleration and their energy decreases down to the value  $\varepsilon_{cr}$ ; but if  $\varepsilon < \varepsilon_{cr}$ , acceleration predominates over deceleration and the particle enters the energy range  $\varepsilon \sim \varepsilon_{cr}$ .

Specifying the parameters of the solar plasma in the region of chromospheric flares  $n = 10^9 \text{ cm}^{-3}$ ,  $T_i = 10^6 \text{ K}$ , and setting



---

$\omega_0 - 2\pi f_0 = 10^7 \text{ sec}^{-1}$ ,  $E_0 = 10^2$  units CGSE, which corresponds to radio emission of type III, we get  $\epsilon_{cr} = 10^2 - 10^3$  Mev for protons. The proposed method of acceleration of solar cosmic rays in a field of strong electromagnetic radiation evidently can provide the energy sufficient to account for several cases of short-term and long-term increases in streams of heavy particles recorded by the L. V. Kurnosova group (Physics Institute imeni P. A. Labedev of the USSR Academy of Sciences) in experiments on the Elektron series satellites.

# REFERENCES

1. Smit, G., and Smit, E., Solnechnyye vspyshki (Solar Flares), "Mir", 1966.
2. Syrovatskiy, S. I., Astron. zhurn., 43, 340 (1966).
3. Davydovskiy, V. Ya., and Yakushev, Ye. M., ZhETF, 52, 1068 (1967).
4. Vekshteyn, G. A., Ryutov, D. D., and Sagdeyev, R. Z., Doklad na seminare: Generatsiya kosmicheskikh luchey na Solntse (Paper at the Seminar: Generation of Cosmic Rays at the Sun), Leningrad, 1970.
5. Timofeyev, A. V., and Pistunovich, V. N., in the book: Voprosy teorii plasmy (Problems of Plasma Theory), No. 5, Atomizdat, 1967.
6. Jukes, J., J. Fluid Mech., No. 3, 275 (1957).
7. Nezlin, M. V., and Solntsev, A. M., ZhETF, 45, 840 (1968).
8. Zavoytskiy, Ye. K. et al., ZhETF, 46, 511 (1964).
9. Kats, M. Ye., and Yukhimuk, A. K., UFZh, 14, 1019 (1969).
10. Sitenko, A. G., Elektromagnitnyye fluktuatsii v plazme (Electromagnetic Fluctuations in Plasma), Khar'kov State University Press, 1965.

14741.5.0000

EFFECT OF SMALL FLARES IN THE  
NEUTRAL COMPONENT OF SECONDARY COSMIC RADIATION

/50

V. I. Bondarenko, L. V. Raychenko,  
A. K. Yukhimuk

The effect of small class 2 and higher chromospheric flares has been analyzed in a number of studies [1-4]. Here it is assumed that flares of classes 1 and 1+ are not accompanied by an appreciable effect in secondary component of cosmic radiation. Nonetheless, beyond the limits of the magnetosphere some of these flares are accompanied by short-lived and long-lived increases in streams of heavy nuclei [5-6]. This provides grounds for assuming that in small scale division 1 flares generation of solar cosmic rays also occurs and that these flares must contribute to the secondary component of cosmic radiation. This article analyzes this effect, from the data of neutron supermonitors at the Kiev, Bukhta Tiksi, and Deep Rivers stations.

1. Effect of Small Flares From the Data of One Station (Kiev)

In the analysis, the flares 1f, 1n, 1b, and several flares of classes 2f, 2n, and 2b, respectively, from the adopted international 5-scale division classification of flare intensity were selected. Here, of the 1 flares generally those accompanied by the manifestation of bright points were selected.

In accordance with these criteria, 250 flares were selected for January - December 1970. The data of the neutron supermonitor in Kiev were analyzed for this period by the epoch superimposition technique, where the time of flare commencement was taken as the zero instants. The effect of selected flares was detected in the component of cosmic rays, amounting to 0.20-0.07 percent. Figs. 1 and 2 present the results of the statistical analysis of the effect of small flares in the neutron component of cosmic rays, from the data of stations at Climax [2] and Kiev, respectively. Striking is the slower decline in intensity in Fig. 2 compared with the data in [2]. This fact can be accounted for by one of the following causes:

/51

1) in the analysis of the data from the neutron supermonitor of the Kiev station, the amplitude of the solar-day variation was not excluded, based on the data of days preceding the flares;

2) since scale division 1 flares in several cases quite frequently follow one after the other, some blurring of the effect of increase and decline in the intensity of the neutron component of the cosmic rays from these flares is possible; and

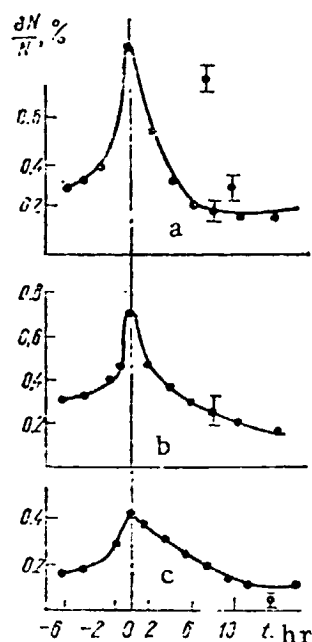


Fig. 1. Effect of small flares of scale division 2 and higher, from the data of the Climax station [2]:

- a. amplitude of solar-day variation was excluded, based on the data for the day proceeding the flare
- b. the mean-monthly diurnal variation was excluded
- c. the amplitude of the solar-daily variation was not excluded

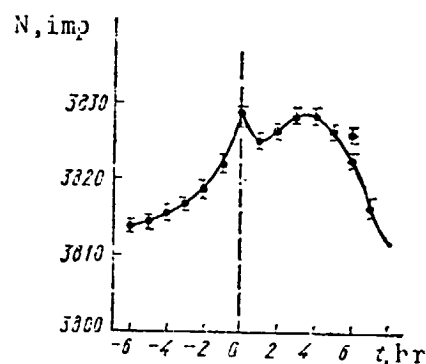


Fig. 2. Effect of flares of scale divisions 1 and 1+, based on the data of the neutron supermonitor at the Kiev station for 1970, without excluding the amplitude of the solar-day variation

3) the slow decline in the intensity of neutron component is accounted for by the conditions of propagation in the interplanetary medium of solar cosmic rays from small chromospheric flares.

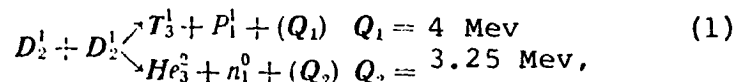
In Fig. 2 we can see that the curve describing the time variation of the neutron component intensity has two maxima: the first -- in the time interval corresponding to the commencement of the chromospheric flare, and the second -- in approximately three hours after the commencement of the chromospheric flare. Accordingly, it appears to us that the mechanism of the departure of particles from the region of acceleration at the Sun is possibly made up of two stages: at the first stage the particles of solar cosmic rays leave the acceleration region owing to the mechanism of collective exiting from the magnetic trap; the second stage

includes the diffusion of low-energy particles through the walls of the magnetic trap in those cases when tunnel conditions of existing are not realized.

## 2. Exiting of Particles Generated in Small Flares due to the Diffusion Across the Magnetic Field of the Trap

As shown by numerous investigations of magnetic fields in active groups of sunspots, chromospheric flares originate in the neutral points of the magnetic field if the field gradient in the vicinity of the point is quite strong. During the flare period, annihilation of magnetic fields occurs: here the plasma is significantly heated in the flare region.

As we know, the temperature in the region of the flares is quite high, and as a result there is the probability that the following thermonuclear reactions occur:



where  $Q_1$  and  $Q_2$  are the amounts of energy released in the corresponding reactions. Thus, for the density  $n \sim 10^{15} \text{ cm}^{-3}$ ,  $n \sim 10^5 \text{ n}$ , and the temperature  $T \sim 10 \text{ kev}$ , the reaction intensity is  $10^4 \text{ cm}^{-3} \text{ sec}^{-1}$ .

The presence of products of thermonuclear reactions in the system can lead to plasma instability, which in turn causes the diffusion of particles across the magnetic field [7, 8]. These instabilities build up when the density of the reaction products exceeds some critical value.

Let us examine oscillations of the plasma in the flare region. To do this, let us use the model in which the magnetic field  $\vec{H} = (0, 0, H)$ , and let us orient the x axis along the inhomogeneity. Here we assume that the thermodynamic nonuniformity of the reacting ions is associated with the presence of density inhomogeneity. Then the distribution function of the products of the thermonuclear reactions is of the form [7]:

$$f_\alpha(v) = n_\alpha(x) \frac{\sqrt{\frac{m_\alpha}{\pi T}}}{4.7u_\alpha} \left( 1 + \frac{k_0 u_\alpha}{\omega_\alpha} \right) \frac{1}{v} \left[ e^{-\frac{m_\alpha}{T} (v - u_\alpha)^2} - e^{-\frac{m_\alpha}{T} (v + u_\alpha)^2} \right], \quad (2)$$

$$u_\alpha = \sqrt{\frac{2m_\alpha - m_d}{m_\alpha m_d}} Q;$$

$Q$  is the amount of energy released in the thermonuclear reaction,  $k_0 = \frac{1}{n_\alpha} \frac{dn_\alpha}{dx}$ ,  $\omega_\alpha$  is the cyclotron frequency of the reaction products,  $T$  is the temperature of the reacting ions,  $m_d$  and  $m_\alpha$  are

the masses of the deuterium ions and the reaction products, respectively.

Let us consider the longitudinal high-frequency oscillations of plasma in which  $\omega \gg kv_i, kv_e; \Omega_e \gg \omega_i; kr_H \gg 1$ ; ( $v_i$  and  $v_e$  are the ionic and electron thermal velocities, respectively;  $\Omega$  and  $\omega_e$  are the plasma and cyclotron frequencies of the electrons, and  $r_H$  is the Larmor particle radius). Under these conditions we can write the following dispersion equation:

$$1 - \left(\frac{\Omega_e}{\omega}\right)^2 + \sum_{e,i} 2i \sqrt{\pi} \frac{\Omega_e^2}{\omega^2} z e^{-z^2} + \sum_{\alpha} \frac{2\Omega_\alpha^2}{k^2 u_\alpha^2} \left[ u_\alpha(0) + F\left(\frac{\omega}{ku_\alpha}\right) \right] = 0, \quad (3)$$

where

$$F(y) = \int_0^\infty d\omega \frac{\frac{\partial \psi}{\partial \omega} + \frac{\omega_\alpha^*}{2\omega} \psi}{\sqrt{1 + \frac{\omega}{y^2}}}; \quad z = \frac{\omega}{\sqrt{2} kv_1}. \quad (4)$$

Here  $\psi_\alpha(\omega_\alpha)$  is the distribution function of the products of thermonuclear reactions, normalized for unity, over the transverse

energies  $W_\alpha = \frac{v_\perp^2}{u_\alpha^2}$ ,  $u_\alpha$  is the velocity, and  $\omega_\alpha^* = \frac{k_y k_y u_\alpha^2}{\omega_\alpha}$  is the

drift frequency of particles of species  $\alpha$  forming in the quasithermonuclear reactions. In the expression under the sign of the integral (4), the required branch of the root must be selected according to [8]. In Eq. (3), since the terms relating to ions have been omitted, the real part of the terms of the dispersion equation associated with the products of quasithermonuclear reactions can be neglected. Then it is not difficult to obtain the solution to Eq. (3), by representing  $\omega$  in the form of

$$\omega = \omega_0 + i\gamma, \quad \gamma \ll \omega_0;$$

$$\omega_0 = \Omega_e; \quad (5)$$

$$\frac{\gamma}{\omega_0} = - \sum_{e,i} \sqrt{\pi} z^2 \frac{\Omega_e^2}{\omega_0^2} e^{-z^2} - \sum_{\alpha} \left( \frac{\Omega_\alpha}{ku_\alpha} \right)^2 \text{Im} F\left(\frac{\omega}{ku_\alpha}\right). \quad (6)$$

In this expression, the first term corresponds to the Landau damping by electrons and ions, and the second is associated with the products of quasithermonuclear reactions, and by virtue of these specific nature of the distribution function of the products of quasithermonuclear reactions, this second term can lead to instability. Instability specifically develops when  $\text{Im} F < 0$  and when Landau damping is small.

Using (5), let us find that  $\text{Im} F < 0$  in the region  $\frac{\omega}{ku_\alpha} < 1$  when  $k_y < 0$  and is equal to:

$$\text{Im} F\left(\frac{\omega}{ku_\alpha}\right) \approx -\frac{\pi}{2} \frac{\omega^2}{ku_\alpha}. \quad (7)$$

The final expression for the increment of oscillations is of the following form:

$$\gamma = -\Omega_e \sum_{\alpha} \sqrt{\pi} z_e^{-2} + \frac{\pi}{2} \Omega_e \sum_{\alpha} \frac{\Omega_p^2 n_{\alpha}}{(k u_{\alpha})^2}. \quad (8)$$

From (8) we see that  $\gamma = \gamma_{\max}$  when  $\omega \sim k u_{\alpha}$ . In this region, the number of particles of species  $\alpha$  effectively interacting with the wave is large. Therefore the diffusion of products of thermonuclear reactions across the magnetic field becomes appreciable. Note that this analysis is valid, strictly speaking when  $\gamma > \omega_z$ , which imposes a constraint on the concentration of the products of quasithermonuclear reactions at which instability will be initiated.

Using as the possible flare parameters  $n_0 \sim 10^{14} \text{ cm}^{-3}$ ,  $T_i \sim 10 \text{ kev}$ ,  $T_e \sim 10 \text{ ev}$ ,  $k_0 \sim 10^{-6} \text{ cm}^{-1}$ , and  $H \sim 10 \text{ gauss}$ , we get the instability threshold  $\sim 10^{-4}$ , which can be attained in a time period of the order of  $\tau \sim 10^3 \text{ sec}$ . At this stage of flare buildup, the diffusion of reaction products across the magnetic field becomes appreciable, that is, the generation of cosmic rays due to the instability under consideration.

153

From qualitative considerations of the theory of turbulence it follows that the coefficient of diffusion for a high-temperature plasma can be estimated according to the formula:

$$D_{\alpha} \sim \gamma_{\alpha}^2. \quad (9)$$

Then the total flux of particles exiting from this region is

$$P_{\alpha} \sim \pi r n_{\alpha} D_{\alpha}, \quad (10)$$

where  $r \sim 1/k_0$  is the size of the region. For the flare parameters we have been considering,  $P_{\alpha} \sim 10^{30}$ ; the total flux of exiting particles for a flare duration  $t \sim 10^3 \text{ sec}$  is  $\sim 10^{32}$  particles.

### 3. Analysis of the Effect of Small Flares From the Data of Three Stations (Kiev, Bukhta Tiksi, and Deep River)

It was of interest to investigate the effect of small flares of scale division 1 and 1+, cancelling out the solar-day variation, whose amplitude is  $\sim 0.3$  percent at the middle latitudes.

If we assume that the solar-day variation is due to the anisotropy of cosmic radiation, and invariant, at least for 24 hours, and that this anisotropy is an arbitrary function of  $\phi$ ,  $t$  (where  $\phi$  is the longitude of the station reckoned from the midnight

meridian and  $t$  is time), then it can be shown [9] that the summation of the data from three stations separated from each other by  $120^\circ$  in longitude excludes the anisotropy component of the solar-day variation.

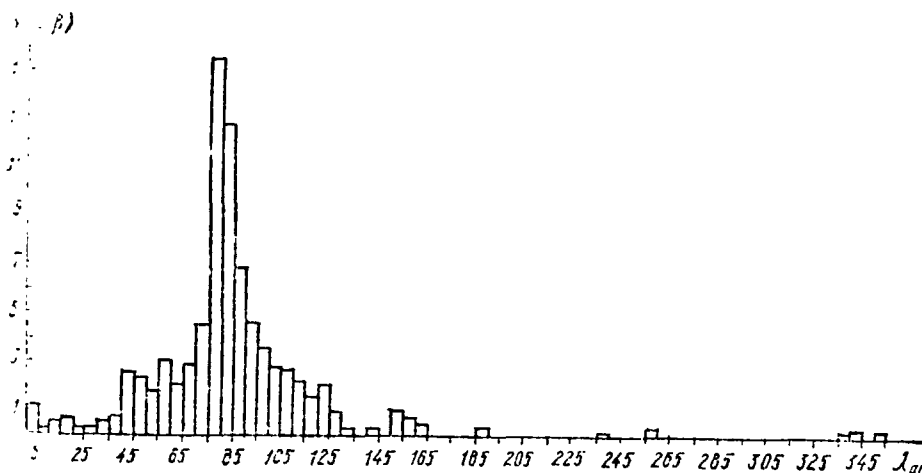


Fig. 3. Reception cones for the Moscow station

In this section, results of interpreting 24 cases of small flares of scale divisions 1 and  $1^+$  in January - February 1970 are presented, from the data of three stations (Kiev, Bukta Tiksi, and Deep River), separated by approximately  $120^\circ$  in longitude.

In selecting the stations whose data were analyzed by the superposition of epoch technique, the following criteria were used: closely similar values of cutoff sharpness; similar asymptotic longitudes; and latitudinally similar reception cones.

Reception cones for each station (Figs. 3-5) were plotted from tabulated variational coefficients [10], determining the anisotropic component of cosmic radiation arriving from asymptotic directions in the solid angle  $\Omega_i$ : /54

$$v(\Omega_i, \beta) = \int W(R) R^\beta \frac{Y(\Omega_i, R)}{Y(4\pi, R)} dR, \quad (11)$$

where  $W(R)$  are the coupling coefficients for the [cutoff] sharpness values  $R$  in the interval from 0 to 500 bv;  $\beta$  is the index of the cosmic rays spectrum in the range  $-1.5 \lesssim \beta \lesssim 0.6$ ;  $Y(-\Omega_i, R)$  is the integral of the function  $Z(\theta, \phi)$  over all zenithal and azimuthal angles  $\theta$  and  $\phi$ , respectively. The reduced reception cones are plotted for the spectral index  $\beta = 0.0$ ; it is also



assumed that in view of the close location, the calculations of the variational coefficients for the Moscow station are valid for the characteristics of the Kiev station reception cone.

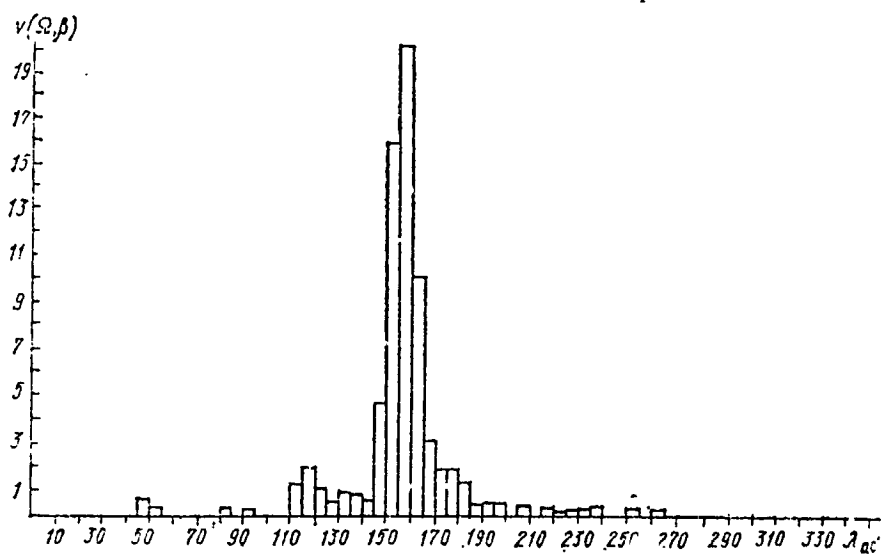


Fig. 4. Reception cones for the Bukhta Tiksi station

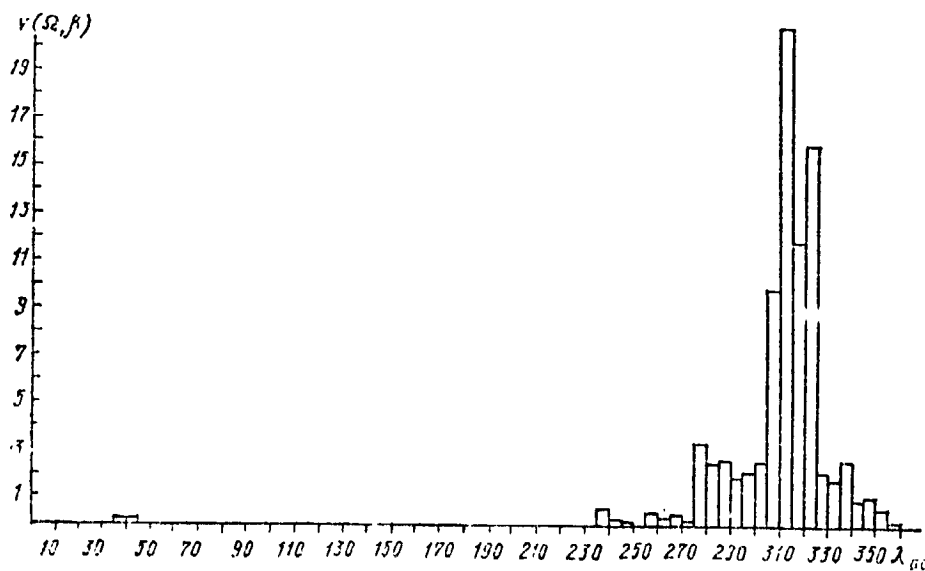


Fig. 5. Reception cones for the Deep River station

Fig. 6 presents a curve illustrating the nature of the effect of small scale division 1 and 1<sup>+</sup> flares when the anisotropic component of the solar-day variation is excluded by the method described. As we can see from the figure, the effect of the flares analyzed is  $0.45 \pm 0.3$  percent. The nature of the decline in the intensity differs from the one shown in Fig. 2, so that it can be assumed that its slow decline in this case is due to the effect of the solar-day variation. Nonetheless, the presence of the second maximum in Fig. 6 confirms the assumption that a diffusional mechanism of the exiting of accelerated particles in small chromospheric flares from the region of acceleration occurs several hours after a flare, as is presented in section 2 of this article.

In conclusion, the authors express their gratitude to Candidates of Physicomathematical Sciences O. I. Inozemtseva (Institute of Terrestrial Magnetism, the Ionosphere, and radio wave propagation of the USSR Academy of Sciences), for discussing the study and for valuable comments.

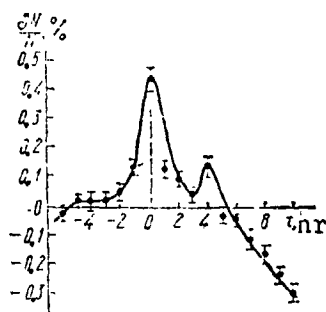


Fig. 6. Effect of scale division 1 and 1<sup>+</sup> flares (January - March 1970), with the anisotropic component of the solar-day variation cancelled out by the three-station method.

#### REFERENCES

1. Dorman, L. I., Variatsii kosmicheskikh luchey i issledovaniya Kosmos (Variations of Cosmic Rays and Space Studies), USSR Academy of Sciences Press, Moscow, 1963.
2. Kolomeyets, Ye. V., Geomagnetizm i aeronomiya, 1(4), (1961).
3. Dorman, L. I., and Kolomeyets, Ye. V., ibid, 1(5), (1961).
4. Dorman, L. I., Ivanov, V. I., and Kolomeyets, Ye. V., Geomagnetizm i aeronomiya, 4(3), (1964).
5. Karnsova, L. V. et al., Kosmicheskiye issledovaniya, 5, (1967).
6. Suslov, A. A., and Tinde, I. P., ibid, 5(4), (1967).
7. Post, R., UFN, 61(4), (1957).
8. Kolesnichenko, N. N., and Srayevskiy, V. N., Atomnaya energiya, No. 5, (1967).
9. Pankratov, A. K., "Relationship Between Diurnal Variation of Cosmic Rays With the Structure of the Interplanetary Medium," Avtoreferat. Dis. (Author's Abstract of Dissertation), Moscow State University Press, 1970.
10. McCracken, K. C., Rao, U. R., and Fowler, B. C., Cosmic Ray Tables, SASY Instruction Manual, No. 10, London, 1965.

N74-28110

ANALYSIS OF THE NATURE OF EXCESSIVE COSMIC  
RADIATION IN THE AREA OF THE BRAZILIAN  
MAGNETIC ANOMALY AT ALTITUDES 250-500 KM,  
FROM KOSMOS-225 SATELLITE DATA

/55

L. V. Raychenko

The existence of the gigantic anomaly in the intensity of cosmic radiation at the altitudes 190-340 km was first detected with the second and third Soviet spacecraft-satellites [1-3]. In these experiments, a telescope of gas-discharge counters recorded protons with energies exceeding 60 Mev, and electrons with energies stronger than 8 Mev. The second spacecraft-satellite orbited at altitudes of 306-339 km, and the third -- at altitudes of 187-265 km. The flux of particles recorded by the telescope at all points at which measurements were made exceeded the cosmic ray flux in the region of the equator, the mean flux was 1.2 particles  $\text{cm}^{-2} \cdot \text{sec}^{-1} \cdot \text{ster}$ , and in the upper latitudes -- 3.3 particles  $\text{cm}^{-2} \cdot \text{sec}^{-1} \cdot \text{ster}$ .

The following results were also obtained for the first time in these experiments.

1. There is a local anomaly in the cosmic radiation intensity over the southern part of the Atlantic (in the region between South America and the southern tip of Africa) (Fig. 1). In the region of this anomaly (called the South Atlantic Anomaly), the counting rate of the telescope during the flight of the second spacecraft-satellite rose by roughly 70 times compared with the counting rate in adjoining regions. /56

2. A very stable local anomaly in the intensity of cosmic radiation was detected, located along the coasts of Antarctica (called the South Anomaly). In this region, the telescope counting rate during both flights was approximately two orders of magnitude greater than the counting rate in adjoining regions.

3. The recorded intensity of radiation at the altitudes 190-340 km exceeded by several times the intensity of cosmic rays over the entire surface of the Earth within the latitudes  $-65$  to  $+65^\circ$ . Also detected was an interesting difference between the patterns of the distribution in cosmic ray intensities over the surface of the Earth obtained during both flights -- the absence of the well-defined anomaly in the region of the South Atlantic during the flight of the third spacecraft-satellite, while during the flight of the second spacecraft-satellite the South Atlantic anomaly was detected. It is highly probable that this difference

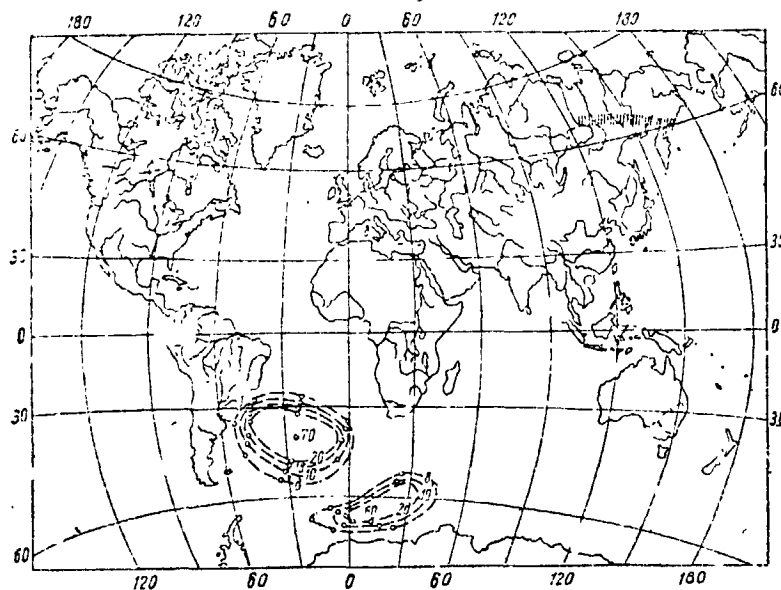


Fig. 1. Projection on the surface of the earth of the regions of the Southern and South Atlantic anomalies from measurements on the second and third Soviet spacecraft-satellites

is associated with the difference of the altitudes at which the flights of both satellites were made, about 100 km. Thus, the boundary of the South Atlantic Anomaly in altitude was determined. It must, however, be noted that the results obtained in the experiments on the second and third spacecraft-satellites do not have adequate statistical precision owing to the gravity of the flights (both flights lasted one day). Thus, the rise in the intensity in the region of the South Atlantic Anomaly was recorded only on three successive orbits of the satellite trajectory lying between Africa and South America.

157

More detailed and longer investigations of the spatial structure and nature of the excessive cosmic radiation in the area of the South Atlantic Anomaly were conducted in an experiment on the Kosmos-225 satellite (14-29 June 1963, orbital inclination  $49^\circ$ , and altitudes 250-550 km). Since the flight of the satellite occurred at latitudes below  $50^\circ$  N. Lat, it was not possible in this experiment to investigate the region of the Southern Anomaly, since the increase in the counting rate of the telescope at latitudes close to the Southern Anomaly was practically indistinguishable from the latitudinal trend of the excessive background of cosmic radiation [4].

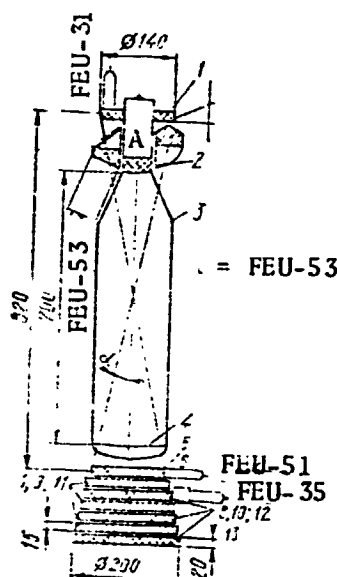


Fig. 2. Device for recording electron component of cosmic radiation in the experiment on the Kosmos-225 satellite:

1. scintillating counter (telescope)
2. Cherenkov counter (Plexiglas)
3. gas Cherenkov counter
4. spherical mirror ( $f = 700$ )
5. scintillating counter (telescope)
- 6, 8, 10, 12. scintillating counters (measuring)
- 7, 9, 11. lead

axis. The energy threshold of the GCC counter was 6.2 Mev for electrons and 11.5 Mev for protons.

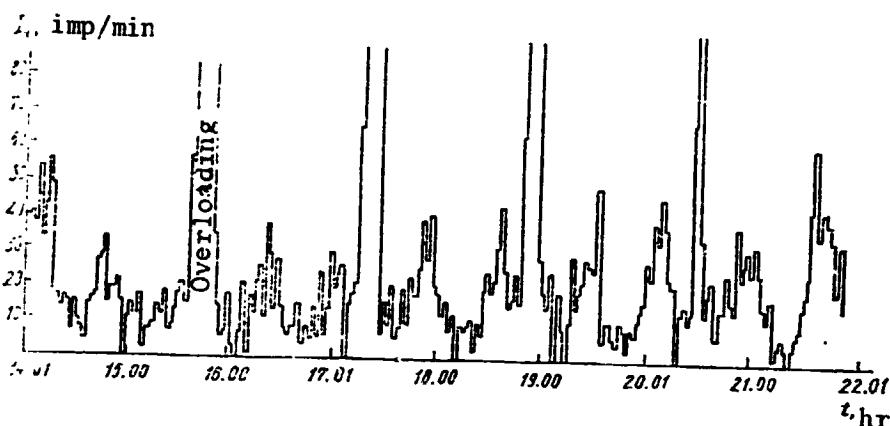


Fig. 3. Latitudinal trend of nuclear component of cosmic radiation in one of the sections of the Kosmos-225 satellite trajectory

The device for recording the flux of electrons in the energy range  $\sim 300$  Mev launched on board the Kosmos-225 satellite consisted of a control telescope discriminating the direction of the incident particles and the measuring section for recording the avalanches formed by electrons striking the installation (Fig. 2). The control telescope with aperture  $\Gamma = 1.8$  cm<sup>2</sup>.ster consisted of two scintillators and a gas Cherenkov counter connected to a triple-coincidence circuit. The telescope was removed outside the outer hull of the satellite.

The total material in the telescope was about 20 g/cm<sup>2</sup>, therefore the minimum electron energy recorded by the telescope was  $\sim 40$  Mev. The gas Cherenkov counter (GCC) did not record the direction of the incoming particles, since the light generated in the counter material upon passage of a particle along its axis, regardless of the direction, impinged on the multiplier photocathode. However, a light pulse sufficient to record the magnitude was induced only if the particle passed close to the counter

A solid-state Cherenkov counter (SCC) was used to record the direction of particle arrival.

In order to record the total flux of particles over a wider energy range, an additional output was provided in the device, for recording the counting rate of triple coincidences in two control scintillators and a third Cherenkov counter (control telescope). The aperture of the oriented telescope was  $\Gamma = 1.8 \text{ cm}^2 \cdot \text{ster}$ , just as in the telescope of the gas-discharge Cherenkov counter. If in events of accompanying the triggering of the GCC either electrons with energy  $E \sim 40 \text{ Mev}$ , or protons with energy  $E_p \geq 11.5 \text{ Mev}$  (GCC threshold) could be recorded, events accompanied by the triggering of the orient telescope with the SCC could be caused either by electrons in this same energy range or by protons with  $E_p \geq 600 \text{ Mev}$  (the effective threshold energy of the SCC).

158

Using the oriented telescope with the SCC on the Kosmos-225 satellite, several interesting results were obtained, concerning the radiation environment at the altitude 250-550 km. The counting rate of this channel in the equatorial region was  $9.7 \pm 0.3 \text{ min}^{-1}$ , which corresponded to a flux of  $900 \pm 30 \text{ particles m}^2 \cdot \text{sec}^{-1} \cdot \text{ster}^{-1}$ . Thus, whereas on the basis of [5] it can be assumed that the flux of protons in the equatorial region is approximately  $200 \text{ particles m}^2 \cdot \text{sec}^{-1} \cdot \text{ster}^{-1}$ , the flux recorded by the telescope with the SCC exceeded the value by a factor of 4.5. This indicates the presence in the altitude interval 250-550 km of an additional radiation background that exceeds by several times the flux of primary cosmic rays. Thus, these results confirm the conclusion in [6] that at these altitudes there is an additional radiation background that is several times greater than the cosmic ray flux.

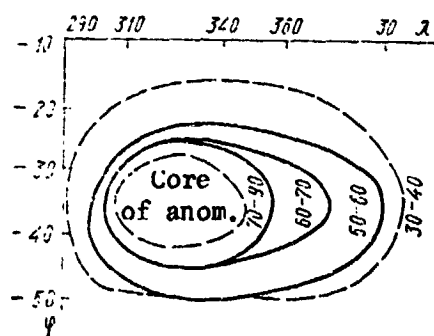


Fig. 4. "Core" and isolines of equal counting rates of the South Atlantic Anomaly for the intensity of radiation at the altitudes 250-400 km.

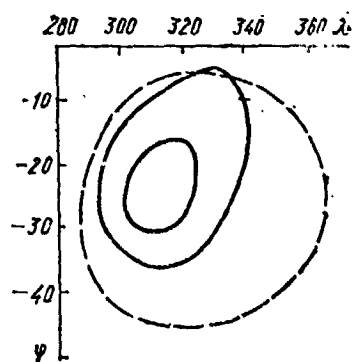


Fig. 5. Region of the South Atlantic Anomaly of intensity at the altitudes 400-550 km (dashed line) and isolines of the total vector of the geomagnetic field at the corresponding altitude (solid lines)

The counting rate measured by the oriented telescope has a latitudinal dependence. Fig. 3 shows the latitudinal trend of the counting rate measured with this channel for one of the sections of the flight trajectory. In the region of the latitude  $49^\circ$ , the counting rate was 20-25 counts per minute, which corresponds to a flux of 1800-2300 particles  $\text{m}^{-2} \cdot \text{sec}^{-1} \cdot \text{ster}^{-1}$ . The observed background, evidently, is accounted for by electrons with energies  $E \geq 40$  Mev, since the minimum energy of protons required to trigger the SCC is  $\sim 600$  Mev.

Now let us turn to the results of investigating the spatial structure of the South Atlantic Anomaly in the intensity of cosmic radiation obtained in the experiment on the Kosmos-225 satellite. When the data from the instruments for recording the electronic and nuclear component of cosmic radiation over several sections of the satellite trajectory were interpreted, the counting rate of the recorded particles was found to increase by several orders compared with the counting rate over the adjoining sections of the trajectory (Fig. 3). This suggested that over these sections the satellite trajectory passed over the region of the South Atlantic Anomaly discovered in the experiments on the second spacecraft-satellite. The data of the control telescope over the sections of the trajectory with the anomalously high counting rate were interpreted, which made it possible to obtain information on the spatial structure and the altitude trend of the South Atlantic Anomaly (Figs. 4 and 5). The first approximation, the line of equal intensity with the count number  $N \geq 100$  counts (cycles) in a 2-minute interrogation cycle was taken as the boundary of the anomaly. Since the geometric factor of the control telescope  $\Gamma = 1.8 \text{ cm}^2 \cdot \text{ster}$ , the line of equal intensity  $I = 0.45 \text{ sec}^{-1} \cdot \text{cm}^{-2} \cdot \text{ster}^{-1}$  was adopted as the anomaly boundary. As Fig. 4 shows, at the altitudes 250-400 km of the region of the South Atlantic Anomaly, not only was it possible to distinguish the "core" of the anomaly (the region in which the counting rate of the control telescope was several orders of magnitude greater than the intensity of cosmic rays at these latitudes), but also to trace the isolines of equal counting rate encompassing the anomaly "core". When Figs. 2 and 4 are compared, we can see (Fig. 6) that the longitudinal extent of the South Atlantic Anomaly in the intensity of radiation, from the data of the Kosmos-225 satellite, increased compared with the results of the second spacecraft-satellite. Additionally, evidently there was a change in the orientation of the anomaly "core" position for the 1968 epoch compared with the 1960 epoch. These phenomena are naturally associated with the change in solar activity: the measurements on Kosmos-225 were made during a period of high solar activity, while the measurements on the second spacecraft-satellite encompassed a period of minimum solar activity.

159



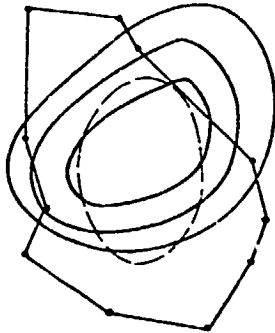


Fig. 6. Position of the South Atlantic Anomaly for the 1960 and 1968 epochs (solid and dashed lines, respectively). The points represent the intensities of the geomagnetic field at the corresponding altitudes.

The results from this experiment made it possible to trace the spatial structure of the South Atlantic Anomaly for the first time using the same instrument at different altitudes -- from 250 to 550 km. Fig. 5 shows that at the altitudes 400-550 km the anomaly in the intensity of cosmic radiation enlarges and forms a horn, narrowing with decrease in observational altitude. This result is extremely vital for clarifying the nature of the South Atlantic Anomaly, which we will discuss below.

The discovery and study of the South Atlantic Anomaly in the intensity of radiation provides extremely vital information on the structure of the Earth's magnetic fields. It proved possible to compare information on the spatial structure of the anomaly not only with ground data of the geomagnetic field, but also with the isolines of the total vector of the geomagnetic field at different altitudes <sup>/61</sup>

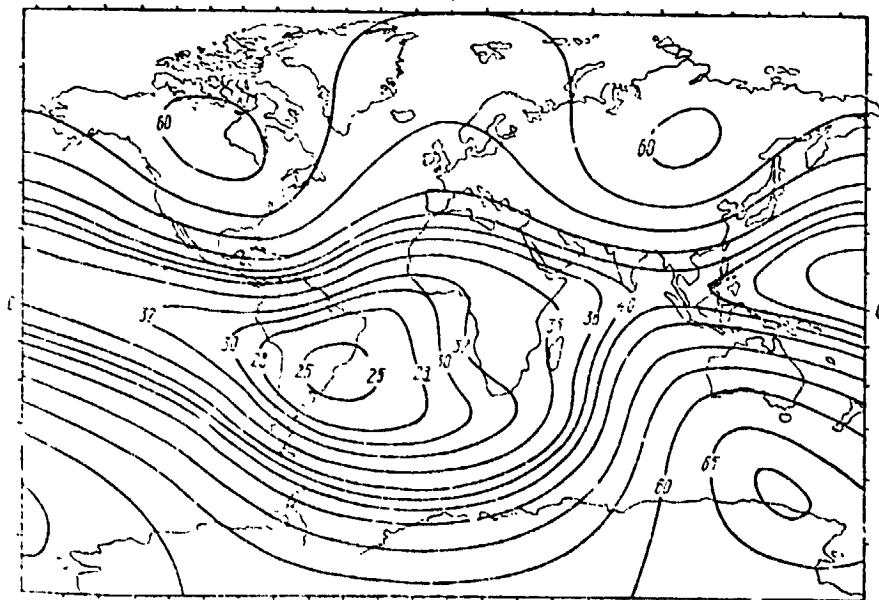


Fig. 7. Isolines of the total vector of the geomagnetic field at the altitude 0 km. The isolines of the constant B are in gauss

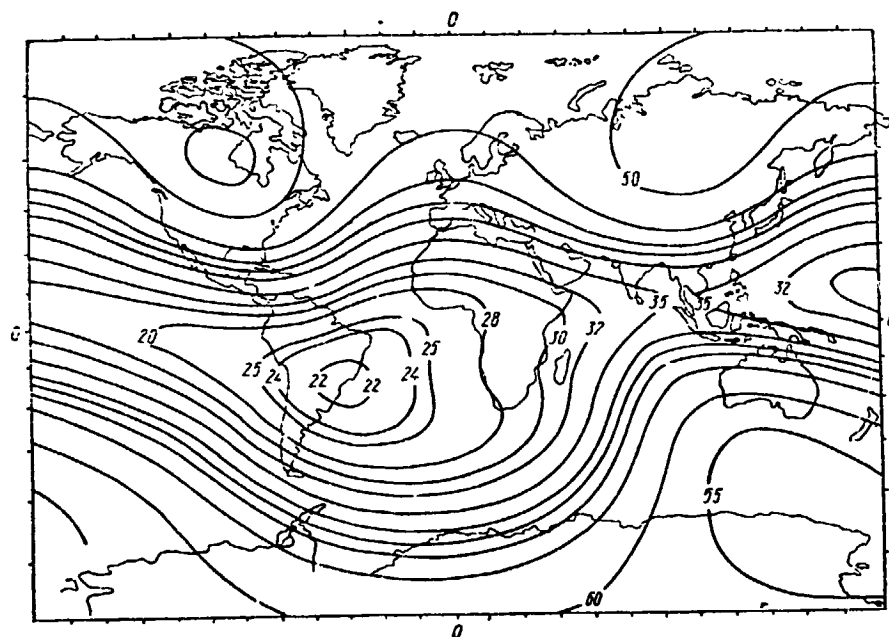


Fig. 8. Isolines of the total vector of the geomagnetic field at the altitude 300 km. The isolines of the constant B are in gauss

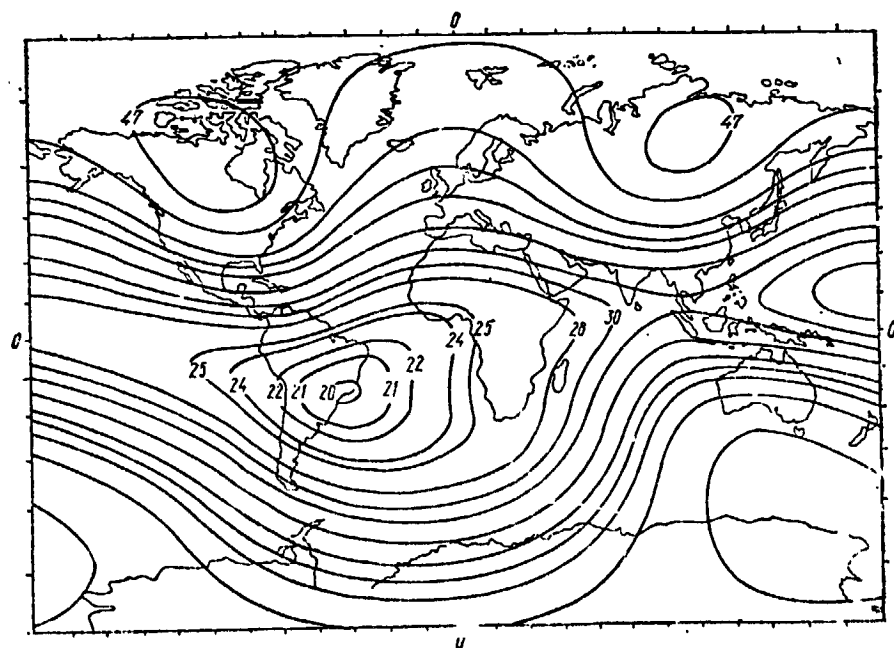


Fig. 9. Isolines of the total vector of the geomagnetic field at the altitude 500 km. The lines of the constant B are in gauss

(Figs. 7-9). Results of this comparison are in Fig. 7. From the data of the Kosmos-225 satellite, we can note the close proximity of the geomagnetic field minimum and the center of the South Atlantic Anomaly. These results indicate that the action of the regional magnetic anomaly on the Earth's surface extends all the way to altitudes of  $\sim 200-500$  km.

Now let us discuss several problems dealing with the nature of the South Atlantic Anomaly in the intensity of cosmic radiation. As shown in [5], due to particles forming the albedo of cosmic rays, one cannot explain the increase in the telescope counting rate in the region of anomalies, since even at the equator the experimental data and theoretical models permit the existence of an anomaly within the limits of not more than 50 percent of the intensity of cosmic rays, whose flux is only 200 particles  $m^{-2}.sec^{-1}.ster^{-1}$ . The results of the experiment on the Kosmos-225 satellite represent new convincing proof in favor of the assumption [1, 2] that the South Atlantic Anomaly in the intensity of radiation is associated with the internal radiation belt of the Earth.

A particle reflected by the Earth magnetic field travels along a magnetic force line to the magnetically-conjugate [magnetic-mirror] point and is reflected in the same magnitude of the magnetic field  $B_1$  until it is scattered in the geomagnetic field owing to a change in its pitch angle [7]. For the region of negative magnetic anomaly with magnetic field intensity  $B_1$ , the corresponding magnetically-conjugate region must be characterized by a greater magnitude of the overall magnetic field  $B_2$ . But the altitudes at which reflection from the magnetically conjugate points occurs are associated by the ratio [8]:

$$h_2 = (R_0 + h_1) \left( \frac{B_2}{B_1} \right)^{1/2} - R_0,$$

where  $R_0$  is the Earth's radius, and  $h_1$  is the mirror altitude of reflection above the region where the intensity of the magnetic field is  $B_1$ .

Thus, the negative anomaly of the magnetic field must cause, over the corresponding region, a decrease in the level at which reflection of charged particles occurs, so that the regions of the negative anomalies can be apparently regions of the "sink" of charged particles from the Earth's radiation belts. This conclusion is confirmed by the "horn-shaped" constriction with altitude of the "core" of the South Atlantic Anomaly in the intensity, recorded in experiments on the Kosmos-225 satellite.

In conclusion, the author expresses his deep gratitude to L. V. Kurnosova and L. A. Razorenov (Physics Institute of the USSR Academy of Sciences imeni Lebedev) for discussion of the study and for valuable comments.

#### REFERENCES

1. Ginzburg, V. L. et al., Geomagnetizm i aeronomiya, 2(2), 189 (1962).
2. Kurnosova, L. V. et al., Iskusstvennyye sputniki Zemli (Artificial Earth Satellites), No. 8, 1961, p. 90.
3. Savenko, I. A. et al., Geomagnetizm i aeronomiya, 1(4), 490 (1961).
4. Kurnosova, L. V. et al., K voprosu o prirode radiatsionnogo fona na vysotakh 250-550 km (Nature of Radiation Background at the Altitudes 250-500 km), Physics Institute im Lebedev of the USSR Academy of Sciences, 1969.
5. Kurnosova, L. V., Razorenov, L. I., and Fradkin, M. I., in the book: Iskusstvennyye sputniki Zemli, No. 6, 1961, p. 132.
6. Ginzburg, V. L. et al., Uspekhi fiz. nauk, ser. fiz., No. 12, 31 (1961).
7. Spitzer, L., Fizika polnost'yu ionizirovannogo gaza (Physics of Wholly Ionized Gases), Moscow, IL, 1965.
8. Dessler, A. J., J. Geophys. Res., 64(7), 713 (1959).

NT-70271

## INSTRUMENTS FOR MEASURING RADIANT THERMAL FLUXES

/62

O. A. Gerashenko and S. A. Sazhina

Measuring radiant energy and physical parameters characterizing its transport conditions is a vital problem in thermometry as applied to the investigation of space. Specific conditions of the operation of radiation detectors require combinations of simplicity and reliability of an instrument with the stability of measurement precision. In this respect, interest in detectors capable of carrying out absolute (unrelated to black body reference) measurements is understandable.

In the Laboratory of Techniques of Thermal Measurement of the ITTF [transliterated] of the Ukrainian SSR Academy of Sciences, an absolute two-sided radiometer has been developed, constructed on the principle of replacing the energy of absorbed radiation investigated with electric energy. The instrument is a thermoelectric converter. The classic prototype of this instrument is the two-element Angstrom thermoelectric radiometer. One of the elements is irradiated with the flux being measured, and the second -- the compensation elements -- is shaded and is heated with electric current. The equality of energies supplied to plates is monitored with a sensitive element -- a differential thermocouple, whose junctions lie at the irradiated and shaded plates [2]. In the instrument developed, the thermoelectric sensor performs the functions of the sensitive element and the auxiliary wall through which a considerable fraction of the absorbed or generated thermal energy streams. This makes it possible to conduct measurements on the principle not only of compensation, but also of the auxiliary wall. A schematic and layout is shown in Fig. 1. A series-built laminated transducer of thermal flux [1] serves as the auxiliary wall, containing about 5000 pairs of galvanic thermocouple junctions in a volume not exceeding 0.5 cm<sup>3</sup>. The thermoelectrodes of the pile are arranged in parallel, insulated, and secured to each other with epoxy resin. Thus, sensor 1 is a rigid intermediate wall, on whose parallel planes are situated the hot and cold junctions. Plates 2 made of aluminum are mounted on both sides of the transducer. They are coated with an insulation film obtained by anodic oxidation. Electric heaters 3 deposited by vacuum sputtering lie on the inner walls of the plates. The outer surfaces of the plates are coated with "black body" gray paint with known integrated and spectral absorptivity. The plates are symmetric and interchangeable. The metal tube 4 supporting the structure simultaneously serves as a housing for the current-conducting wires. The strength of the thermal pile signal is determined by the value of the thermal flux passing

/63

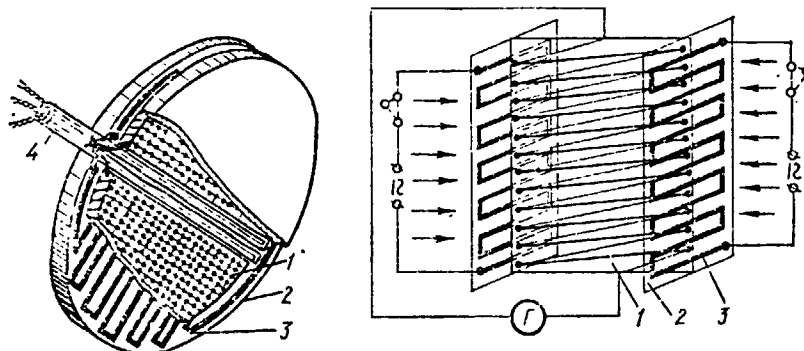


Fig. 1. Schematic and layout of absolute two-sided radiometer

through the transducer and does not depend on the nature of the transducer, that is, on whether the plate is heated by the action of the radiant flux or by the electric power of the heater. This property of the transducer underlies the principle of replacing regimes.

When measurements are taken in conditions of vacuum in a steady-state of the system source-environment-detector, the heat balance equation of the sensor is of the form:

$$q_1 - q_2 = \frac{1}{R} (T_1 - T_2) + a(q_{2\phi} - q_{1\phi}) + \epsilon\sigma(T_1^4 - T_2^4), \quad (1)$$

where  $q_1$  and  $q_2$  are the energy received by the first and second plates [respectively];

$q_{1\phi}$  and  $q_{2\phi}$  are the fluxes irradiated by the background at the first and second plates [respectively];

$R$  is the effective thermal resistance of the auxiliary wall-transducer;

$T_1$  and  $T_2$  are the temperature of the surfaces of the first and second plates; and

$a$  and  $\epsilon$  are the integrated absorptivity and emittance of the ray-sensing surfaces of the plates.

In the following, for simpler form, we adopt the notation

$$\Delta = a(q_{2\phi} - q_{1\phi}) + \epsilon\sigma(T_1^4 - T_2^4).$$

The technique of measuring the radiant thermal flux is based on an analysis of Eq. (1).

In the compensation regime, the plate temperatures are identical, and the electrical signal of the transducer is zero. Here

$$q_1 = q_2 + \Delta. \quad (2)$$

The transducer serves as the zero instrument. Let us denote:  $q_1^e$  and  $q_2^e$  are the energies received by the plates in the electric heating regime, and  $q_1^0$  and  $q_2^0$  are the energies fed to the plates in the irradiation regime. The radiant energy is measured by successive employment of two regimes: exposure and electric heating, according to the equations

$$q_1^0 - \Delta = q_2^e, \quad (3)$$

$$q_2^0 - \Delta = q_1^e. \quad (4)$$

The system (3-4) is solved for  $q_1^0$  and  $\Delta$ . In the radiation regime, one plate is exposed to the radiant flux being measured. During this time the other is shaded and is heated at the electric heater. The heating intensity is specified so that the transducer signal is equal to zero. The estimate of the quantity  $\Delta$  is made in the second regime. Here the action of the irradiation at the detector is halted and the regime of simultaneous electric heating of both plates is introduced. The regime of heating the shaded plate is retained as before. When the signal of the transducer is equal to zero, the intensity of electric heating of the receiving plate is wholly adequate to the magnitude of the radiant power absorbed by the plate in the first regime. The method of compensation makes it possible to measure the radiant energy without determining the sensitivity of the thermoelectric pile.

Another state of the detector is the one in which the temperatures of the plate are not equal. In this case the signal of the transducer differs from zero and is directly proportional to the penetrating thermal flux:

$$q_1 - q_2 = \frac{e}{c}, \quad (5)$$

and when  $q_2 = 0$ ,  $q_1 = e/c$ , where  $e$  is electrical signal of the transducer, and  $c$  is the sensitivity of the radiometer. The magnitude of the flux and sensitivity according to [5] are determined by the total replacement method. The method consists in the successive employment of the regimes of exposure and the electric heating of the plate according to the conditions

$$q_1^0 = \frac{e}{c},$$

$$q_1 = \frac{e}{c}.$$

Procedurally, the experiment is carried out as follows. The exposed plate is irradiated with the radiant flux being measured. The other plate is shaded. The transducer signal is recorded. Then the action of the measured flux on the detector is halted and the regime of electric heating of the previously irradiated plate is introduced. The intensity of electric heating of the plate is specified so that signals of the radiometer in both regimes are the same. The sensitivity is determined in the electric heater regime:

164

$$c = \frac{e}{q_1}$$

The measured incident flux is:

$$q_1^n = \frac{1}{a} q_1^0 = \frac{1}{a} q_1^{\text{a}}$$

In the range of the flux measured with the instrument, the instrument sensitivity does not depend on the power fed to the plate. Considering this property, other methods of measurement have been developed: the method of incomplete replacement of the regimes and the method of combination (simultaneous replacement) of regimes.

The method of incomplete replacement consists in the calibration of the radiometer being carried out based on an arbitrary electric power, within the limits of measurement, according to the equation given in [6]. The sensitivity can be determined before the beginning of exposure and can be verified in the intervals between any two measurement regimes.

Of particular interest is the method of combination (simultaneous replacement) of the regimes. The method determines the sensitivity of the radiometer and measures the radiant flux that interrupting exposures. This advantage of the method is especially important as conditions when it is impossible to annul the action of the measured flux on the detector. The measurements are conducted in two stages: initially the plate exposed is irradiated with the radiant flux being measured and the transducer signal is recorded. Then, without interrupting the exposure to the radiant flux, extra radiant electric power is fed to one of the plates. The radiometer is calibrated based on the ratio of the auxiliary signal to the additional power producing the signal:

$$c = \frac{\Delta e}{\Delta q_1} = \frac{\Delta e}{\Delta q_2}. \quad (7)$$

When the methods of incomplete replacement and combination of regimes are used, the temperatures of the plates in the calibration and measuring regimes are not the same. Therefore, neither are the values of  $\Delta$  the same. Within the range of the fluxes measured with the instrument, the difference between the temperatures of the irradiated and shaded plates does not exceed  $3^\circ \text{ K}$ . In order to retain the stability of the heater exchange conditions of the detector with the ambient environment in the two regimes, the ratio  $\Delta c/e$  is selected as equal to approximately 0.1, which corresponds to a change in the temperature difference by no more than  $0.3^\circ \text{ K}$ . Here the systematic error caused by the inequality of  $\Delta$  in the two regimes can be neglected. The selection of the method is determined on the basis of the conditions of optimizing the measurements.



The sensitivity of the detector to the flux accepted depends on the properties of the thermal battery and of the conditions of heat transfer of the plate with the ambient environment. A quantity characterizing properties of the thermoelectric converter itself and independent of the state of the ambient environment is the sensitivity of the thermoelectric converter to the penetrating flux:

165

$$C = \frac{eR}{T_1 - T_2} \quad (8)$$

These methods of measurement have been developed on the assumption of adequacy of plate heating in the regimes of irradiation and electric heating, and also the complete interchangeability of plates. Obviously, these assumptions are actually only approximately met in reality. The measures of both approximations must be estimated. The measure of nonidentity of plates is due to the inequality of the effective thermal resistances of the sides, each of which is the sum of series-connected thermal resistances: of the blackening ink, of the two aluminum oxide films, of the aluminum plate, and of the layer of resin bounding the plates to the transducer. The measure of nonidentity of plates measured in the working range of the instrument does not exceed 0.4 percent.

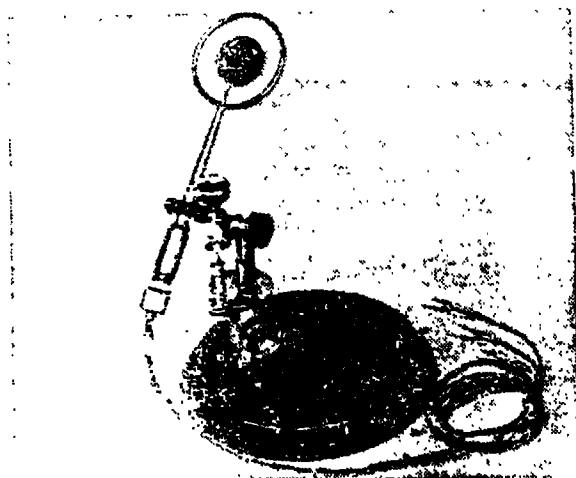


Fig. 2. General view of absolute two-sided radiometer

The nonidentity of the regimes is due to the fact that the radiant energy is fed to the layer of the blackening coating, and the electrical energy is released at the inner side of the plate. The measure of this nonidentity is the ratio of the fluxes passing through the transducer in each regime given the condition that the energies received are equal. In the theoretical and experimental estimates, the measure of nonidentity of regimes does not exceed 0.3 percent.

Both these measures of nonidentity were taken into account in determining the systematic error of the instrument.

The radiometer is constructed on a three-coordinate stand. The general view is shown in Fig. 2.

Main specifications of radiation detector

Range of flux measured	0-2000 w/m <sup>2</sup>
Diameter of ray-sensing plates	34.1 mm
Absorptivity of plate surface	0.95
Thermal resistance of transducer	0.8.10 <sup>-3</sup> m <sup>2</sup> .deg/w
Resistance of electric heaters	500 ohms
Sensitivity of radio-meter to penetrating flux	0.06 mv/w./m <sup>2</sup>
Inertia (time constant)	2.5 sec
Error of measurement	1.5 percent

/66

#### REFERENCES

1. Gerashchenko, O. A., Osnovy teplometrii (Fundamentals of Thermometry), "Naukova dumka", Kiev, 1971.
2. Kedrolivanskiy, V. N., and Sternzat, M. S., Meteorologicheskiye pribory (Meteorological Instruments), Gidrometeoizdat, Leningrad, 1953.

N74-22282

POSSIBILITY OF USING SOURCES OF VACUUM  
ULTRAVIOLET IRRADIATION TO SOLVE PROBLEMS  
OF SPACE MATERIAL SCIENCE

/66

E. T. Verkhovtseva and E. I. Yaremenko

In recent years, as part of the mastery of space, the study of phenomena occurring in solids placed in ultrahigh vacuum when acted on by the electromagnetic radiation of the Sun is gaining growing urgency. The fraction of energy of solar radiation arriving in the regional vacuum ultraviolet is a very small quantity  $\sim 10^{-2}$  percent compared with overall radiation energy [1-3]. However, in spite of this, the effect of vacuum ultraviolet (UV) of radiation on the properties of materials can be appreciable. This is because the energy of the quanta of the short-wave electromagnetic radiation is somewhat greater than the energy for quanta of the visible and infrared wavelength range. On the other hand, vacuum UV radiation is absorbed in a very thin surface layer of materials  $\sim 10^{-4} - 10^{-7}$  cm. Therefore, the specific dose of absorbed UV radiation can be very appreciable. Short-wave irradiation in the 2000-100 Å range can cause electronic excitation and ionization of ions, followed by changes in electrical, optical, and mechanical properties of materials. When this radiation is absorbed by the surface layer, the transparency of windows can deteriorate, the stability of mirror reflective coatings can be disturbed, and light coatings can be darkened. Moreover, these changes in the properties of the surface layer of solids can affect bulk properties. Based on the foregoing, it becomes necessary to investigate the radiation stability of materials that are of interest to spacecraft designers, with respect to irradiation simulating the radiation of the Sun in vacuum ultraviolet, for which sources of vacuum UV radiation are necessary.

In this review we examine the sources of vacuum UV radiation from the standpoint of their possible use in irradiating materials used in space.

First of all, let us formulate the requirements that must be satisfied by the source.

1. The spectral and energy characteristics of irradiation of the source must correspond to solar radiation. On the basis of the energy distribution curve of solar radiation in the region of vacuum ultraviolet shown in Fig. 1, the spectrum of source radiation must be continuous with a long number of emission lines imposed on it, among which the brightest must be the emission  $L_{\alpha}$  line of atomic hydrogen.

2. To produce the dose of vacuum UV radiation corresponding to long-term exposure of solar radiation on the material with a relatively short experimental period, it is necessary that the flux of radiation energy of the source somewhat exceeds the corresponding flux of solar energy.

167

3. The possibility of input of radiation from the source into a chamber with ultrahigh vacuum ( $10^{-8} - 10^{-9}$  mm Hg) where the irradiated object is located must be provided for. Since for radiations with wavelength shorter than 1050 Å (the transmission band of LiF), mechanically strong transparent materials are absent, radiation with wavelength  $\lambda < 1050$  Å must be introduced into the high-vacuum chamber through an open aperture.

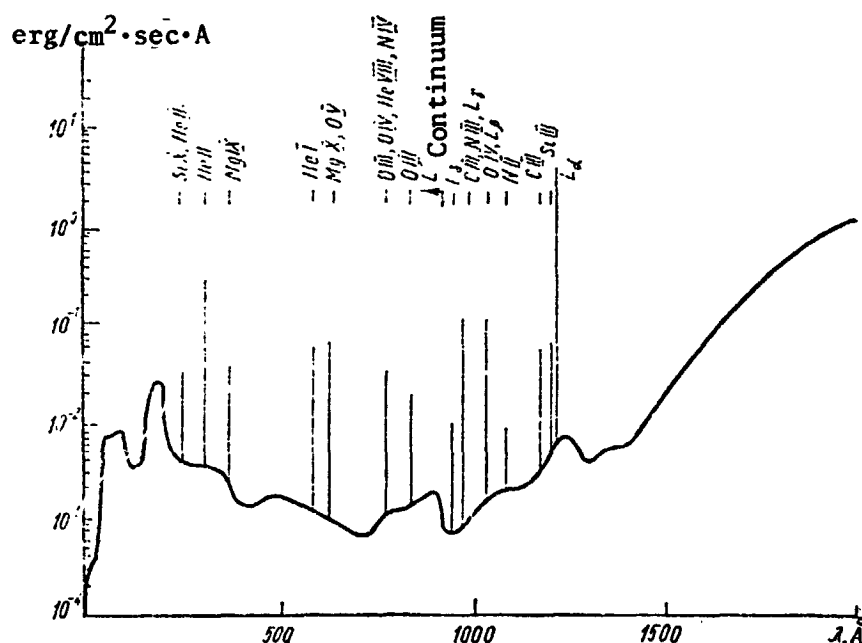


Fig. 1. Distribution of solar energy and the short-wave region of the spectrum for the quiet Sun near its mean activity level [1, 2]. All faint lines are included in the background; the lines whose radiation intensity is greater than the background are singled out; close-lying lines are combined, and the ordinates of the apex relate to their sum.

4. Sensitive radiation with  $\lambda < 1050$  Å is introduced through the open aperture, nowhere the particles except for the protons of the vacuum UV must strike the source at the at the surface of the irradiated object.

103

5. To investigate changes in the properties of materials upon prolonged exposure to solar radiation, the service life of the source must be sufficiently long (we have in mind several days of operation).

In addition to these requirements on the source, it is desirable that also the following conditions be met: 1) introduce the radiation from the source into the high-vacuum chamber in a wide solid angle, so that this will permit irradiating the objects with a greater surface area; 2) since solar radiation for a short time interval continuously acts on the object in space, the source must operate in a continuous regime. As for the stability of operation, less stringent requirements it must obviously impose on the source of light used for purposes of space material science lend on the source intended for use in purely physical investigations, namely: in this case the instability of operation of 5-10 percent is quite satisfactory.

Let us consider to what extent sources of vacuum UV satisfy these requirements. The problem involves a specific case -- irradiation of an object with an area  $100 \text{ cm}^2$ . In our presentation, first we consider sources operating at the pressure of the working gas from several tenths to several hundredths of millimeters Hg. This pertains to sources whose operating basis is the irradiation of various types of gas discharges. Then we consider sources operating in conditions of high vacuum ( $10^{-5}$  -  $10^{-6}$  mm Hg). These sources include the radiation of a beam of electrons accelerated in a synchrotron, irradiation of various modifications of vacuum sparks, and irradiation of electron-excited supersonic gas jet escaping into vacuum.

/68

#### Source Emitting Continuum and Multiline Spectrum of Hydrogen Molecules (Hydrogen Flame)

When excited in an electric discharge at low pressure (several tenth of millimeters of a mercury column), hydrogen emits intense radiation in the vacuum ultraviolet range in the limits 900-2000 Å. It consists of a continuum given at  $\lambda = 1670 \text{ Å}$  and extending into the region of longer wavelength all the way to  $\lambda = 5000 \text{ Å}$ , of a multiline molecular spectrum in the region 1670-900 Å and a Lyman series of atomic hydrogen with a resonance line  $\lambda = 1215.7 \text{ Å}$ .

Most hydrogen lamps have vacuum ultraviolet radiation emitted by the positive column of the glowing and arc discharges. Hydrogen lamps with glowing discharges are classified as lamps with cold cathode and, as a rule, are high-voltage. At different times in the literature, various designs of hydrogen lamps with cold cathode have been described [4-9]. Usually, a quartz or pyrex capillary

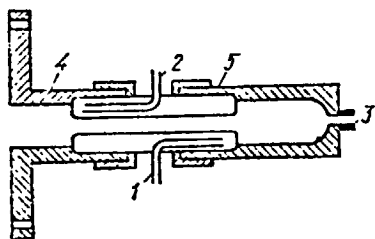


Fig. 2. Capillary discharge tube with external electrodes:  
1, 2. water inlet and outlet  
3. hydrogen admission  
4. anode  
5. cathode

cooled with water and located between the cathode and the anode are incorporated in these lamps (Fig. 2). In addition, wide use is made of hydrogen lamps of arc discharge with hot cathode [10-15]. The use of hot cathodes with a small cathode potential drop provides for high current values (several amperes) at the working supply frequency of the lamp of several tenths of volts. Low-voltage hydrogen lamps are convenient in operation, since they do not require cumbersome power sources. Discharge conditions similar to those observed in the positive column of the glowing and arc discharges occur in the nonelectrode discharge. The main advantage of the latter is the purity of the hydrogen plasma. The design of the source itself is extremely simple [16-17].

As we can see from Fig. 3, good correspondence between the spectral distribution of the energy of hydrogen lamp radiation and solar radiation is observed only in the region 1000-1600 Å. Fig. 3 is supplemented by Table 1, in which for comparison we present the radiation energy fluxes of a hydrogen lamp used with a LiF window, and the radiation energy of the Sun in various spectral regions. From the data it follows that in the region of vacuum ultraviolet the radiation spectrum of the hydrogen lamp is somewhat more intense than the solar spectrum. In the FTINT AN USSR\*, a hydrogen lamp with a LiF window has been developed, whose radiation intensity in the wavelength range 1050-1700 Å at a distance of 30 cm at the location of an object having an area of 100 cm<sup>2</sup> is 3·10<sup>3</sup> erg/cm<sup>2</sup>·sec [19]. The intensity of solar radiation in the same range is two orders of magnitude less, ~ 26 erg/cm<sup>2</sup>·sec [1, 2].

The input of radiation from the hydrogen lamp into the chamber containing the irradiated object, in which the pressure must not be more than (10<sup>-8</sup> - 10<sup>-9</sup> mm Hg), can be provided in two ways: 1) through a vacuum-tight LiF window transmitting hydrogen lamp radiation in the region of the vacuum UV with the wavelength interval 1100-2000 Å; and 2) through an open aperture by using a multistage system of differential evacuation stored between the source and the high-vacuum chamber, to provide for a pressure drop from several millimeters of mercury in the source to 10<sup>-8</sup> - 10<sup>-9</sup> mm Hg in the chamber containing the irradiated

/69

\* [FTINT (transliterated) of the Ukrainian SSR Academy of Sciences]

object. The use of the LiF window has the advantage that in this case various kinds of particles are not transferred from the source into the vacuum chamber. Moreover, the aperture of the light beam exiting from the source is not reduced. However, the use of the LiF window does have disadvantages: it emits not all the radiation of the hydrogen lamp (900-2000 Å) into the high-vacuum chamber, but some of it (1100-2000 Å). In addition, during the operation of the hydrogen lamp, the transmission capacity of the LiF windows is sharply reduced, and the short-wave cutoff of LiF transparency, initially in the wavelength region 1050-1100 Å, is shifted toward the long-wave spectral region. These disadvantages to some extent can be eliminated by feeding the radiation into the high-vacuum chamber through the open aperture by using a system of differential evacuation. However, the use of the latter entails the following difficulties. Placing it between the gas-discharge lamp and the high-vacuum chamber removes the light sources to a considerable distance from the chamber and thus reduces the illumination from the source at the location of the irradiated objects. Accordingly, the feasibility of satisfying the conditions of correspondence between the fluxes of radiation energy from the hydrogen lamp and from the Sun at the location of the object is placed in doubt. In addition, the diaphragms that are part of the system of differential evacuation, with which the pressure drop is achieved, considerably reduce the solid angle of the radiation flux introduced into the chamber, and thus significantly lower the irradiated area of the object.

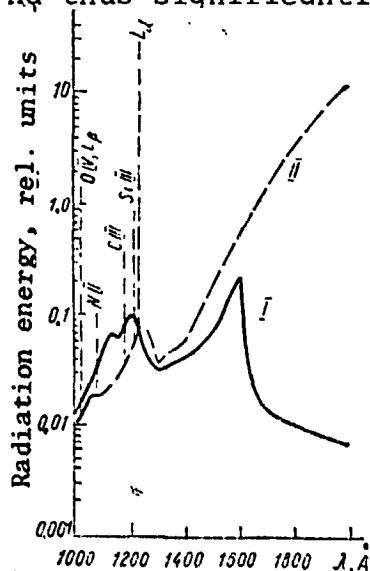


Fig. 3. Spectral distribution of energy in relative units:  
I. hydrogen lamp radiation [18]  
II. solar radiation [1, 2]

The hydrogen lamp satisfies the requirement of a continuous regime of operation and radiation stability.

Thus, the hydrogen lamp with the LiF window in the spectral region 1100-2000 Å satisfies the main requirements that are imposed on the light source intended for use for purposes of space material science, with the exception of the requirement of duration of operating time. To provide a continuous cycle of operation of the hydrogen lamp with the LiF window through a long time interval in simulation chambers, in view of the simplicity of its design it is obviously useful to install two lamps that operate in time.

The hydrogen lamp with the LiF window is already been used in experiments on the changes in the properties of materials placed in ultrahigh vacuum [18, 20].



Table 1

Wavelength interval $\Delta\lambda, \text{ \AA}$	Energy flux, $\text{erg/cm}^2 \cdot \text{sec}$ of Sun at 1 A.U. [1,2]	of hydrogen lamp at 17 cm [18]
1100—1300	5.4	$1.1 \cdot 10^3$
1300—1450	0.9	$4.5 \cdot 10^3$
1450—2000	204.3	$4.0 \cdot 10^3$

To simulate the action of solar radiation in the region 1550–2200 Å, a convenient light source is the hydrogen lamp with the fuse quartz window, model DVS-200, produced domestically. This is a low-pressure arc lamp ( $\approx 2$  mm Hg) with a heated cathode. The divergence of the light beam of the lamp is  $35^\circ$ , and the absolute intensity of radiation at 10 cm is approximately  $10^5 \text{ erg/cm}^2 \cdot \text{sec}$  [21].

### Gas-discharge Sources of Vacuum UV Radiation Filled with Inert Gases

To understand processes occurring in solids where they are irradiated with vacuum UV-radiation from the Sun, it is important to carry out additional investigations associated with the irradiation of solids with a narrow wavelength through range or with monochromatic lines. For this purpose, it is convenient to use the continuum irradiation of inert gases, since the continuum of each inert gas encompasses a fairly narrow spectral region in the interval 500–2000 Å (Fig. 4). In addition, it is also useful to make use of resonance lamps filled with inert gases, their mixtures, or with mixtures of inert gases and hydrogen, nitrogen, and oxygen.

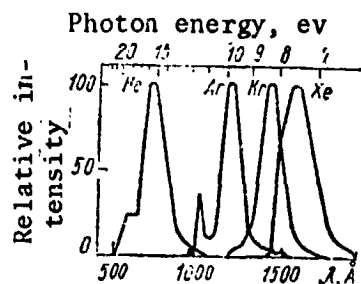


Fig. 4. Continuum of inert gases [22]

The continuous spectra of inert gases are best excited to the high-voltage, impulse condensed discharge controlled with a thyatron at a gas pressure of the order of several hundredth of millimeters of mercury [22]. The appearance of these spectra is associated with the formation in the discharge, as the result of several processes of collision, of excited gas molecules [23]. An very convenient and simple design of a gas-discharge too poor exciting the helium continuum is

given in [24]. The continuous spectra of heavy inert gases (Ar, Kr, and Xe) can be obtained in soldered lamps with windows.

Table 2 presents, for a comparison, the integrated radiation energy fluxes of continuum of inert gases and of the Sun.

Favorable conditions for exciting the resonance lines He I ( $\lambda = 584.3$  and  $537.0$  Å); Ne I ( $\lambda = 735.9$  and  $743.7$  Å); Ar I ( $\lambda = 1048.2$  and  $1066.7$  Å); Kr I ( $\lambda = 1164.9$  and  $1235.8$  Å); and Xe ( $\lambda =$

1295.6 and 1469.6 Å) are provided in the positive column of the glowing and arc discharge at low current density (up to 1 a/cm<sup>2</sup>) [26-29], or in a nonelectrical discharge at low partial pressure of Xe or Kr (0.01-0.1 mm Hg) in a mixture with He or Ne (several millimeters of the mercury column) [30-35]. In the latter case, matching the operating regime of the generator of the ultrahigh frequency oscillations with the gas-discharge load is vital. Different methods of matching the operating regime with a generator with load are described in [36].

The low-voltage discharge makes it possible to obtain a radiation flux of  $3 \cdot 10^{16}$  photons/sec in the resonance line He I  $\lambda = 584$  Å is described in [29]. The design of a stable nonelectrode resonance krypton lamp emitting  $2 \cdot 10^{17}$  photons/sec for 80-120 hours of continuous operation is described in [34]. Xenon arc low-voltage resonance lamp KsR-1 and KsR-2 (with water cooling) were developed in Soviet Union. Table 3 presents several parameters of these lamps, including the fluxes emitted through the fluorite windows in each of the resonance lines 1295.6 and 1469.6 Å.

From the data in Table 3 it follows that resonance lamps emit monochromatic lines, whose radiation flux is three-four orders of magnitude greater than the radiation flux of the brightest line in the vacuum UV spectrum of the Sun -- the hydrogen  $L_{\alpha}$  line. /71

Table 2

Wavelength interval $\Delta\lambda$ , Å	Energy flux, erg/cm <sup>2</sup> ·sec	
	of Sun at 1 A.U. [1,2]	of inert-gas continuum*
580-1100 (He, $\lambda_{\max} = 710$ Å)	1.0	$\approx 10^5$
740-1000 (Ne, $\lambda_{\max} = 823$ Å)	0.6	not measured
1050-1550 (Ar, $\lambda_{\max} = 1270$ Å)	7.0	$\sim 10^3$
1250-1800 (Kr, $\lambda_{\max} = 1500$ Å)	42.0	$\sim 10^3$
1480-2000 (Xe, $\lambda_{\max} = 1650$ Å)	204.0	$\sim 10^3$

\* The radiation energy fluxes of the continuum of inert gases are estimated roughly, to a precision of the order of magnitude, by using the data of intensity in the principal maximum of the continuum at the output of the monochromator [22] and the averaged values of the efficiency of the platinum-coated grid [25].

The input of the continuous radiation of inert gases and the monochromatic lines in the spectral region 1100-2000 Å into the high-vacuum chamber is best done through windows made of lithium fluoride, calcium fluoride (fluorite), leucosapphire, quartz, or several other materials. To introduce radiation with wavelength shorter than 1050-1100 Å, it is necessary to use a system of intermediate chambers with separate evacuation to ensure a pressure drop from several millimeters of mercury in the source to  $10^9$  mm Hg in the high-vacuum

chamber. To reduce to the minimum the losses in intensity the light passes through the differential evacuation system, and also

to increase the aperture of the light beam introduced in high-vacuum chamber, the work [37] proposes using an optical system of focusing the emission at the apertures of the diaphragms, for this purpose. The scheme of this input of radiation from a helium lamp operating at  $P = 10$  mm Hg into the high-vacuum chamber with  $P = 10^{-9}$  mm Hg is shown in Fig. 9. A system of three intermediate chambers with millimeter diaphragms makes it possible to achieve the required pressure drop (chamber I:  $P = 5 \cdot 10^{-3}$  mm Hg,  $S_1 = 162$  l/sec; chamber II:  $P = 3 \cdot 10^{-5}$  mm Hg,  $S_2 = 91$  l/sec; chamber III:  $P_3 = 5 \cdot 10^{-7}$  mm Hg,  $S_3 = 32$  l/sec). To focus the radiation, use is made of three identical elliptical aluminum-plated mirrors, whose foci coincide with the chamber diaphragms. Angles of incidence of light from mirrors ( $\approx 80^\circ$ ) are used; the aperture angle of the beams is  $6^\circ$ . Experimental verification showed that the losses of intensity due to diaphragming of the beam at the millimeter openings do not exceed 6 percent for each chamber. The intensity losses in reflection from the mirrors in the spectral region 500-1100 Å were not measured. However, as calculations conducted with literature data [38] showed, the total intensity losses (for reflection and due to diaphragming of the beam at the openings) when the radiation passed through the intermediate chambers does not exceed one order of magnitude. The flux of radiation energy of the helium lamp, considering the losses in the intermediate vacuum chambers that the location of the object with an area  $S = 100$  cm<sup>2</sup> then is about 1 erg/cm<sup>2</sup>·sec. When objects with an area  $S = 10$  cm<sup>2</sup> were investigated, the radiation energy flux of the helium lamp at the object location exceeded the radiation flux of solar energy in the spectral region 580-1100 Å by approximately one order. Therefore, the helium continuum evidently is best used for irradiating objects with a smaller surface area. The following must be added to the foregoing: implementing the concept of using an optical system associated with intensity losses within the limits of one order of magnitude in introducing radiation into a high vacuum chamber requires both the use of advanced experimental techniques (fabrication of high grade mirrors, deposition thereon of high quality coatings, and the use of intermediate chambers evacuated with nonoil pumps)<sup>1</sup>, as well as conducting a great deal of experimental work associated principally with studying changes in the coefficients of reflection of mirrors in the spectral region below 1100 Å with time in the operating conditions of the source. Several results of these kinds of investigations conducted in the spectral region 1100-2000 Å are given in the study [40].

<sup>1</sup> The presence in intermediate chambers of the vapor of the diffusion pump oil promotes the formation of optical films on the surfaces of mirrors when exposed to vacuum UV radiation [40]. This circumstance can lead to a reduction in the coefficients of mirror reflection in the spectral region below 1100 Å.

Table 3

Lamp type	Dis. cur. amp	Vol-tage, V	Rad. flux, photons/sec	
			1295,6 Å	1469,6 Å
KsR-1	0,2	40-50	$4 \cdot 10^{14}$	$8 \cdot 10^{15}$
KsR-2	1,0	30	$6 \cdot 10^{14}$	$4 \cdot 10^{16}$

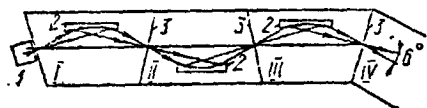


Fig. 5. Scheme of introducing radiation from the helium lamp ( $P = 10$  mm Hg) into the simulation chamber ( $P = 10^{-9}$  mm Hg) [37]:

1. lamp
2. elliptical mirror
3. diaphragm
- I-IV. chambers

the input of radiation into the high-vacuum chamber, is determined by the time during which the coefficients of mirror reflection in the spectral region below 1100 Å retain a high value. Owing to the absence of these kinds of data, no specific conclusions as to the operating time of a lamp with a system of differential evacuation can be made.

The stability of operation of the gas-discharge lamps considered here is satisfactory.

#### Source Emitting Lyman Continuum

Lyman, on discharging a capacitor through a narrow capillary filled with helium to a pressure of several millimeters of mercury, detected a continuum extending from the visible to the X ray spectral region [41-43]. More detailed investigations showed that the determining parameter of the discharge emitting the Lyman continuum, is the current density (the current density must be about  $30 \text{ A/cm}^2$ ), and the nature of the gas and its pressure plays no appreciable role [44]. The appearance of the continuous

The operating regime of gas-discharge lamp emitting the most intense continuous spectrum of inert gases is of the impulse type, with a high pulse repetition frequency rate. However, for discharge in helium if the pulse firing rate is selected so that the interval between subsequent pulses is equal to the discharge after glow time, the discharge in the pulse regime of excitation will yield radiation that is continuous with time. Resonance lamps have a continuous operating regime.

The life time of gas-discharge lamps of the enclosed type is limited to several tens of hours of operation due to a reduction in the transparency of the LiF window in the course of lamp operation. The service life of gas discharge lamps of the open type, using an optical system for

spectrum at high current densities in the gas-discharge lamp is caused by free-free and free-bound transitions [45]. The main disadvantages of the Lyman source [41-43] lies in the superimposition on the continuous spectrum, especially in the region below 1800 Å, of a line emission spectrum and absorption of particles of the material of the capillary walls. In addition, rapid breakdown of the latter occurs.

/13

Major successes in improving the working parameters of the Lyman continuum source were made by Garton [46]. He was able to prolong the operating life of the source; and in so doing, the continuum was virtually freed of the absorption lines, however below 900 Å a large number of emission lines were observed. In recent years, satisfactory designs of the Lyman continuum source have appeared, making it possible to achieve radiation without admitting gas in the discharge chamber [47, 48]. The electrical supply circuit of a tube with automatic and manual firing is given in the monograph [49].

The question of the correspondence of the energy characteristics of radiation from the source and from the Sun remains open, owing to the absence of experimental data in the literature dealing with the spectral distribution of the radiation intensity of the Lyman continuum and the magnitude of its integrated flux in the region of vacuum UV.

Introducing radiation from the source at a pressure from several hundredths to several units of millimeters of mercury through an open aperture into high-vacuum chamber at a pressure of  $10^{-8}$  -  $10^{-9}$  mm Hg requires a differential evacuation system, whose advantages and disadvantages we have already noted. Owing to the absence of data dealing with the flux of radiation energy of the Lyman continuum in the region of vacuum UV, no conclusions about the satisfaction of conditions of the correspondence of radiation energy fluxes from the source and from the Sun at the object location can be made, with allowance for the losses in radiation intensity in the intermediate vacuum chambers.

The Lyman continuum source does not satisfy the requirement of continuous operation. The stability of its radiation is quite satisfactory. Specific data on its operating time are not given in the literature.

#### Source with Condensed Low-pressure Spark Discharge

A condensed spark discharge in a gas of low pressure (from several hundredths to several millimeters of mercury) and a current density up to  $30 \text{ ka/cm}^2$  leads to the appearance of intense ionization and excitation of lines belonging to ions with a high

ionization multiplicity. Using this source, radiation spectra of highly ionized atoms of inert gases, nitrogen, oxygen, and other gases were obtained, chiefly in the spectral region 200-1000 Å.

There are many designs of spark sources [50-54]. The most modern design is given in the monograph [49, Fig. 5]. A capillary pulse source with a thyratron control developed in the USSR at the State Optical Institutes imeni S. I. Vavilov has been introduced commercially. Its prototypes were built under the designation IGI-1 [55].

Since there are no data in the literature on the distribution of the energy flux in the spectrum of condensed spark discharge in a gas, we cannot compare the energy characteristics of the radiation from a source and from the Sun at narrow spectral regions in the interval 200-1000 Å. However, from the data of the study [56], the integrated flux of radiation energy from the source in the spectral region 500-1050 Å is  $8 \cdot 10^2$  erg/sec for a light beam aperture of  $7.5^\circ$ . The radiation intensity of the Sun in this range is about 1 erg/cm<sup>2</sup>.sec [2]. The radiation energy flux from the source at the site of an object with an area of 100 cm<sup>2</sup> is 8 erg/cm<sup>2</sup>.sec, that is, it corresponds to solar radiation in order of magnitude. However, if it is assumed that to introduce the radiation from the source into a chamber containing the irradiated object, one must use a differential evacuation system, the radiation flux in the high-vacuum chamber at the location site of an object with an area  $S = 100$  cm<sup>2</sup> corresponds to the best of cases, but it is most probable that it is smaller than the solar radiation flux. Accordingly, this source evidently is not rationally used in the irradiating large-area objects. /74

The condensed discharge in a gas gives a time-pulsed radiation; its stability is 2-3 percent; its operating time is extended. However, when an optical system installed in intermediate vacuum chambers with differential evacuation is used for the input of radiation into the high-vacuum chamber, the operating time of the source is determined by the time during which the coefficients of the mirror reflection in the region 200-1000 Å retain high values during system operation.

#### Synchrotron as a Source of Vacuum UV Radiation

From the main principles of classical electrodynamics, it follows that an electron accelerated to relativistic velocities must emit energy. This fact was taken into account in designing high-energy electron accelerators (betatron and synchrotron). The theory of the radiation of relativistic electrons is covered by the studies [57-58].

Electromagnetic radiation of electrons in a synchrotron yields an intense continuous spectrum from the x-ray to the infrared region. The nature of the radiation spectrum of electrons in the synchrotron in the region of the vacuum UV does not correspond to the solar spectrum, since it has no radiation of numerous lines superimposed on the continuous spectrum. Since the spectral distribution of energy and the short-wave cutoff of this synchrotron radiation are determined by the energy of the accelerated electrons  $E$  (Fig. 6), then obviously by selecting  $E$  one can obtain the distribution of the synchrotron radiation energy in an individual spectral region that is close to the solar distribution. As an example, Fig. 7 presents, in the spectral region below, 500 Å, the energy distributions of solar radiation and radiation of the DESY synchrotron [60] for  $E = 1$  Bev.

175

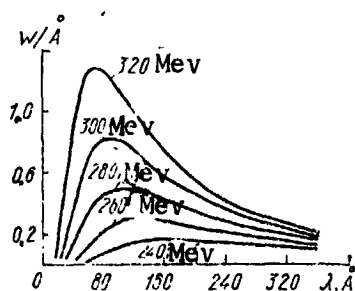


Fig. 6. Spectral distribution of radiation intensity (in relative units) for various electron energies [59]

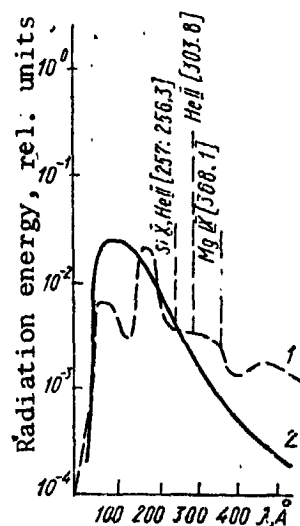


Fig. 7. Energy distribution in the radiation spectra of the Sun (1) [2] and the DESY synchrotron (2) [60] in the region 35-500 Å. The energy of the accelerated electron  $E = 1$  Bev, and the radius of the orbit  $R = 31.7$  m.

In Fig. 8 is presented the energy distribution of solar radiation and radiation from the NBS synchrotron [61], for  $E = 120$  Mev in the wavelength interval 500-1500 Å. These curves are supplemented by Table 4, in which the radiation fluxes of the Sun and of the synchrotron are presented in narrow spectral regions in the interval 40-1500 Å.

It must be noted that the Table 4 gives the radiation fluxes emitted by a single electron during its acceleration in the synchrotron. Since the electron beam in the DESY and NBS synchrotrons contain  $10^{16}$  and  $10^3$  electrons, respectively, the fluxes of synchrotron radiation considerably exceed solar values. Here we must bear in mind that by changing the number of accelerated electrons, one can over wide limits modify the energy flux of the synchrotron radiation.

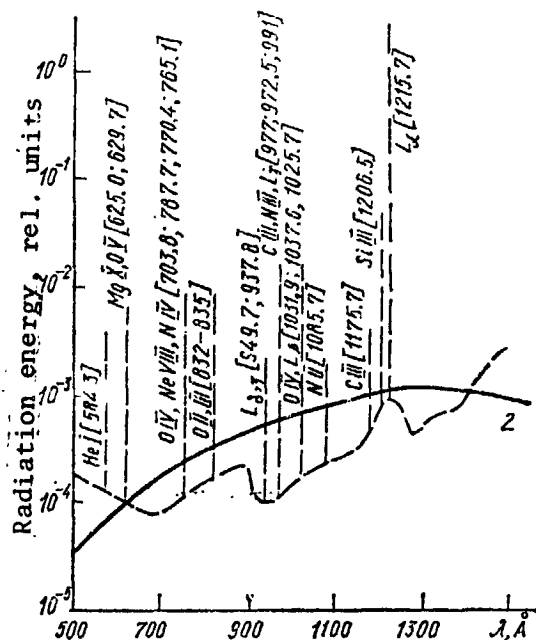


Fig. 8. Energy distribution in the radiation spectra of the Sun (1) [2] and of the NBS [61] in the region 500-1500 Å. The energy of the accelerated electron  $E = 120$  Mev, and the radius of the orbit  $R = 0.83$  m

In addition, the conditions of continuous operation and radiation stability are met.

Based on the foregoing, it can be concluded that synchrotron radiation satisfies virtually all the requirements imposed on the source of vacuum UV intended for use in space materials science, with the exception of the requirement of the correspondence of the nature of the radiation spectrum with that of the solar spectrum. The main disadvantage of the synchrotron is its complexity, cumbersomeness, and high cost.

Since the pressure in the synchrotron is low ( $10^{-6}$  mm Hg), it is not very difficult to introduce its radiation into a high-vacuum chamber at a pressure of  $10^{-8} - 10^{-6}$  mm Hg, while preserving the intensity of radiation at a sufficient level. The high-vacuum chamber can be connected to the synchrotron at a distance of from several meters to several tens of meters [61, 62]. Therefore, introducing synchrotron radiation into it can be achieved through a pipeline of large enough diameter, thus ensuring the possibility of irradiating objects of relatively large areas.

The synchrotron satisfies a very important requirement -- the absence of the transfer of various kinds of foreign particles from the sources to the chamber containing the irradiated object.



Table 4

Wavelength interval $\Delta\lambda, \text{\AA}$	Solar rad. flux at 1 AU, $\text{erg/cm}^2 \cdot \text{sec}$ , [2]	Flux of synchr. rad. flux (E=1 Bev, R=31.7 m) $\text{erg/sec} \cdot \text{el}$ , [50]	Wave-length interval $\Delta\lambda, \text{\AA}$	Solar rad. flux at 1 AU, $\text{erg/cm}^2 \cdot \text{sec}$ , [2]	Flux of synchrotron rad. flux (E=1 Bev, R=31.7 m) $\text{erg/sec} \cdot \text{el}$ , [60]
40-60	0.13	$8.0 \cdot 10^{-5}$	500-600	0.17	$3.0 \cdot 10^{-5}$
60-80	0.14	$9.5 \cdot 10^{-5}$	600-700	0.14	$3.7 \cdot 10^{-5}$
80-100	0.15	$1.0 \cdot 10^{-4}$	700-800	0.11	$4.5 \cdot 10^{-5}$
100-120	0.07	$1.1 \cdot 10^{-4}$	800-900	0.26	$5.2 \cdot 10^{-5}$
120-140	0.06	$9.5 \cdot 10^{-5}$	900-1000	0.24	$5.6 \cdot 10^{-5}$
140-160	0.07	$8.0 \cdot 10^{-5}$	1000-1100	0.26	$5.8 \cdot 10^{-5}$
160-180	0.39	$7.6 \cdot 10^{-5}$	1100-1200	0.29	$5.9 \cdot 10^{-5}$
180-200	0.36	$7.2 \cdot 10^{-5}$	1200-1275	4.97	$4.5 \cdot 10^{-5}$
200-250	0.23	$1.6 \cdot 10^{-4}$	1275-1325	0.18	$3.0 \cdot 10^{-5}$
250-300	0.19	$1.4 \cdot 10^{-4}$	1325-1375	0.26	$2.9 \cdot 10^{-5}$
300-350	0.41	$1.0 \cdot 10^{-4}$	1375-1425	0.26	$2.9 \cdot 10^{-5}$
350-400	0.13	$8.0 \cdot 10^{-5}$	1425-1475	0.5	$2.8 \cdot 10^{-5}$
400-500	0.14	$1.1 \cdot 10^{-4}$	1475-1525	0.96	$2.8 \cdot 10^{-5}$

\* Radiation is concentrated in a cone with an aperture angle of  $1/E$  (if E is measured in Mev).

\*\* Translator's Note: Commas represent decimal points.

#### Source with Vacuum Spark

The plasma of a condensed spark discharge fired in a high vacuum of  $10^{-5}$  -  $10^{-6}$  mm Hg between two electrodes emits multiline radiation of highly ionized atoms of the metal that the electrodes are made of. This discharge was first achieved in the study [63] and came to be called the "hot spark" discharge. A spectrum up to 140 A can be produced with it.

Wodar and Aston [64] suggested a variant of the vacuum spark, which came to be called the "sliding spark" in vacuum. These metallic electrodes are connected with each other with a solid heat-resistant insulator, when voltage is fed at the electrodes a discharge is induced, sliding along the inner surface of the channel in the insulator. Compared with the "hot spark", the "sliding spark" has a low breakdown voltage, greater dimensions of the glowing cloud, adequate operating stability, and less sputtering of the electrode material. Many designs of a source with the "sliding spark" in vacuum have been published in the literature [64-67].

Recently, a three-electrode vacuum spark has become common, in which a "sliding spark" is used in firing to reduce the firing voltage of the main discharge [66, 68]. In the radiation from this spark is observed not only the line spectrum, but also an intense continuum, extending from the visible to the X-ray spectral region. The most successful design of a three-electrode vacuum spark is described in [69].

Of the various modifications of the vacuum spark, from the standpoint of the correspondence of the nature of the radiation spectrum of the spark to the solar radiation spectrum, mention must be made of the three-electrode spark that emits, in addition to the numerous lines of ionized atoms, any of which are presented in the solar spectrum, a continuous spectrum. Owing to the absence in the literature of data on the spectral distribution of the radiation energy flux of the vacuum spark in the wavelength interval 80-2000 Å, the problem of the correspondence between the energy characteristics of the spark radiation and solar radiation in the region of vacuum UV remains open.

Since the spark glows in a high vacuum ( $10^{-5}$  -  $10^{-6}$  mm Hg), introducing its radiation into a chamber at a pressure  $10^{-8}$  -  $10^{-9}$  mm Hg can be done in a large solid angle through a cryogenically cooled channel.

As a result of the intense sputtering of electrodes during operation of the spark, the discharge of atomized metal and dielectric particles from the source into the chamber contained the irradiated object is possible.

The three-electrode vacuum spark operates in a pulsed regime with a low pulse repetition frequency rate (5-10 pulses/sec). Since after 5000-10,000 discharges, the anode in the source wears down [69], which affects the intensity of the radiation spectrum and its composition, the operating time of the vacuum spark is limited. The spark is a fairly stable light source. /77

Based on the foregoing, it can be concluded that the three-electrode vacuum spark does not satisfy the following requirements: absence of discharge of foreign particles from the source into the high-vacuum chamber, regime of continuous operation, and operating time. Moreover, the problem of correspondence between the energy characteristics of the source radiation and solar radiation remains open.

#### Gas-jet Source

In the FTINT [transliterated] of the Ukrainian SSR Academy of Sciences, a vacuum UV source has been developed, operating on a new physical principle. Radiation in the source is emitted by

an excited compact electronic beam of supersonic gas jets streaming into the vacuum, followed by the freezing of the gas jet at cold surfaces. In the region of the jet the gas pressure is sufficient for the normal operation of the source (from several hundredths to several units of millimeters of mercury), while near the jet, owing to the oriented motion of the gas due to its supersonic velocity, the pressure is several orders of magnitude lower ( $\approx 10^{-5}$  mm Hg). A detailed description of the design and the main spectral characteristics of the source radiation are given in [70-72].

When a jet of the gas mixture  $\text{Ar} + 7 \cdot 10^{-2} \% \text{Kr} + 1 \cdot 10^{-3} \% \text{Xe}$  at the energy  $E = 1.1 \text{ keV}$  ( $j_e = 0.15 \text{ a/cm}^2$ ), when the gas pressure in the jet is 0.6 mm Hg, a distribution of the energy of radiation emitted by the jet is obtained in the spectral region 500-1500 Å that is close to the distribution of solar radiation energy (Fig. 9).

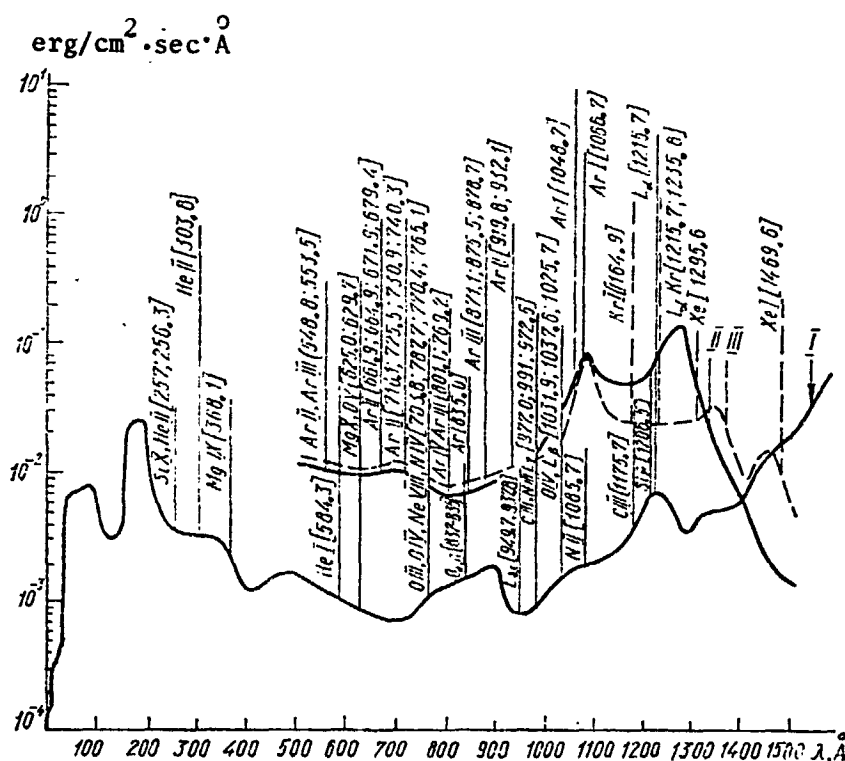
The flux of source radiation energy in this operating regime in the spectral region 500-1200 Å at the distance of 1 m at the location of the object having an area  $S = 100 \text{ cm}^2$  is more than one order of magnitude greater than the corresponding flux of solar radiation energy. In the spectral regions 1200-1275 and 1425-1525 Å, the order of magnitude of both radiation fluxes is the same (Table 5).

The gas-jet source makes it possible to introduce radiation in the spectral region 500-1500 Å in a fairly wide angle through a cryogenically-cooled channel into the chamber containing the irradiated object, in which the gas pressure does not exceed  $1 \cdot 10^{-8}$  mm Hg.

In the operating regime of the source, there is no discharge of different kinds of charged particle, ions, electrons, and metal particles into the high-vacuum chamber. The penetration of the small amount of Ar from the source into the chamber containing the irradiated object, recorded with a mass spectrometer transducer evidently cannot affect the results of the experiment with respect to the effect of vacuum UV radiation on the initial physical properties of the material, since Ar is a chemically low-activity gas and is weakly adsorbed on the surfaces of irradiated objects.

The gas-jet source, whose design is described in [70], does not satisfy the requirement of many hours of operating time. However, a new design of the source has been developed in the FTINT of the Ukrainian SSR Academy of Sciences, which can prolong its operating time to several days. The operating regime of the source is continuous, and the radiation instability does not exceed 4 percent.

Thus, based on the analysis of the properties of sources of vacuum UV radiation from the standpoint of the suitability for purposes of space materials science, the following conclusions can be drawn.



- I. of the Sun [1, 2]
- II. of the gas-jet source operating with an Ar jet at a distance of 1 m [72]
- III. of a gas-jet source operating with a jet of a gas mixture: Ar +  $7 \cdot 10^{-2}$  % Kr +  $1 \cdot 10^{-3}$  % Xe, at the distance of 1 m

Table 5\*

Spectral interval Å, Å	Energy flux, $\text{erg/cm}^2 \cdot \text{sec}$		
	in solar spec. [1,2]	in spec. of gas-jet source	
		$P = 0.6 \text{ mm}, E = 1.1 \text{ kev}$ $j_e = 0.15 \text{ a/cm}, R = 1 \text{ m}$	
		Ar	Ar + $7 \cdot 10^{-2} \% \text{ Kr} +$ $+ 1 \cdot 10^{-3} \% \text{ Xe}$
1525-1475	0,96	0,07	0,3
1475-1425	0,5	0,01	0,9
1425-1375	0,26	0,3	0,6
1375-1325	0,26	0,8	1,5
1325-1275	0,18	3,1	1,6
1275-1200	4,97	8,3	3,8
1200-1100	0,29	5,5	3,9
1100-1000	0,26	20,6	19,5
1000-900	0,24	2,9	2,6
900-800	0,26	1,3	1,5
800-700	0,11	1,0	1,2
700-600	0,14	1,3	1,6
600-500	0,17	1,2	1,4

\* Translator's Note: Commas represent decimal points.

objects with large areas. Accordingly, two sources can be recommended for simulating the action of solar radiation at a wavelength range less than 1100 Å on objects with large areas -- the synchrotron and the gas-jet source.

To understand processes occurring in solids when they are irradiated by vacuum UV solar radiation, it is important to conduct additional investigations on irradiating solids with narrow wavelength intervals or monochromatic lines. For this purpose it is convenient to use simple sources, with the emission of the continuum of inert gases, and also resonance lamps filled with inert gases and their mixtures.

To simulate the action of solar radiation in the wavelength range 1100-2000 Å on materials, a hydrogen lamp with a lithium fluoride window can serve as a convenient light source.

In the spectral region below 1100 Å major difficulties arise, principally related to introducing the radiation into a chamber with an ultra-high vacuum, the absence of discharging of any foreign particles from sources into the chamber, and the possibility of irradiating

/79

# REFERENCES

1. Detwiler, C. et al., Ann. de Geophys., 17, 263 (1961).
2. Hinteregger, H. E., Space Science Rev., 4(4), 461 (1965).
3. Johnson, F. S., J. Meteorology, 11, 431 (1954).
4. Johnson, F. S., Watanabe, K., and Tonsey, R., JOSA, 41, 702 (1954).
5. Robin, S., and Vodar, B., J. Phys. et Radium, 13, 671 (1952).
6. Gerasimova, N. G., and Kulikov, S. A., OMP, 1, 17 (1958).
7. Vilesov, F. I., Akopyan, M. Ye., and Kleymenov, V. I., PTE, 6, 150 (1963).
8. Zaytsev, V. S. et al., Ukr fiz. zhurnal, 10(2), 187 (1965).
9. Vilesov, F. I., PTE, 4, 89 (1958)
10. Franklin, S. G., JOSA, 44, 348 (1954).
11. Hartman, P. L., and Nelson, J. R., JOSA, 47, 646 (1957).
12. Hartman, P. L., JOSA, 51, 113 (1961).
13. Rendina, I. F., Rev. Sci. Instr., 7(89), 34 (1963).
14. Shchishatskaya, L. P., Optiko-mekhanicheskaya promyshlennost', No. 12, 33 (1964).
15. Gerasimova, N. G. et al., OMP, 34(7), (1964).
16. Warneck, P., Appl. Opt., 1(6), 721 (1962).
17. Dicke, G. H., and Cunningham, S. P., JOSA, 42, 187 (1952).
18. Cowling, I. E. et al., First Symposium on Surface Effects on Spacecraft Materials -- Palo Alto, California, May 1959, p. 364.
19. Verkin, B. I. et al., Sb. trudov FTINT AN USSR (Collection of Works of the FTINT [transliterated] of the Ukrainian SSR Academy of Sciences), No. 4, 116 (1968).
20. Babjak, S. I., Boobel, C. P., and Scaunapieco, I. F., Vacuum, 18(2), 57 (1968).

21. Kozeyanin, V. V., and Denisov, Yu. N., Sb. trudov NIIYaF  
(Collection of Works of the Scientific Research Institute  
of Nuclear Physics of Moscow State University), 2, Part I,  
1968, p. 358.
22. Huffman, R. E., Larrabee, I. C., and Tanaka, Y., Appl. Optics,  
4, 1581 (1965).
23. Wilkinson, P. G., Canad. J. Phys., 45, 1715 (1967).
24. Huffman, R. E., Tanaka, Y., and Larrabee, J. C., Appl. Optics,  
2, 617 (1963).
25. Zaydel', A. N., and Shreyder, Ye. A., Spektroskopiya vakuum-  
nogo ul'trafioleta (Spectroscopy of the Vacuum Ultraviolet),  
"Nauka", Moscow, 1967 p. 96.
26. Comes, F. I., and Schlag, E. W., Z. Phys. Chem., 21, 212 (1959).
27. Yakovlev, S. A., Optika i spektroskopiya, 14(5), 718 (1963).
28. Feates, F. S., Knight, B., and Richards, E. W. T., Spectro-  
chim. Acta, 18, 485 (1962).
29. Lenson, C. A., and Libby, W. F., Phys. Rev., 135, 1247A (1965).
30. Lelikoff, M. et al., JOSA, 42, 818 (1952).
31. Schlag, E. M., and Comes, F. I., JOSA, 50, 866 (1960).
32. Axelrod, N. N., JOSA, 50, 866 (1960).
33. Okabe, H., JOSA, 54, 478 (1964).
34. Sparapany, I. I., Appl. Optics, 4, 303 (1965).
35. Stief, L. I., and Mataloni, R. I., ibid, 4, 1674 (1965).
36. Fuchsfield, F. C., Evenson, K. M., and Broida, H. P., Rev.  
Scient. Inst., 36, 294 (1965).
37. Verkin, B. I. et al., Doklad na seminar (Paper at Seminar...)
38. Madden R. P., and Hass, G., JOSA, 53, 5 (1963).
39. Lyulichev, A. N., Fugol', I. Ya., and Khrushch, B. I., Sb.  
trudov FTINT AN USSR, No. 5, 1969, p. 83.

40. Kirichenko, A. P., and Krasnova, N. I., ibid, No. 1, 1969, p. 202.
41. Lyman, T., Astrophys. J., 60, 1 (1924); Science, 64, 89 (1926).
42. Collins, G., and Price, W. C., Rev. Sci. Instr., 5, 423 (1934).
43. Worley, R. E., ibid, 13, 67 (1942).
44. Anderson, I. A., Astrophys. J., 75, 394 (1932). /80
45. Unzol'd, A., Fizika zvezdnykh atmosfer (Physics of Stellar Atmospheres), IL, 1949, p. 128.
46. Garton, W. R. S., Proc. 5th Internat. Conf. Ioniz. Phenomena in Gases, Munich, 1961, p. 1884.
47. Goldstein, R., and Mastrup, F. N., JOSA, 765 (1966).
48. Kulikov, S. A. et al., OMP, No. 2, 26 (1965).
49. Samson, A. R., Techniques of VUS, New York.
50. Hunter, W. R., Proc. 10th Colloquium Spectrosc. Intern., 1962, p. 247.
51. Lee, Po, JOSA, 55, 783 (1965).
52. Brmisch, R., and Schonheit, E. Z. Naturforsch., 20a, 611 (1965).
53. Rustgi, O. P., JOSA, 55, 630 (1965).
54. Kulikov, S. A. et al., PTE, No. 2, 157 (1965).
55. Startsev, G. P., Optiko-mekhanicheskaya promyshlennost', 12, 39 (1968).
56. Verkin, B. I. et al., Otchet K-51 a (K-25-1), FTINT of the Ukrainian SSR Academy of Sciences.
57. Ivanenko, D. D., and Pomeranchuk, I. Ya., DAN SSSR, 44, 343 (1944).
58. Schwinger, I., Phys. Rev., 75, 1912 (1949).
59. Tombouljian, D. H., and Hartman, P. L., Phys. Rev., 102, 1423 (1956).
60. Haensel, R., and Kunz, C., Z. fur Angewandte Physik., 23, 276 (1967).



61. Codling, K., and Madden, R. P., J. Appl. Phys., 36, 380 (1965).
62. Godvin, R., UFN, 101(3), 493 (1970).
63. Mullikan R. A., and Sawyer, R. A., Phys. Rev., 12, 167 (1918).
64. Vodar, B., and Astoin, N., Natura, 166, 1029 (1950).
65. Romaud, I., and Balloffet, G., J. Phys. Radium, 166, 489 (1955); Compt. Rend., 244, 739 (1957).
66. Romaud, I., J. Quant. Spectr. Rad. Trans., 2, 691 (1962).
67. Freeman, G. H. C., Proc. Phys. Soc., 86, 117 (1965).
68. Balloffet, G., Ann. Phys., 5, 1243 (1960); J. Phys., 25, 73A (1964).
69. Damany, H., Roncin, I-Y., Damany - Astoin, N., Appl. Optics, 5, 297 (1966).
70. Verkhovtseva, E. T. et al., Zhurn. prikl. spektroskopii, 7(6), (1967).
71. Verkhovtseva, E. T., Fogel', Ya. M., and Osyka, V. S., Optika i spektroskopiya, 25(4), 440 (1968).
72. Verkhovtseva, E. T., et al., Kosmicheskiye issledovaniya, 8(1), 140 (1970).

N 74-28263

METHOD OF CALCULATING GAS-DYNAMICS AND HEAT TRANSFER IN SINGLE-STAGE REFRIGERATION UNITS

/80

I.S. Zhitomirskiy, A.B. Podol'skiy

1. Many of the instruments which are used or can be used in systems of navigation, communications and so on, in flight, and especially spacecraft require the removal of heat given off at a lower temperature level for normal functioning. Accordingly, it becomes necessary to have high-efficiency refrigeration units with small size, low weight and low power consumption.

One of the most promising units for this field of application is represented by refrigerators with internal regeneration of heat. The rational selection of the design parameters of refrigerators can be done only when an adequately supported method of calculating thermal and gas-dynamics processes in these units is available.

In developing methods of a priori estimates of refrigerator characteristics, two directions are possible. The first of these provides for determining cold productivity based on some function obtained for an idealized cycle, followed by correction of this value by the amount of the losses in different unit components. Here the losses are determined either in a differentiated way [16, 23, 24], or else in a generalized manner [1]. The common disadvantage of the first approach is that considerable difficulties arise in designing the units that differ widely from those for which extensive experimental material has been collected and, possibly, a fairly exact determination of losses has been made. The second trend in improvement of methods of analyzing refrigerators is the development of mathematical models of the working process, permitting the tracing of change in working parameters (pressure, velocity, and mass of gas, and gas and wall temperatures) during the cycle [1, 2, 4, 5, 9-12, 17-20, 22].

/81

Sometimes both methods of determining the thermodynamic characteristics of facilities closely overlap and supplement each other. At the same time, there are studies in which the first or second trend is strongly evident, and therefore this classification appears justified.

Thermal and gas-dynamic processes in refrigerators with internal regeneration of heat are marked by great complexity. The duration of the working cycle in the machines is  $(10^{-2} - 1)$  sec. Thus, all these processes are essentially nonsteady. As the result of the intense heat transfer of the working body with the regenerator packing and with the ambient medium, in regenerative heat-exchangers, significant longitudinal gradients in temperature arise, and thus

also in the working body flow rate. All these circumstances produce some difficulties in the theoretical analysis of the working process.

Let us examine existing methods of calculating refrigeration machines with internal regeneration of heat. The studies [9, 23, 24] assumed the isothermality of processes of compression and expansion, ideal heat transfer in recuperative heat-exchangers and in the regenerator, while the effect of the line on processes in the chambers is allowed for in an approximate way. Hydraulic losses in the equipment are not considered. The assumption of the isothermality of processes in machine chambers is also quite approximate.

The studies [1, 2, 4, 5, 10-12, 17-20] make allowance for the nonsteady nature of processes in chambers; they provide for various methods of determining the energy interaction between chambers and the main line. The operation of the heat-exchanger is assumed to be ideal, and the temperature in the heat exchangers and the regenerator is taken to be unchanged during the working process. The volume flow of gas through the main line is determined from the equation of state for the entire mass of the gas in the machine, given the condition of ideal heat transfer in the main line and the absence of hydraulic losses in equipment components.

Methods of calculating a "pulsating tube" refrigerator have been suggested in [18, 19, 20]. It is assumed in [19] that particles of gas in the compression chamber undergo an adiabatic process, that the temperature of the gas in the heat exchangers is constant, and that heat transfer in the regenerator is ideal. The work [20] assumes a constant gas temperature and packing temperature in any cross-section of the regenerator and the gas pressure is assumed to be a linear function of time. Equations are derived for the mean-cyclic wall temperature and mean mass flow rate over the half-cycle in the regenerator and in the pulsating tube.

One of the most exact is the method of calculating refrigerators operating in the Stirling cycle. Processes of heat transfer in chambers are described here with a system of ordinary differential equations or volume-averaged thermodynamic parameters. Heat transfer with walls, energy exchange with the main line, change in the size of the chamber, and the thermal conductivity in the walls are taken into account. To describe the change in thermodynamic parameters in the main line, the author uses differential equations in partial derivatives: the equation of energy in the gas flow and the equation of continuity (the latter is replaced by a finite-difference equation). Instead of the equation of motion, use is made of a modified Darcy-Weissback equation, which is equivalent to neglecting inertial forces in the gas flow. This assumption, when there is an abrupt change in the gas flow rate in the refrigerator, can lead to appreciable deviations from the actual process. A method of solution of the mathematical problem formulated is not set forth in [22].



refrigeration cycles. Actually, the regenerator is a mandatory component of any existing or possible machine, while the compressed-gas motor may or may not be (pulsating tube). The regenerator -- a cylindrical tube with packing -- in the general case is part of the gas-dynamic main line which connects the expansion and compression chambers, and one end of the main line can be closed (pulsating tube).

The gas regenerative refrigerators analyzed are shown in Fig. 1. The parameters of the gas (pressure and temperature) in the low pressure receiver (LPR) and the high pressure receiver (HPR) can be regarded as constant, since the volume of the receivers is large compared with the volume of the refrigerating part of the machines considered. Therefore, there is no need to analyze the chain receiver-compressor (C)-refrigerator (R), and it also appears possible to develop a generalized working scheme for all machines considered. /83

The working scheme (Fig. 2 a) is a system consisting of two chambers  $V_1$  and  $V_2$ , arbitrary in shape and variable in volume, and a main line<sup>1</sup> connecting these chambers. In the general case, the main line consists of a series-connected refrigerator, regenerator (R), and heater (H). During the working process, the gas passes through the trunk line from one chamber to another. In the main line the streaming gas exchanges its heat with the regenerator packing or through the line wall with the ambient environment. Streaming of the gas is caused by the change in the volumes of the chambers (cylinder with piston) or else by connection of the chamber with the high or low pressure receiver.

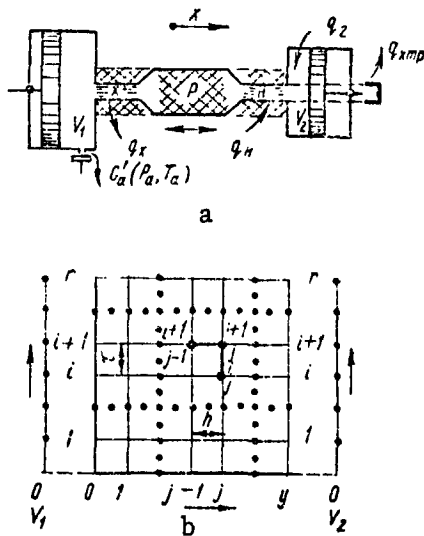


Fig. 2. Working Scheme  
a. Generalized working scheme; b. Difference scheme.

The generalized working scheme (Fig. 2 a), externally similar to the classical scheme of the Stirling cycle, includes several cycles appearing later, namely: MacMahon, Gifford-MacMahon and two modifications of the "pulsating tube". These cycles can be realized in two types of designs: with generator removed and with generator built in. In the second case, the gas-dynamic line is a regenerator connecting the vessels  $V_1$  and  $V_2$ . Here it is assumed that the displacer with the built-in regenerator is fixed, but the cylinder moves, which causes the change in the volumes of vessels  $V_1$  and  $V_2$ . This assumption is quite valid, since the acceleration in the gas stream as a rule is incommensurably greater than the piston acceleration.

Thus, the generalized working scheme is suitable for calculating thermal and gas-dynamic parameters in the working process of gas regenerative refrigerators operating: a) in the Stirling cycle ( $V_1$  is the compressor and  $V_2$  is the compressed-gas motor); b) in the MacMahon cycle ( $V_1$  is the valve chamber or a chamber whose volume is equivalent to the overall volume of the system of subsidiary flow lines supplying gas from the receiver, and  $V_2$  is the compressed-gas motor); c) in the Gifford-MacMahon cycle with built-in regenerator ( $V_1$  and  $V_2$  are the hot and cold parts of the working cylinder, respectively, separated by the regenerator placed in it); d) in the cycle of the "pulsating tube" with the generator removed (the volume  $V_2$  disappears).

3. Proceeding to outline our proposed method of calculation, let us first formulate these assumptions made above:

a) heat transfer by thermal conductivity in the gas and the walls of the lines is negligibly small compared with convective heat transfer;

b) thermal conductivity of the packing is equal to zero in the gas flow and is infinitely large along a normal to it;

c) the working gas obeys the equation of state for an ideal gas: the specific heat capacity of the gas is constant;

d) in the chambers analyzed the ratio of the diameter of the inlet opening to the characteristic dimension of the chamber is small. Therefore the nonuniformity of the distribution of pressure caused by the wave phenomena in the chamber during streaming or filling is negligibly small [21];

e) the equalizing of the temperature of the gas in the chamber as the result of mixing of the incoming gas portion with the earlier present gas portion occurs in a time interval much smaller than the time of an appreciable change in thermodynamic parameters of the gas in the chamber. /84

These last two assumptions make it possible to assume that the processes in the chambers can be described with a system of ordinary differential equations for semidynamic parameters averaged over the chamber volume.

In the last equations, the gas consumption is assumed to be positive when gas flows into the chamber and negative when it flows out of the chamber. The subscript  $n$ , taking on the values 1 and 2, denotes the number of the chamber, and the subscript  $\epsilon$  denotes the number of the source or discharge of the gas for the given chamber. The role of these sources and discharges is played either by the high or low pressure receivers, or by the main line connecting the chambers. The main equations of balance for the chambers are as follows:

the equation of energy for the gas is

$$\frac{d}{dt}(m_n e_n) = -P_n \frac{dV_n}{dt} + \sum_i G_{en} I_{en} + q_n - F_n \cdot \alpha_n (T_n - T_{cn}) \quad (1)$$

the quantities  $I_n$  are determined by the parameters of the gas in the chamber when  $G_{en} < 0$  and by the parameters of the source when  $G_{en} > 0$ ;

the equation of heat balance for the wall (subscript  $c$ ) is

$$\rho_{cn} \delta_{cn} \frac{de_{cn}}{dt} = \alpha_n (T_n - T_{cn}) + \alpha_{an} (T_{an} - T_{cn}) + q_{cn}; \quad (2)$$

change of mass of gas in chamber

$$\frac{dm_n}{dt} = \sum_i G_{en}; \quad (3)$$

equation of state:

$$P_n V_n = m_n R I_n; \quad (4)$$

change in volume of chamber with time:

$$V_n = V_n(t); \quad (5)$$

change in valve cross-sectional area with time:

$$f_n = f_n(t). \quad (6)$$

Here  $m$  is the mass of gas;  $e$  is internal energy;  $P$  is pressure;  $V$  is volume;  $G$  is gas consumption;  $I$  is enthalpy;  $q$  is the density of the thermal flux;  $\alpha$  is the coefficient of heat transfer;  $T$  is gas temperature;  $T_w$  is wall temperature;  $\delta_w$  is wall thickness;  $a$  is the index of the ambient environment.

When gas arrives from the external reservoir, the energy transfer  $G_{en} I_{en}$  is determined from the condition of the quasisteady-state nature of the gas outflow process. To determine the gas consumption  $G_{en}$ , we use expressions obtained for the single-dimensional isentropic outflow of gas in [7].

The time interval during which cyclic change in thermal and gas-dynamic parameters occurs in refrigerators is  $(1 - 10^{-3})$  sec, where the smallest characteristic linear dimension is of the order of  $0.3 \cdot 10^{-4}$  m (the pores in the regenerator packings). Since the time and spatial scales of these processes are large compared with the relaxation time and with the mean free path of molecules in the gas, heat-transfer and gas-dynamic processes in the main line in the case of a smooth variation in the cross-sectional area,

are satisfactorily described with a system of one-dimensional differential equations in partial derivatives for parameters averaged over the flow cross-section.

The equation of motion is:

/85

$$\rho \frac{du}{dt} = - \frac{\partial p}{\partial x} - \frac{\xi}{2d_r} \rho u |u|; \quad (7)$$

the equation of continuity is:

$$\frac{\partial \rho}{\partial t} + \frac{\partial}{\partial x} (\rho u) + \rho u \frac{\partial}{\partial x} \ln F = 0; \quad (8)$$

the equation of energy in the gas flow:

$$\rho \frac{di}{dt} = \frac{dp}{dt} - \frac{4\alpha}{d_r} \left( T - T_c + \frac{u^2}{2c_p} \right) + \frac{\xi}{2d_r} \rho U^2 |U|; \quad (9)$$

the equation of heat balance for the wall (packing) is:

$$\rho_c \frac{\partial T_c}{\partial t} = S \cdot \left( T - T_c + \frac{u^2}{2c_p} \right) + W(T_s - T_c) + q_c, \quad (10)$$

where

$$\begin{aligned} S &= \frac{\alpha}{\delta_s}; \quad W = \frac{\alpha_s}{\delta_s} \quad \text{-- for the wall} \\ S &= \frac{4\alpha}{c_r} \cdot \frac{\rho}{1-p}; \quad W = 0 \quad \text{-- for packing,} \end{aligned}$$

(p -- is porosity);

and the equation of state is:

$$\begin{aligned} p &= \rho RT; \\ t &\geq 0; \quad 0 \leq x \leq l. \end{aligned} \quad (11)$$

Here  $u$  is velocity;  $\rho$  is density of gas;  $d_2$  is hydraulic diameter;  $F$  is the area of the flow kinetic cross-section; and  $l$  is the length of the main line.

The coefficients of heat transfer  $\alpha_n$ ,  $\alpha_{an}$ , and  $\alpha$ , and the coefficient of hydraulic drag  $\xi$  are selected from experimental data. The heat transfer and gas-dynamic processes are strongly affected by the dependence of the physical properties of the gas and the packing on temperature (in particular, this is shown in [13] for the regenerator). Therefore, to the system of equations shown above we must add the temperature functions of those heat-physical characteristics that undergo considerable change in the temperature range under study.

As the initial conditions, the arbitrary distribution of temperature, pressure, velocity, gas mass, and temperature of wall in chambers and in their connecting main line are adopted:



$$\begin{aligned} P_n(0) = P_n^0; \quad T_n(0) = T_n^0; \quad T_{cn}(0) = T_{cn}^0; \quad m_n(0) = m_n^0; \quad V_n(0) = V_n^0; \\ P(0, x) = P_0(x); \quad T(0, x) = T_0(x); \quad T_c(0, x) = T_{ce}(x); \quad U(0, x) = U_0(x). \end{aligned} \quad (12)$$

The system of equations (7) -- (11) is hyperbolic in character and has four families of characteristics  $dx/dt = u$ ,  $dx/dt = u + a$ ,  $dx/dt = 0$ . The behavior of these characteristics makes it necessary to assign two boundary conditions at the inlet into the main line and one -- at the outlet [15]. This specifying of boundary conditions in our case does not appear possible, but we can specify systems of conditions of connecting chambers with the main line that are equivalent to it. Here the number of conditions of connection at the inlet and outlet from the main line must correspond to the required number of boundary conditions.

Thus, for subsonic gas flows at the inlet into the main line two conditions of connection are used ( $u, a$ , where  $a$  is the speed of sound in gas):

$$\begin{aligned} P_n = P_0 + \zeta_0 \rho_0 u_0^2 \quad \text{-- is the conservation of momentum,} \\ \frac{2k}{k-1} R T_n = \frac{2k}{k-1} R T_0 + u_0^2 \quad \text{-- is the conservation of energy} \end{aligned} \quad (13)$$

( $k$  is the adiabatic index).

At the outlet from the main line, the condition of connection is taken as the law of the conservation of momentum (the pressure of the gas in the jet entering the chamber and the pressure of the gas inside the chamber are similar, owing to assumption 4; we cannot make an analogous conclusion concerning gas temperature, therefore the law of conservation of energy is not usefully employed here):

$$P_n = P_y + \frac{F_y}{F_n} \zeta_y \rho_y u_y^2. \quad (14)$$

If instead of the outlet there is a dead-end wall (the dashed line in Fig. 2), a condition is required which, in this case, is the boundary condition ( $u = 0$ ).

4. This system of differential equations and boundary conditions (1) - (14), describing the change in thermo-gas-dynamic parameters when gas flows between communicating vessels is solved by the finite-difference method.

According to the adopted implicit difference scheme (Fig. 2 b), after several translations of the initial equations, the following difference equations are obtained:

$$\begin{aligned} \frac{T_n^{i+1} - T_n^i}{\tau} = -(k-1) T_n^{i+1} A_1 + \frac{1}{m_n^i} \Sigma G_{cn}^{i+1} [k (T_{cn}^*)^i - T_n] - \\ - A_2 \frac{V_n^i}{m_n^i} T_n^{i+1} + A_2 \frac{V_n^i}{m_n^i} T_{cn}^i + \frac{q_n}{c_v} \frac{1}{m_n^i}, \\ \frac{P_n^{i+1} - P_n^i}{\tau} = -k P_n^{i+1} A_1 + \frac{R}{V_n^i} \Sigma G_{cn}^{i+1} k (T_{cn}^*)^i - A_2 \frac{V_n^i}{m_n^i} P_n^{i+1} + \end{aligned} \quad (15)$$

$$+ A_2 R T_{cn}^i + \frac{q_n}{c_v} \frac{R}{V_n^i}; \quad (16)$$

$$\frac{m_n^{i+1} - m_n^i}{\tau} = \Sigma G_{en}^{i+1} \beta; \quad (17)$$

$$\frac{T_{cn}^{i+1} - T_{cn}^i}{\tau} = \frac{1}{\rho_{cn} \delta_{cn} c_{cn}} [\alpha_n (T_n^{i+1} - T_{cn}^{i+1}) + \alpha_{an} (T_{an}^{i+1} - T_{cn}^{i+1}) + q_{cn}], \quad (18)$$

where

$$A_1 = (V_n^{i+1}/V_n^i - 1)/\tau; \quad A_2 = \alpha_n \frac{4}{d_n \cdot c_v}.$$

$$G_{en}^{i+1} = \begin{cases} G_{pn}^{i+1} & \text{-- for the case of energy exchange with} \\ & \text{the receiver and} \\ u_z^{i+1} \rho_z^i F_z & \text{leaking of gas through the piston seal,} \\ & \text{-- energy exchange with the main line.} \end{cases}$$

When the chamber is being filled:

$$(T_{en}^*)^i = \begin{cases} T_{pn} & \beta = 1 \text{ -- energy exchange with the receiver or} \\ & \text{or gas leak} \\ T_z + \frac{(u_z^{i+1})^2}{2c_p} & \text{-- energy exchange with the main} \\ & \text{line.} \end{cases}$$

During emptying of the chamber, we have:

$$\beta = \begin{cases} \frac{m_n^{i+1}}{m_n^i} & \text{-- outflow into the receiver or leakage,} \\ 1 & \text{-- outflow into the main line} \end{cases}$$

$$(T_{en}^*)^i = T_n^i.$$

Gas consumption. G is determined according to [7]:

$$\frac{u_j^{i+1} - u_j^i}{\tau} + u_j^i \frac{u_j^{i+1} - u_j^{i-1}}{h} + R \frac{T_j^i}{P_j^i} \frac{P_j^{i+1} - P_j^{i-1}}{h} = - \frac{1}{2a_2} u_j^{i+1} |u_j^i|, \quad (19)$$

/87

$$\left. \begin{aligned} & \frac{P_j^{t+1} - P_j^t}{\tau} + u_j^t \frac{P_j^{t+1} - P_{j-1}^{t+1}}{h} - \frac{P_j^t}{T_j^t} \left( \frac{T_j^{t+1} - T_j^t}{\tau} + u_j^t \frac{T_j^{t+1} - T_{j-1}^{t+1}}{h} \right) + \\ & + P_j^t \frac{u_j^{t+1} - u_{j-1}^{t+1}}{h} = - \frac{B_1 \cdot B_2}{h} P_j^t, \end{aligned} \right\} \quad (20)$$

where  $B_1 = u_j^1 + 1$  for  $B_2 > 0$  and  $B_1 = u_j^1 - 1$  for  $B_2 < 0$ ,  $B_2 =$

$$\left. \begin{aligned} & \frac{T_j^{t+1} - T_j^t}{\tau} + u_j^t \frac{T_j^{t+1} - T_{j-1}^{t+1}}{h} - \frac{k-1}{k} \frac{T_j^t}{P_j^t} \left( \frac{P_j^{t+1} - P_j^t}{\tau} + u_j^t \frac{P_j^{t+1} - P_{j-1}^{t+1}}{h} \right) = \\ & = - \frac{4\alpha}{d_r} \frac{k-1}{k} \frac{T_j^t}{P_j^t} \{ T_j^{t+1} - T_{cj}^t + (u_j^t)^2 / 2c_p \} + \frac{\xi}{2d_r} \frac{1}{c_p} (u_j^t)^2 |u_j^t|, \end{aligned} \right\} \quad (21)$$

$$\frac{T_{cj}^{t+1} - T_{cj}^t}{\tau} = \frac{s}{\rho_c c_c} \left[ T_j^{t+1} - T_{cj}^{t+1} + \frac{(U_j^t)^2}{2c_p} \right] + \frac{W}{\rho_c c_c} (T_a^t - T_{cj}^{t+1}) + q_c. \quad (22)$$

The conditions of connection are:

$$\left. \begin{aligned} P_n^{t+1} &= P_0^{t+1} + \zeta_0 \rho_0^t \cdot (u_0^{t+1})^2, \\ \frac{2k}{k-1} R T_n^{t+1} &= \frac{2\lambda}{k-1} R T_0^{t+1} + (u_0^{t+1})^2, \end{aligned} \right\} \quad (23)$$

$$P_n^{t+1} = P_y^{t+1} + \frac{F_p}{F_n} \zeta_p \rho_p^t (u_y^{t+1})^2. \quad (24)$$

The system of difference equations (19) - (21) is solved by the method of orthogonal fitting [3]. For this purpose, equations (19) - (21) are written as

$$A_{ij}^t x_{j-1}^{t+1} + B_{ij}^t x_j^{t+1} = C_i^t, \quad (25)$$

where  $A_j^1$ ,  $B_j^1$  -- are square matrices of coefficients for the known time layer,

$x = \begin{pmatrix} U \\ P \\ T \end{pmatrix}$  -- is a vector, whose components are the unknown thermo-gas-dynamic parameters in the main line.

The conditions of connection can be represented as

$$\left. \begin{aligned} L_{yz}^{i,i+1} &= \varphi, \\ N_{yz}^{i,i+1} &= \psi, \end{aligned} \right\} \quad (26)$$

where  $L_0^1$ ,  $N_0^1$  are rectangular matrices that are formed from equations (23) and (24), respectively, by cancelling out  $p_n^1 + 1$  and  $T_n^1 + 1$  with the aid of equations (15) and (16) and by subsequent linearization in velocity ( $u^{i+1} = u^i + \Delta u^i$ ). Further, the procedure in calculating the thermo-gas-dynamic parameters in the main line is set up in accordance with the procedure described in [3].

That the determination of  $u_j^1 + 1$ ,  $p_j^1 + 1$ , and  $T_j^1 + 1$  in the gas-dynamic main line from known values  $j$  of the gas outflow velocity  $u_0^1 + 1$  and  $u_j^1 + 1$ , we find the thermo-gas-dynamic parameters in the vessels according to the equations (15 and (17)). When calculating the emptying of the main line closed at one end ("pulsating tube"), it appears necessary to have an auxiliary equation (in addition to the available equation  $u = 0$ ) in accordance with (26). We can adopt as this expression the characteristic equation /88 corresponding to the characteristic  $dx/dt = u$ , which when  $u = 0$ , is of the form

$$\frac{T_0^{i+1} - T_0^i}{\tau} - \frac{k-1}{k} \frac{T_0^i}{P_0^i} \frac{P_0^{i+1} - P_0^i}{\tau} = - \frac{4\alpha}{d_r} \frac{k-1}{k} \frac{T_0^i}{P_0^i} (T_0^{i+1} - T_{co}^i). \quad (27)$$

The wall temperature in the vessel  $T_{wn}^1 + 1$  and the temperature of the wall in the main line  $T_{w1}^1 + 1$  are determined, respectively, from Eqs. (18) and (22). Thus, for the new time layer,  $i + 1$ , all the thermo-gas-dynamic parameters in the chambers and their connecting main line have been determined.

The program for calculating these parameters has been developed in the algorithmic language ALGO-60.

Preliminary estimates and calculations performed with the M-20 digital computer showed that this finite-difference method of solving the initial equations has a first order of approximation in time and space. The length of the step in time must be approximately 0.003-0.001 of the overall cycle duration. The length of the step in space must be approximately 0.03-0.01 of the total length of the main line; the sites of connection of the component must be calculated with a shorter step, whose value is determined in relation to the ratio of the diameters of the components being connected.

5. For a system modeling the working process in the refrigerators of Stirling, MacMahon, Gifford-MacMahon, and pulsating tube, calculations of heat transfer and gas-dynamic parameters in the initial working cycle were made on a digital computer. The results of these calculations are given in [14].

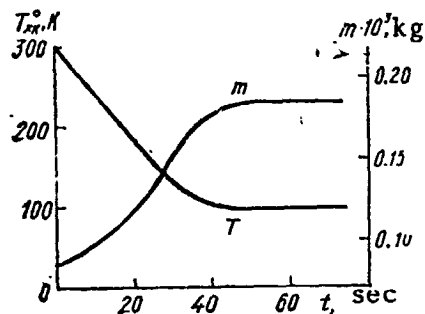


Fig. 3. Change in packing temperature at cold end of regenerator (T) and mass of gas in compressed-gas motor (M) at end of working cycle when the machine departs from regime.

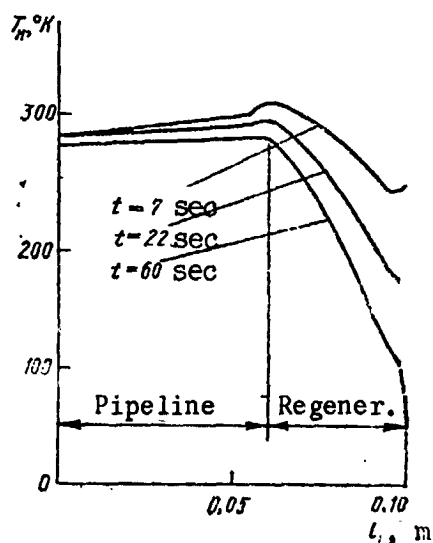


Fig. 4. Distribution of packing temperature along regenerator length at end of working cycle when machine departs from regime.

The developed method of calculation makes it possible to analyze the characteristics of the machine in the transitory process, that is, when the machine departs from the regime. This calculation was performed for a refrigerator operating in the MacMahon cycle (compressed-gas motor with regenerator in the dead space). In the calculation, the following geometrical and heat-physical data were adopted: cylinder diameter -- 40 mm, piston stroke -- 40 mm, wall thickness -- 0.5 mm, revolutions per minute -- 250, regenerator diameter -- 15 mm, regenerator length -- 40 mm, mesh size -- 004, porosity -- 0.7, initial packing (wall) temperature and initial gas temperature --  $300^\circ K$ , maximum gas pressure --  $20 \cdot 10^5 N/m^2$ , minimum gas pressure --  $5 \cdot 10^5 N/m^2$ , working gas -- helium, law of compressed-gas motor piston travel -- harmonic,  $\alpha_0 = 3000 W/m^2 \cdot deg$ ,  $\zeta_p = 2$ , cold productivity -- 5 watts,  $\alpha_n = 2000 W/m^2 \cdot deg$ .

The arbitrary distribution of parameters characterizing the non-working state of the machine was taken as the initial conditions. The results of the calculation of the transitory process are in Figs. 3-6. /89

When the machine departs from the regime, the temperature at the cold end of the packing (see Fig. 3) varies exponentially, and in the  $300-150^\circ K$  range, the drop in temperature can be taken as approximately linear. The temperature at the cold end was of the order of  $97^\circ K$  in 70 sec. This rapid departure from the regime is caused by the fact that in the calculation no allowance was made for the mass of certain auxiliary machine components that are usually situated in the cold zone (the mass of the object being chilled, and so on), and the rate of departure from the regime was determined by the

rate of cooling of the regenerator packing. When the additional masses are taken into account, the time of departure from the regime increases somewhat.

Fig. 4 shows the distribution of the packing temperature along the regenerator length at the end of the working cycle. The change in the packing temperature, as we can see from the plot, can be assumed approximately linear. Fig. 5 shows the calculated indicator diagram for the initial working cycle (dashed line) and for the working cycle in the steady regime (shaded diagram). The difference in the diagram from the usually accepted shape (the absence of the section of reverse compression) is caused by the fact that in the calculation it was assumed that the exhaust valve remains open during the entire reverse stroke of the compressed-gas motor piston.

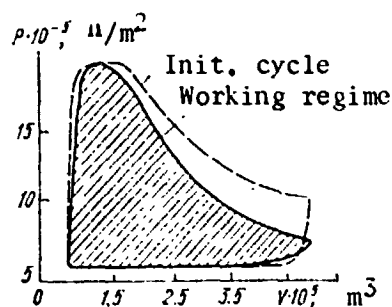


Fig. 5. Calculated indicator diagram of MacMahon refrigerator.

The change of pressure and temperature of the gas in the compressed-gas motor in the working cycle in the steady regime is shown in Fig. 6.

The proposed single-dimensional mathematical model of nonsteady heat-transfer and gas-dynamic processes in refrigerators takes into account thermal and hydraulic losses, and the variability of the heat-physical characteristics of the interacting bodies. The finite-difference method of solving the initial system of equations developed here permits calculating the change in thermodynamic parameters in the working cycle in the transitory and steady regimes and determining the time for the machine's departure from the regime.

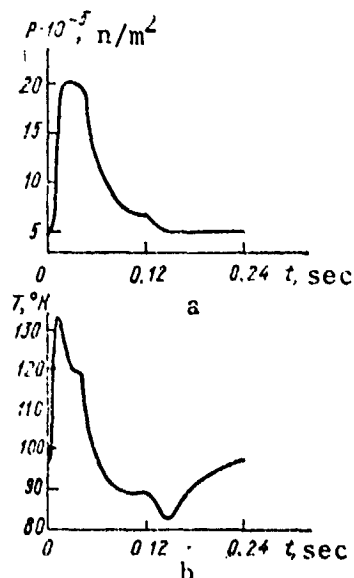


Fig. 6. Change in parameter of gas in compressed-gas motor in the working cycle of the machine in the steady regime.  
a. pressure; b. temperature

# REFERENCES

1. Arkharov, A. M., Nizkotemperaturnyye gazovyye mashiny (Low-Temperature Gas Machines), "Mashinostroyeniye", 1969.
2. Brodyanskiy, V. M., and Grachev, A. B., Izv. vuzov, Energetika, No. 7, (1965)
3. Godunov, S. K., ZhVM i MF, 2(6), (1962).
4. Karavanskiy, I. I., Tezisy dokladov Vsesoyuzn. konf. Odessa (Abstracts of Papers Presented at the All-Union Conference at Odessa), 1967.
5. Kuznetsov, B. G., and Arkharov, A. M., Trudy MVTU im. Baumana (Transactions of the Moscow High-Technical Schools im. Bauman), No. 138, (1970). /90
6. Kutateladze, S. S., and Borishanskiy, V. M., Spravochnik po teploperedache (Handbook on Heat Transfer), Gosenergoizdat, 1959.
7. Loytsyanskiy, L. G., Mekhanika zhidkosti i gaza (Mechanics of Liquids and Gases), 1970.
8. Malkov, M. P., et al., Spravochnik po fiz.-tekhn. osnovam glubokogo okhlazhdeniya (Handbook on Engineering Physics Fundamentals of Deep Cooling), Gosenergoizdat, 1963.
9. Mel'tser, L. Z., and Karavanskiy, I. I., Kholod'linaya tekhnika, No. 5, (1959).
10. Mikulin, Ye. I., Kriogennaya tekhnika (Cryogenic Techniques), "Mashinostroyeniye", 1969.
11. Mikulin, Ye. I., Gorshkov, A. M., and Danilenko, T. K., Trudy MVTU im. Baumana, No. 132, (1969).
12. Novotel'nov, V. N., and Kondryakov, I. K., Khimicheskoye i neftyanoye mashinostroyeniye, No. 7, (1969).
13. Podol'skiy, A. G., IPZh, 19(2), (1970).
14. Podol'skiy, A. G., Trudy FTINT AN USSR (Transactions of the FTINT [transliterated] of Ukrainian SSR Academy of Sciences), No. 1, (1970).

15. Rozhdestvenskiy, B. L., and Yanenko, N. N., Sistemy kvazilinyeynykh uravneniy (Systems of Quasilinear Equations), "Nauka", 1969.
16. Suslov, A. D., Uzv. vuzov, Mashinostroyeniye, No. 5, (1970).
17. Suslov, A. D., and Sivkov, V. P., Trudy MVTU im. Baumana, No. 132, (1969).
18. Suslov, A. D., and Ruban, A. N., *ibid*, No. 138, (1970).
19. Shnayd, I. M., and Pavlovskiy, A. L., Trudy Vsesoyuzn. nauchno-tekhn. konf. po termodinamike (Transactions of the All-Union Scientific-Technical Conference on Thermodynamics), Leningrad, 1967.
20. Collangelo, I. W., and Fitzpatrick, F. E., Adv. in Cryog. Engrg., No. 13, (1968).
21. Decker, B. E., and Chang, V., Tr. ASME, No. 3, (1968).
22. Finkelstein, T., Journ. of Spacecraft and Rockets, No. 9, (1967).
23. Gifford, W. E., Adv. in Cryog. Engrng., No. 11, (1966).
24. Kohler, I. W. L., Progress in Cryogenics, No. 2, (1960).



1174-28284

PROBLEM OF SELECTING OPTIMAL REGIMES FOR STORAGE OF CRYOGENIC AGENTS /90

R. S. Mikhal'chenko, V. F. Getmanets, and Yu. V. Iskhakov

Various cryogenic systems onboard spacecraft, such as rocket engines, fuel elements, life support systems, and so on, impose specific requirements both as to the weight reserves of the cryogenic agents as well as storage time [1-3]. However, in all cases the minimum weight requirement remains unchanged. Solving this problem requires not only building reliable thermal-protective devices, but also developing the optimal conditions for the process of storing cryogenic agents in specific conditions of space. The following external conditions have the main effect on the storage process: temperature and pressure of the ambient medium and gravitational acceleration.

The temperature of the outer hull in combination with the heat-protection devices determines the heat inflows to the cryogenic agent. The combined action on the storage regime of these factors, as well as the influence of the storage time and the amount of agent stored can be taken into account in calculations by means of the criterion of specific heat inflows  $Q_T$  during the storage time [4].

In ground conditions, cryogenic agents are most conveniently stored in the liquid state with the draining of vapor formed during storage. In space conditions, this method encounters difficulties owing to the complexity of separating the liquid-vapor mixture in conditions of weightlessness. From this standpoint, preference must be given to storing cryogenic agents in the solid state. The saturated vapor pressures of most cryogenic agents are much lower than atmospheric pressure. The presence of the high space vacuum insures the storage of solidified gases without additional pumping units and energy outlays.

As follows from the analysis given in this study, the storage of cryogenic agents in the solid state with the draining of the vapors formed to the surrounding space not only makes for the practical convenience of the operation, but also permits an appreciable reduction in the losses of the stored substance. Referring to the specific conditions, we perform a thermal analysis of the possible storage regimes in the condensed state of hydrogen, oxygen, nitrogen, and argon. /91

With decrease in the temperatures of cryogenic agents, both the specific density and heat of vaporization increase. Moreover, the possibility of an increase in the cold reserves owing to the heat capacity of the condensed state mounts. At the same time, with decrease in the temperature, the heat inflows to the stored agent show practically no rise when the most effective laminated-vacuum

insulations are used [4-5]. Therefore, losses in vaporization for a particular cryogenic agent are appreciably reduced with decrease in the temperature of the initial state [6]. Accordingly, in our analysis, the temperature of the initial state was taken as equal to the temperature that is the lowest attainable in practical conditions ( $T_{\min}$ ), in the numerical calculations, which corresponds to the saturated vapor pressure over the solidified gas of 0.1 torr [7]. It must be noted that in specifically arranged conditions, the vapor pressure over solid hydrogen can be reduced down to  $1 \cdot 10^{-3}$  torr [8].

The estimation of different storage regimes is possible only by comparing the losses of the substance during the entire storage period. We will estimate the loss by the coefficient of relative losses  $\eta$ , defined by the ratio

$$\eta = \frac{m_0 - m_K}{m_0}, \quad (1)$$

where  $m_K$  characterizes the mass of the agent at the end of the storage, and  $m_0$  is equal to the mass of the solidified gas, which can be charged into the vessel at the temperature  $T_{\min}$ .

This criterion was used also in evaluating the nondrainage storage regime, where, strictly speaking, no losses of substance occur. However, even in this regime there are losses of the substance in the sense that in the initial state, to avoid overly rapid pressure rise when heating, the charging factor of the vessel must be less than 1. In addition, for the nondrainage storage regime, the usually adopted coefficient of relative losses  $\eta = \frac{m_H - m_K}{m_H}$  in general becomes meaningless, since in any case it is 0;  $m_H$  is the initial mass. If by using the ratio

$$\rho_V = \frac{m}{V_c} \quad (2)$$

we introduce the concept of the density of the substance in the vessel averaged over the volume  $\rho_V$ , then by employing  $m_K = \rho_V^K \cdot V_c$  and  $m_0 = \rho_m \cdot V_c$ , Eq. (1) can be represented as:

$$\eta = 1 - \frac{\rho_V^K}{\rho_m}. \quad (3)$$

The mean-volume density at the end of storage  $\rho_V^K$  is defined by the ratio between the heat inflows into the vessel and by the cold reserve in the cryogenic substance;  $\rho_m$  is the maximum possible density of the solidifying gases at the temperature  $T_{\min}$ .

In order to increase the generality of the analysis and to take account of the dependence of losses on various factors (vessel size and shape, storage time, nature of change in heat inflows with time, kind of thermal protection and its design, and so on), we will characterize the heat inflows to the stored substance by the parameter of the specific heat inflows  $Q_T$ , which is

$$Q_T = \frac{1}{V_0} \int_0^{\tau_{xp}} Q d\tau. \quad (4)$$

The parameter  $Q_T$  determines the heat inflows per unit chamber volume during the entire storage time  $\tau_{xp}$ . /92

The thermodynamic analysis of the following storage regimes was carried out in our study:

I. Nondrainage storage regimes with gradual heating of the cryogenic agent partially filling the vessel at the  $T_{min}$  to the temperature  $T_K$  at which the condensed phase fills the entire vessel volume.

II. Nondrainage storage in regime I up to the temperature  $T_K$  and subsequent drainage of the vapors in isothermal conditions.

III. Isothermal storage at the initial temperature  $T_{min}$  with constant drainage of the vapors formed.

IV. Isothermal storage with draining of the vapors at the temperature  $T_{min}$ , further nondrainage heating with temperature rise to  $T_K$  at which the condensed phase, due to thermal expansion, fills the entire chamber volume and again, drainage of vapors in isothermal conditions  $T_K = \text{const.}$  to the end of the storage.

V. Heating of the condensed phase filling the entire vessel volume at all temperatures, from the temperature  $T_{min}$  to  $T_K$ , along the equilibrium line solid (liquid) phase-vapor<sup>min</sup>, with evaporation and drainage of the excess volume of substance arising owing to the thermal expansion of the condensed phase, and subsequent isothermal drainage of the vapors at the temperature  $T_K = \text{const.}$

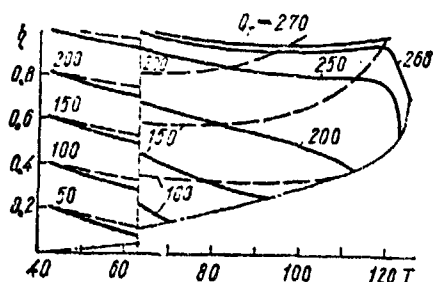


Fig. 1. Dependence of relative losses of hydrogen, oxygen, nitrogen, and argon vapor on the final-state temperature for various specific thermal inflows  $Q_T$  during storage in regimes II and IV ( $T$ ,  $^{\circ}\text{K}$ ;  $Q_T$ ,  $\text{j/cm}^3$ ).

The analysis was made on the assumption that with isobaric drainage of vapors and with heating of condensed phase, its temperature is identical in the entire vessel volume. In the liquid phase, this condition can easily be insured by mixing of the liquid or by placing in the vessel ribs made of a material with high thermal conductivity. If porous solidified gases, (obtained by the evacuation method), are not heated very intensely, their temperature also changes at the same rate throughout the vessel volume [9, 10].

For a maximum use of the useful volume of the vessel, we assume that at the end of the nondrainage storage (regimes I, II, IV), the condensed phase fills the entire vessel volume,

and we take the initial vessel charging factor in regimes III-V as equal to 1.

It can be shown that with the assumptions made in our study, the amount of heat  $Q_V$  absorbed per unit volume of cryogenic agent when it passes in regimes I-IV from the assigned temperature  $T_{\min}$  to  $T_K$  (with or without drainage of vapor) is determined only by the selection of the final-state temperature  $T_K$ . For the period of nondrainage storage (regimes I, II, IV), this assertion is obvious, since in this case the mass of the substance remains unchanged and is determined by its density at  $T_K$ .

The amount of heat absorbed during drainage at  $T_K$  in the regimes II-V is determined by the density of the substance and by the heat of the phase transition, that is, by the temperature  $T_K$ . The amount of vapor drained and the heat inflow during the heating process per unit volume of the substance in the regime V to the temperature  $T_K$  are also determined only by the density of the condensed phase at this temperature. It remains to be noted that the amount of vapor drained in regime IV at the initial temperature  $T_{\min}$  (and therefore, also the energy expended) uniquely determines the temperature  $T_K$  at which the stage of nondrainage storage sets in. Therefore, the selection of the final  $T_K$  uniquely determines in regime IV the charging factor at the end of drainage, for the initial temperature  $T_{\min}$ . Accordingly, all the regimes considered can be characterized by a single-valued function of cold which depends only on the final-state temperature. /93

Let us derive the analytic expressions for the function described.

#### Storage in Regime I

In the conditions of nondrainage storage, the heat inflows to the vessel are absorbed by the heat capacity of the condensed phase and of vapor, and by the heat of vaporization of the portion of the condensed phase which enters the vapor cushion, and with heating above the triple point temperature, the heat of fusion is also used. Therefore the cold reserve of the substance  $Q_V^I$  per unit volume of the vessel extended with heating from  $T_{\min}$  to  $T_K$  is:

$$Q_V^I = \int_{T_{\min}}^{T_K} (\rho_V - \rho_V^n) c_s dT + \int_{T_{\min}}^{T_K} \rho_V^n \cdot c_v^n dT + \int_{T_{\min}}^{T_K} r d\rho_V^n + \left[ F(T_K) = \lambda \cdot (\rho_V - \rho_V^n); \begin{matrix} T_K \geq T_{p,T} \\ 0, T_K < T_{p,T} \end{matrix} \right]. \quad (5)$$

Here  $c_s$  and  $c_v^n$  are, respectively, the heat capacity of the condensed phase and the vapor along the saturation line;  $r$  is the heat of vaporization (sublimation);  $T_{p,T}$  stands for the triple point.

If there is no drainage, the mean-volume density of vessel charging  $\rho_v$  is a constant and is the density of the condensed phase at the end of storage, that is

$$\rho_v = \rho(T_k) = \rho_k. \quad (6)$$

Therefore, Eq. (3) for relative losses for storage in regime I becomes:

$$\eta = 1 - \frac{\rho_k}{\rho_m}. \quad (7)$$

The mean-volume density of the vapor in the vessel  $\rho_v^n = \frac{m_n}{V_c}$  is a function of temperature and the vessel filling factor. Since the last quantity owing to the earlier assumptions, is also a function of the final-state temperature,  $\rho_v^n = \rho_v^n(T_k)$ . Let us determine this dependence. Suppose at an arbitrary moment of time the vapor cushion occupies in the vessel volume the fraction  $x$ , that is,  $x = \frac{V_v^n}{V}$ . Then by using the constancy of the mean-volume density of the substance in the vessel, we can write:

$$x \cdot \rho_n + (1 - x) \rho = \rho_k. \quad (8)$$

Hence we get:

$$x = \frac{\rho - \rho_k}{\rho - \rho_n}. \quad (9)$$

Thus, the mean-volume density of the vapor is

$$\rho_v^n = x \cdot \rho_n = \rho_n \frac{\rho - \rho_k}{\rho - \rho_n}. \quad (10)$$

We can represent this formula also in another form:

$$\rho_v^n = \frac{1}{v_n - v} - \rho_k \frac{v}{v_n - v}, \quad (11)$$

where  $v$  and  $v_n$  are, respectively, the specific volumes of the condensed phase and of the vapor. /94

At the triple point temperature, the mass of the vapor can also be neglected, compared with the mass of the condensate and, we can set:

$$\rho_v^n(T_{min}) \approx 0. \quad (12)$$

Additionally, in Eq. (5) at temperatures below the critical point, we can neglect the expression  $\int_{T_{min}}^{T_k} \rho d\rho_v^n$  owing to its smallness with respect to the other terms. However, in the near-critical region, this expression cannot be neglected; owing to the absence here of data on the heat capacity of cryogenic substances let us use for this region the diagram of state, and we can write the expression for function  $Q_V^I$  as:

$$Q_V^I = \rho \Delta l - \Delta p, \quad (13)$$

where  $\Delta I$  and  $\Delta p$  are the difference in the enthalpies and the pressures, respectively, at temperatures  $T_K$  and  $T_{min}$ .

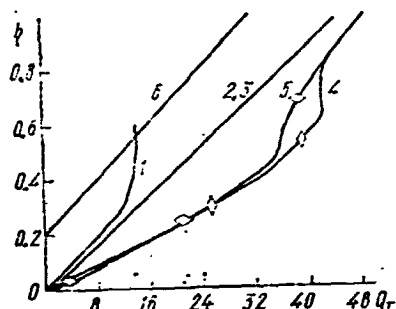


Fig. 2. Dependence of minimum relative losses of hydrogen vapor  $\eta$  on specific heat inflows  $Q_T$  for storage in different regimes ( $Q_T$ , j/cm<sup>3</sup>):

1. Storage in regime I;
2. Regime II; 3. Regime III;
4. Regime IV;
5. Regime V; 6. Storage of liquid boiling at  $P = 1$  ab. atm.

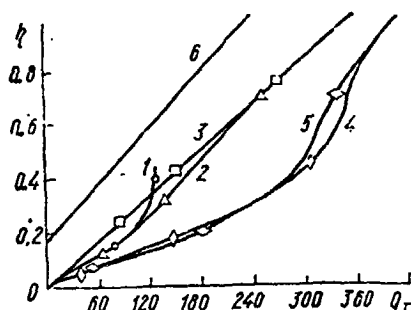


Fig. 3. Dependence of minimum relative losses of oxygen  $\eta$  on specific heat inflows  $Q_T$  for storage in various regimes ( $Q_T$ , j/cm<sup>3</sup>):

1. Storage in regime I;
2. Regime II; 3. Regime III;
4. Regime IV;
5. Regime V; 6. Storage of liquid boiling at  $P = 1$  ab. atm.

The relative losses  $\eta$  for a given level of heat inflows  $Q_T$  are determined as follows. Given the condition  $Q_T = Q_V^I$  from the plots  $Q_V = Q_V(T_K)$ , let us find the final-state temperature  $T_K$ , which in turn uniquely determines the density of the condensed phase at the end of storage. Further, it remains only to use Eq. (7) for the calculation. The results of calculations for hydrogen, nitrogen, and argon are given in Figs. 2-5 in the form

#### Storage in Regime II

If the heat inflow  $Q_T$  exceeds the cold storage  $Q_V^I$ , nondrainage storage in regime I is no longer possible, and other regimes must be used, for example, storage in regime II with drainage of vapor at the end of storage at the temperature  $T_K$ .

It must be noted that in the period of nondrainage storage in regime II, (as in regime I), the mean-volume density of vessel filling  $\rho_V$  is unchanged, and is equal to the density of the condensed phase at the temperature  $T_K$ . Thus, in the course of heating there is always a vapor cushion present, and only at its end can the condensed phase fill the entire vessel volume.

We obtain the mean-volume density of charging at the end of storage for regime II by subtracting from the density of the condensed phase at  $T_K$ , the mean-volume loss of mass in the drainage period, which is  $\frac{Q_T - Q_V^I(T_K)}{r(T_K)}$ . As a result, we have

$$\rho_V^* = \rho(T_K) - \frac{Q_T - Q_V^I(T_K)}{r(T_K)} \quad (14)$$

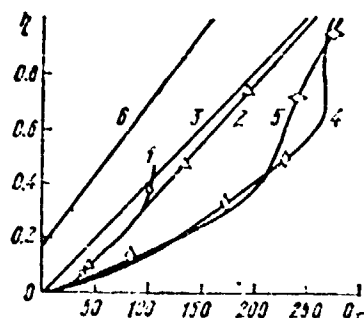


Fig. 4. Dependence of minimum relative losses of nitrogen  $\eta$  on specific heat inflows  $Q_T$  for storage in different regimes ( $Q_T$ , j/cm<sup>3</sup>): 1. Storage in regime I; 2. Regime II; 3. Regime III; 4. Regime IV; 5. Regime V; 6. Storage of liquid boiling at  $P = 1$  ab. atm.

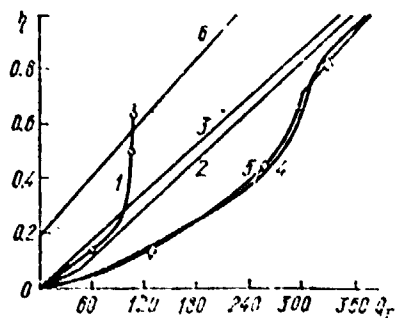


Fig. 5. Dependence of minimum relative losses of argon  $\eta$  on specific heat inflows  $Q_T$  for storage in different regimes ( $Q_T$ , j/cm<sup>3</sup>): 1. Storage in regime I; 2. Regime II; 3. Regime III; 4. Regime IV; 5. Regime V; 6. Storage of liquid boiling at  $P = 1$  ab. atm.

Substituting this expression in Eq. (7), we get

$$\eta = 1 - \frac{|Q_V^I + \rho(T_K) \cdot r(T_K)| - Q_T}{\rho_m \cdot r(T_K)}. \quad (15)$$

In regime II, we introduce the function of the cold reserve with the expression:

$$Q_V^{II} = Q_V^I + \rho(T_K) \cdot r(T_K). \quad (16)$$

Then the expression for the relative losses becomes:

$$\eta = 1 - \frac{Q_V^{II} - Q_T}{\rho_m \cdot r(T_K)}. \quad (17)$$

#### Storage in Regime III

If the cryogenic substance is to be stored in isothermal conditions with constant drainage of vapor (as is usual and customary), the function of the cold reserve  $Q_V^{III}$  is:

$$Q_V^{III} = \rho(T_K) \cdot r(T_K). \quad (18)$$

To calculate the relative losses, again we can use a relation of the type (17), whence we can readily see that the minimum losses of the substance are attained at the temperature  $T_{min}$ , that is, for storage in the solid state with the maximum value of the function  $Q_V^{III} = \rho_m \cdot r_m$ . Then we have:

$$\eta_{min}^{III} = \frac{Q_T}{\rho_m \cdot r_m}. \quad (19)$$

The functions  $\eta^{III} = \eta^{III}(Q_T)$  are shown in Figs. 2-5.

#### Storage in Regime IV

In some sense, regime IV is an improvement on regime II. In

regime IV the volume is filled with the solidified gas at the maximum density  $\rho_m$  and vapor is drained at  $T_{min}$ . Only after attainment in the vessel of the mean-volume density equal to  $\rho_K$  does further storage occur according to regime II. Therefore, compared with regime II, an additional cold reserve of  $r_m (\rho_m - \rho_K)$  will appear in regime IV.

Accordingly, we can write:

$$Q_V^{IV} = Q_V^{II} + r_m (\rho_m - \rho_K). \quad (20)$$

The relative losses as before are determined by a formula of the type (17).

### Storage in Regime V

In this regime, the condensed phase is heated in the unchanged volume of the entire vessel. Gradually the saturated vapor pressure and the temperature of the condensed phase are increased, and the entire vessel volume is filled. The excess volume of the substance occurring owing to thermal expansion is drained in the form of vapor. Therefore the mean-volume density of the substance in the vessel at any moment of time corresponds to the density of the condensed phase at the corresponding temperature. Accordingly, the function of the cold reserve is of the form:

$$Q_V = r_K \rho_K + \int_{T_{min}}^{T_K} r d\rho + \int_{T_{min}}^{T_K} \rho c_s dT + \left[ F(\rho_{tp,T}) = \frac{\lambda \cdot \rho_{tp,T}}{Q}, T_K \geq T_{tp,T} \right]. \quad (21)$$

The relative losses in this regime are also determined by Eq. (17).

### Calculation of the Cold Reserve Function and Relative Loss Function

Each regime has its own cold reserve function  $Q_V$ . We must proceed cautiously in computing them, since the integrands appearing in them have discontinuities caused by first-order phase transitions. Therefore, at these points, the function  $Q_V$  changes discontinuously. For example, the integral  $\int_{T_{min}}^{T_K} r d\rho$  at the triple point has a discontinuity equal to  $r_{tp,T} (\rho_{tp,T}^* - \rho_{tp,T})$ .

The  $Q_V$  functions have a well-defined physical meaning. For each final temperature  $T_K$ , they characterize the maximum amount of heat which in the storage regime II-V can be supplied per unit volume of the substance before converting it into the gaseous state.



Therefore, in those cases when the entire reserve of the cryogenic substance must be evaporated during the storage time, the criterion for selecting the regime is the maximum value of the function  $Q_V$ . As follows from the table, in this respect, regimes IV and V are most advantageous for the storage of nitrogen, argon, and oxygen, since they have similar characteristics.

The ordinate of the function  $Q_V$  at the point  $Q_V = \max$  determines the final-state temperature that is optimal for the given regime,  $T_K$  (cf. table).

If at the end of storage it is required to have a certain amount of the stored substance, the comparison of the storage regimes must be made based on the coefficient of the relative losses  $\eta$ , which in regimes II, IV and V is of the form: /97

$$\eta = 1 - \frac{Q_V - Q_T}{\rho_m \cdot r_m}, \quad (22)$$

where the function  $Q_V$  is determined by Eqs. (16), (20), and (21).

MAXIMUM COLD RESERVES  $Q_V$  (J/cm<sup>3</sup>) AND THE TEMPERATURES  $T_K$  CORRESPONDING TO THEM (°K) FOR REGIMES I-V

Cryog. agent	Regime I		Regime II		Reg. III		Regime IV		Regime V	
	$Q_V$ max	$T_K$	$Q_V$ max	$T_K$	$Q_V$ max	$T_K$	$Q_V$ max	$T_K$	$Q_V$ max	$T_K$
Nitrogen	104	115-125	268	63.15 (sol.ph.)	254	41.7	280	80-100	286	90-110
Argon	110	130-140	357	75-83.8 (sol.ph.)	347	48	377	83.8 (sol.ph.)	382	83.8 (liq.ph.)
Hydrogen	14	31-52	45.8	8.3	45.8	8.3	49.3	23-25	49.5	23-24
Oxygen	146	138-145	360	48-54.36 (sol.ph.)	360	48	407	110-130	408	110-125

For each thermal inflow parameter  $Q_T$ , we can construct a plot of the dependence of the coefficient  $\eta$  on the final-state temperature  $T_K$ . As an example, in Fig. 1 are shown these curves for the case of the storage of nitrogen in regimes II and IV. The dashed curve in this figure corresponds to the losses for nondrainage storage regime I.

If during all storage regimes the minimum value of the coefficient  $\eta$  is brought into correspondence to each value of the parameter  $Q_T$  for the family of curves  $\eta = \eta(T_K)$ , we get the dependence of the

minimum losses on the heat inflows  $Q_T$ . The plots  $\eta_{\min} = \eta_{\min}(Q_T)$  for the different regimes and substances are shown in Figs. 2-5.

#### Comparison of Different Storage Regimes

It follows from Figs. 2-4, for nitrogen, oxygen and argon when the heat inflows are respectively less than 65, 105, and 96 j/cm<sup>3</sup>, the losses in regime II coincide with the losses in regime I, that is, for these heat inflows preference must be given to nondrainage storage. For larger values of  $Q_T$ , the losses in regime I are greater, which is associated with the appreciable reduction in the density of the liquids near the critical point.

A typical feature of hydrogen when stored in regime II is the fact that the minimum losses are attained at constant drainage at the initial temperature  $T_{\min}$ , that is, among the regimes I, II and III, the optimal regime is III (Fig. 2).

The losses for storage in regime IV and V prove to be approximately the same. In the region of smaller heat inflows, the losses are somewhat lower in regime V, while at larger heat inflows, losses are 10-15% lower in regime IV. Therefore, for storage purposes, regimes IV and V lead to roughly equal losses. However, regime IV is much easier to achieve technologically, therefore, it must be recommended for practical use.

Since the losses in regime IV are 1.5-2 times lower compared with regime II, regime IV must be considered as the optimal method of storage. One drawback of regime IV is that for large values of heat inflows,  $Q_T$ , the optimal temperatures at the end of storage are close to the critical points. This dictates the necessity of designing vessels for high pressures. Therefore, it can be shown that from the standpoint of minimalization of the total weight of the storage system, the final-state temperature is required to be selected below the optimal temperature.

For comparison, Figs. 2-5 also present the curves of relative /98 losses for storage of cryogenic agents boiling at a pressure of 1 ab atm (curves 6). From a comparison of these curves it follows that the use of solidifying gases makes it possible to reduce by severalfold the losses compared with storage of cryogenic substances. For example, in regime IV a reduction of losses by three to four times is achieved.

These calculations are based on the heats of vaporization and specific densities adopted from the studies [7, 11, 12-15]. As the result of the absence of adequate data on specific density and heat of sublimation of solid hydrogen, linear functions plotted based on two points were adopted for them [7, 14].

In these storage regimes, the heat of vaporization and the heat capacity of the condensed phase are used efficiently, while

the cold of the vapor drained is not used at all. For nitrogen [16], the use of shields cooled with drained vapor gives an advantage of not more than 20-30%.

The situation is altogether different when hydrogen vapor is used. However, estimates of the effectiveness of hydrogen vapor-cooled shields are contradictory and are given by the quantities 1.5 and 4 [16, 17]. To revise these values and to determine the optimal temperature conditions for the storage of hydrogen with the use of vapor cold, let us make an additional analysis of this problem.

At the present time, the most effective low-temperature insulation is laminated-vacuum insulation. According to the data in [5], not only in nitrogen but also in hydrogen vessels the temperature of the layers of insulation adjoining the cryogenic surface reach 120-130° K. The temperature of the shields cooled by the vapor does not exceed 120° K. Accordingly, and considering the absence of data on the temperature dependence of the coefficient of thermal conductivity of the insulation  $\lambda_{in}$  below 100° K, we will assume that the optimal location of the shield is between the insulation and the hydrogen vessel. Owing to the small difference in the dimensions of the shield and the hydrogen chamber, their areas can be assumed identical. It must be noted that the assumption we adopted above has no effect whatever on the results of further estimates, since the analysis was made in the criterial form. Therefore, the presence of insulation between the hydrogen vessel and the shield is equivalent to changing the reduced black-body factor  $\epsilon_{red}$  and leads only to a change in the value of the criterion  $K_T$  (see Eq. (26)).

As earlier, we will specify the heat inflows to the shield in the general form by means of  $Q_T$ . We present an example of the values of the parameter  $Q_T$  that are possible in practice. To do this, let us determine the heat inflows to the vessel containing hydrogen, of diameter  $D_s = 3$  m, insulation thickness  $\delta = 8$  cm, and coefficient of vessel thermal conductivity --  $\lambda_{in} = 1 \cdot 10^{-6}$  w/cm° K, for an outer hull temperature of 300° K and a storage time of one year. From the relation

$$Q_T = \frac{6\lambda_{in} \cdot \Delta T \cdot \tau_{xp}}{D_s} \quad (23)$$

After substituting numerical values, we get  $Q_T = 23$  j/cm<sup>3</sup>.

Considering that heat transfer between the hydrogen vessel and the shield is only radiative and assuming that the temperature over the entire shield is constant, from the condition of the heat balance, we obtain the following equation for determining the shield temperature  $T_s$ :

$$\frac{6}{T_s} \epsilon_{\text{red}} \sigma (T_s^4 - T_e^4) \cdot r_{\text{sp}} = \frac{Q_r}{1 + \frac{\epsilon_p^0 (T_s^4 - T_e^4)}{r} + \frac{r_{\text{kon}}}{r}} \quad (24)$$

This equation can be easily represented in dimensionless form:

$$\theta^4 - 1 = \frac{\lambda_r}{1 + \frac{\epsilon_p^0 (\theta^4 - 1) r_e + r_{\text{kon}}}{r}} \quad (25)$$

where the determining criterion is:

/99

$$K_r = \frac{Q_r \cdot D}{6 \epsilon_{\text{red}} \sigma \cdot r_{\text{sp}} \cdot T_e^4} = \frac{\lambda_{\text{in}} \cdot \Delta T}{6 \epsilon_{\text{red}} \sigma T_e^4} \quad (26)$$

Physically, the criterion  $K_T$  shows the ratio of the heat inflows through the insulation to the shield to the radiative energy emitted by the vessel at the temperature  $T_e$ , °K.

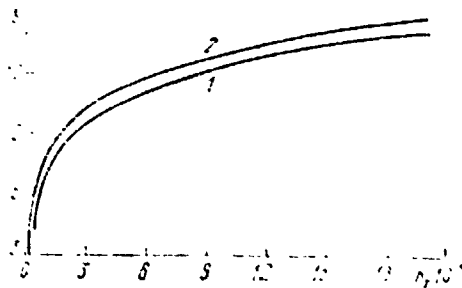


Fig. 6. Change in dimensionless temperature  $K_T^{(0)}$  of hydrogen vapor-cooled shield as a function of the criterion  $K_T$ :

1. Use of heat capacity of vapor and heat of vapor to ortho-conversion. 2. Use only of vapor heat capacity

From Eq. (25), we can easily determine the dimensionless shields temperature  $\theta$  for various criteria  $K_T$ . Fig. 6 shows the dependence of the dimensionless shields temperature  $\theta$  on the criterion  $K_T$ , setting the temperature of solid hydrogen vapor  $T_e$  equal to 8.3° K and the change in the heat of conversion  $r_{\text{KOH}}$  is adopted according to the data in [7]. From the dimensionless temperature  $\theta T_s$ , the specific heat inflows  $Q_e$  to the hydrogen vessel are determined by the relation:

$$Q_e = \frac{6}{D_s} \epsilon_{\text{red}} \sigma (\theta^4 - 1) T_s^4 \cdot r_{\text{sp}} \quad (27)$$

We estimate the effectiveness of vapor use by the coefficient

$$K_v = Q_T / Q_e \quad (28)$$

Criterion  $K_v$  is now determined and represents a function of the criterion  $K_T$ . The correspondence between  $K_T$  and  $K_v$  can be easily found, by determining from Fig. 6 as a function of  $K_T$  the value of  $\theta$ , and from it calculating, using Eq. (28), the coefficient  $K_v$ . The resulting dependence is shown in Fig. 7. From the figure it follows that the use of vapor cold makes it possible to reduce by two to five times the heat inflows into hydrogen. It can also be noted that the use of the heat of vapor to ortho-conversion yields an additional gain of 15-25%.

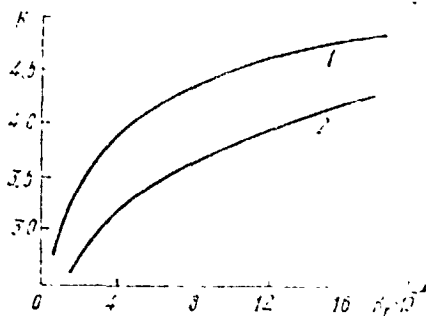


Fig. 7. Dependence of effectiveness of use of vapor  $K_V$  of hydrogen vapor on criterion  $K_T$  at the initial vapor  $T$  temperature  $8.3^\circ \text{K}$ :  
1. Using the heat of vapor to ortho-conversion  
2. Without using this heat

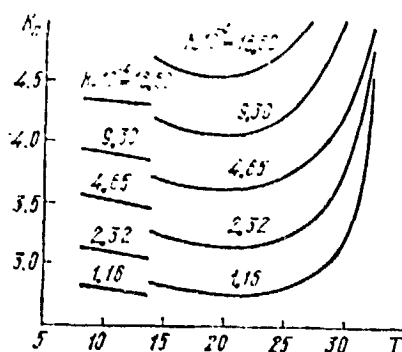


Fig. 8. Dependence of the effectiveness of vapor use  $K_V$  of hydrogen vapor on the temperature of the condensed phase  $T_e$  for different values of criterion  $K_T$  ( $T_e$ ,  $^\circ \text{K}$ ).

From the data in Fig. 7 we can determine that a twofold increase or decrease in the criterion  $K_T$  causes an equivalent change in the

It is also of interest to determine the dependence of the coefficient  $K_V$  on the temperature of the solid or liquid hydrogen at fixed values of criterion  $K_T$ . These curves are in Fig. 8. Clearly, the largest value of  $K_T$  are close to the critical point. However, for the final estimate of the optimal temperature at which the hydrogen must be stored and its vapor strained, we must determine the maximum of the products  $K_V \cdot \rho \cdot r$  since it is precisely this quantity that determines the losses in the regime of isothermal storage with drainage:

$$\eta = \frac{Q_T}{K_V \cdot \rho \cdot r} \quad (29)$$

Plots were constructed of the  $\frac{1}{100}$  function  $K_V \cdot \rho \cdot r$  for different values of the criterion  $K_T$ . From the change in this function follows the conclusion that in the method involving the drainage of vapor, the storage of hydrogen in the solid state at the lowest possible temperature is optimal.

Since the function  $K_V \cdot \rho \cdot r$  takes on the largest values in the region of minimum temperature and, below the triple point temperature changes only slightly, when solid hydrogen is used at any temperature we can employ the dependence  $K_V = K_V(K_T)$  (see Fig. 7). From these data we also conclude the effect of the blackbody factor, specific heat inflows  $Q_T$ , storage time  $\tau_{xp}$ , and vessel dimension  $D_s$  on the effectiveness of vapor use  $K_V$ . As follows from Eq. (26), a change in any of these quantities, for example, by twofold, is equivalent to a proportional change in criterion  $K_T$ .

coefficient  $K_v$  by only 10-12% in the region of the values of criterion  $K_T = (0.2 + 20) \cdot 10^4$  that are attainable in practice.

The value of situating a second intermediate shield with the same blackbody factor as the first shield and the vessel wall between the shield and the hydrogen vessel was studied roughly according to the same scheme.

The installation of an uncooled shield is equivalent to decreasing the reduced blackbody factor between the shield and the vessel by  $(3 - \epsilon)$  times and therefore provides an additional benefit of 12-15%. The use of part of the cold of the escaping vapor at the shield can increase the overall effectiveness of the vapor use by 25%.

In the study, the possibility of using the cold of vapor for storage in regime IV was also evaluated. It was found that owing to the presence of a lengthy period of nondrainage storage in this regime, utilization of vapor cold produces a negligible benefit. Total losses for storage in regime IV using vapor cold amount only to several percentages lower than in regime III when a vapor-cooled shield is present. Therefore, since working in regime III is simpler, it is precisely this regime that must be given preference.

The main conclusions of this study are as follows:

1. For long-term autonomous storage of cryogenic agents, it is best to begin it in the solid state.
2. The smallest losses for argon, nitrogen and oxygen are achieved for storage in regime IV.
3. The optimal method of storing hydrogen with minimum losses is the regime of isothermal storage of solid hydrogen at the lowest possible temperature, with the continuous drainage of vapor and the use of vapor cold reserve in shields.
4. The use of the cold of escaping vapor when hydrogen is stored in the isothermal regime makes it possible to reduce losses by two to five times.
5. The benefit from using the heat of vapor to ortho-conversion of the escaping vapor is as much as 25%.
6. Placement of the second uncooled shield reduces hydrogen vapor losses by 12-15%.

The use of the second intermediate shield, vapor-cooled, means an additional reduction of losses by 20-25%.

# REFERENCES

/101

1. Energeticheskiye ustanovki dlya kosmicheskikh apparatov  
(Power Plants for Spacecraft), "Mir", Moscow, 1964.
2. Plaks, N., and Weiswurm, K., "Solidified Oxygen for Breathing in Space," Adv. in Cryog. Eng., 13, (1968).
3. Eriks, Konstruirovaniye i tekhnologiya mashinostroyeniya (SShA), No. 1, (1961).
4. Shifel'bayn, A. G., "Heat Transfer in Shield-Vacuum Systems in the Low Temperature Region," Kand. dis. (Candidate's Degree Dissertation), Moscow, 1969.
5. Mikhal'chenko, R. S., "Thermoconductivity of Laminated-Vacuum Thermal Insulation and Its Use in Cryogenic Vessels of Small Size, Heat Transfer Mechanism," Avtoreferat. kand. diss. (Author's Abstract of Candidate's Degree Dissertation), Khar'kov, 1969.
6. Gerald, L., AJAA Paper, No. 69-27, 1969.
7. Caren, R. P., Cryog. Technol., 4(1), (1968).
8. Lazarev, B. G., Milenko, Yu. A., and Breslavets, K. G., DAN SSSR, 178(1), (1968).
9. Mikhal'chenko, R. S., Getmanets, V. G., and Arkhipov, V. T., IFZh, 22(4), (1972).
10. Mikhal'chenko, V. S. et al., IFZh, 23(2), (1972).
11. Vasserman, A. A., ibid, 7, (1964).
12. Cryogenic Engineering News, 4(1), (1969).
13. Yesel'son, B. N. et al., Svoystva zhidkogo i tverdogo vodoroda  
(Properties of Liquid and Solid Hydrogen), Standarty Press, Moscow, 1969.
14. Manzheliy, V. G., "Thermal Properties of Solidified Gases," Avtoref. dokt. dis. (Author's Abstract of Doctorial Dissertation), Khar'kov, 1969.
15. Malkov, M. P. et al., Spravochnik po fiz.-tekhn. osnovam glubokogo okhlazhdeniya (Handbook on Engineering Physics Fundamentals of Deep Cooling), Gosenergoizdat, Moscow-Leningrad, 1963.

16. Murto, P. J., "A Gas-shielded Storage and Transport Vessel for Liquid Helium," Adv. in Cryog. Eng., 7, (1962).
17. Suslov, A. D., Belov, V. V., and Bogachenko, V. N., Trudy MVTU im. N. Ye. Baumana (Transactions of the Moscow Higher Technical Schools imeni Bauman), Moscow, 1970, p. 138.



N74-3

## INTERMEDIATE MEMORY DEVICES

G. V. Basalayev, A. B. Kmet', M. A. Rakov, V. A. Tarasevich

Investigation of space and the planets of the solar system by /101 means of spacecraft poses a number of problems whose solution requires methods of information theory and the building of specialized radio-electronic equipment. Difficulties in resolving these problems stem mainly from the restricted conditions, determined by the following factors: the high velocities of spacecraft, the restricted maximum power of transmitter, characteristics of transmitting antennas, losses in space, and the presence of receiver system noise.

The theory of information transmission at the present level of development allows us to find optimal methods of processing and transmitting signals along communication channels in relation to the requirements imposed on them.

This article examines in brief outline problems and several methods of transmitting and processing information for whose actual realization operational memory devices are needed. Specific devices capable of implementing these methods are examined. The first of these problems is associated with a necessity of a finite time period for transmitting a specified volume of information with the necessary confidence level in a selected coding method [1, 2].

The specifics of the signals that are typical of space studies include the fact that one is dealing with  $n$ -dimensional vectors at a specified point in space determined by the readings of  $n$ -spacecraft transducers. Since transmitting data requires a certain time period, readings from the first and subsequent ( $n$ -th) transducers obtained from the earth will pertain to different points in space separated by a distance that is proportional to the time of transmission and the velocity of the craft. Considering the fact /102 the rates of change of components in space are quite high, in practice it is impossible to restore the value of the  $n$ -dimensional vector at a specified point from data acquired. To eliminate errors of this kind, it is useful to store the readings of  $n$ -transducers pertaining to a single point in space during the time of transmission. The use of the operational memory in this case is highly desirable, since it does not lead to changes in the conditions of signal coding and transmission over the information communication channel and makes it possible to transmit the stored information at a rate and an error probability that is identical for the entire for the entire system.

Let us consider a second case that requires the use of memory devices in equipment for space research. The selection of the transmission system is made based on the error probability at

maximum transmission efficiency. The transmitter power is one of the primary limiting conditions for spacecraft with which investigations are made of planets in the solar system. Based on this requirement, one can find the optimal ratio between the error probability and the efficiency of transmission. However, at a high level of interference, signals are encountered whose transmission with an error probability calculated for the transmission of all the information is unsatisfactory. Using transmission with methods of storage or re-interrogation, the error probability for these signals can be lowered to the required level [3]. Let us explain these methods in brief.

The method of transmitting with storage consists of transmitting a constant signal over the extent of  $m$  messages. The result of this accumulation of readings leads to increasing the signal-to-noise ratio by  $m$  times.

This transmission can be implemented by using  $m$  channels with identical error probability and transmission time. However, this method is disadvantageous owing to the low efficiency of the use of each channel. By storing the value of the parameter for whose transmission it is required to increase the signal-to-noise ratio by  $m$  times, using a special device, over the time required for  $m$  messages, one can achieve the required signal-to-noise ratio even with a signal-channel transmission system. In this case, the efficiency of transmission is reduced only in the transmission of the given signal, while the transmission of the remaining signals is conducted at the design efficiency.

Transmission with re-interrogation (or feedback) increases the confidence level of the transmission by using the greater power levels of ground facilities. The use of this method makes it possible to vary the time of transmission of different signals in relation to the conditions, and thus to produce conditions for organizing an optimal communications system. By storing the value of each signal at the input of the transmitter until the signal confirming the reception of this signal arrives, permitting the next signal to be connected to the input of the transmitter, one can attain optimal efficiency.

All these cases pertain to the use of memory devices directly in the information transmission systems. Let us now examine several principles of the preliminary processing of functions using methods of storing their values at discrete moments of time and capable of reducing the volume of transmitted information without lowering the effectiveness of investigations.

In space studies, one must deal mainly with functions whose frequencies spectrum is limited. According to the Kotel'nikov theorem these functions can be restored with pre-assigned precision from equidistant instantaneous values, whose number  $n \geq 2f_0T$ , where  $f_0$  is the frequency band. By storing the instantaneous

values of the function at the instants of time  $t_i$ , where  $i = 1, 2, \dots, n$ , and then, by transmitting them over the communication channel one can restore the form of the function under study over the time interval  $T$ . The storage method is advantageous here in two cases:

- 1) the sampling step is shorter than the time of signal transmission over the channel;
- 2) the sampling step is somewhat larger than the transmission time.

In the first case it is not required to increase the transmission rate over the channel; in the second case, the organization of the transmission system is not made more complicated. /103

By comparing the stored preceding and subsequent values of the function over the assigned time interval  $T$ , one can determine the presence of function extrema from the change of sign of the difference between two neighboring values.

Since the number of determining function values is finite, one can examine several discrete values of the amplitudes differing from each other by twice the magnitude of the error caused by the discreteness in [4]. In other words, one can quantize these functions in amplitude. If it becomes necessary to perform amplitude selection of extrema, then by specifying the sampling step in amplitude (zone sizes), one can determine only those extrema that exceed the discreteness step.

Preliminary processing of information on board can be easily organized if the task of determining the number and values of function extrema over the time  $T$  arises.

In the course of this or similar data processing, one can determine the probability that the function will appear in the future, and on this basis use methods of transmission with lower error probability for the more probable values of the function, at the cost of degrading the transmission of low-probability values.

Let us further examine devices of operational (intermediate) memory with which the methods of data processing and transmission described in the first section can be implemented in practice. Since we will be talking about devices using memory cells with multistable elements, for convenience in reading the following material, let us consider in brief the operating principle of the time-pulse multistable elements used.

A multistable element is a multiport device with a multihump amplitude characteristic. This multiport device, uncomprised by feedback, has several equilibrium states, whose number is determined by the ratio of reference and bar frequencies fed from an external excitation source [5, 6]. The equilibrium states

differ from each other by the magnitude of the static feature in the form of the levels of constant voltage and by the value of the phase of pulse sequence. The advantage of these elements is that a change in the number of equilibrium states over wide limits is not associated with a change in equipment, and also in that the complexity of the overall excitation source is not related to the number of multistable elements in the system. The presence of two features of equilibrium state makes it possible to use effective methods of data input and gives additional advantages in data processing.

The use of multistable elements made it possible to built economical multichannel storage devices for their use in spacecraft in the measurement of n-dimensional vectors. The use of these devices at the same time permits reducing the number of channels requiring the storage of information in the long-term memory, whose necessity is dictated by the restricted time of direct transmission during periods of radiovisibility. In this sense, these devices fulfill the function of an intermediate memory.

Let us first dwell on the 32 channel device for storing analog signals. (Fig. 1). The storage of input signals is performed in the block of memory elements, where to each element there uniquely corresponds a storage element consisting of a multistable element and a servocircuit, which is actuated during the data input time and charges the element capacity up to the magnitude of the signal. The operation of the entire system is synchronized with a pulse sequence fed from without. At the moment of arrival of the first interrogation pulse, the reset device is triggered, resulting in the triggering of a strobe-pulse during whose period data is fed into all 32 elements. At the same time, the signal of the first channel appears at the output of the commutation block. The next, 31st interrogation pulse connects the remaining channels alternately to a common output. The 32nd pulse triggers the reset device and the operating cycle is repeated. For convenience in removal and checking the operation of the subsequent telemetry circuits, the first two channels store constant reference signals with known amplitude. The presence of the phase feature of the element states made it possible to use in the device, instead of an analog commutator a pulse commutator consisting of a counter of 32 positions and a diode matrix-decoder. At the output of the commutator, the phase feature pulses in the code-to-analog converter are converted into an analog signal by means of a sawtooth voltage, which is also used for the multistable elements. Owing to the presence of the circuit of an adjustable time delay, the error in transforming from parasitic time delay arising in the transmission of pulses of the phase feature along the commutated circuits is appreciably reduced. /104

This device has the following technical specifications: data input time is 5 msec; data storage time is unlimited; power required is 5 w; volume is 6 decimeters<sup>3</sup>; weight is 6 kg; precision class is 1.5.

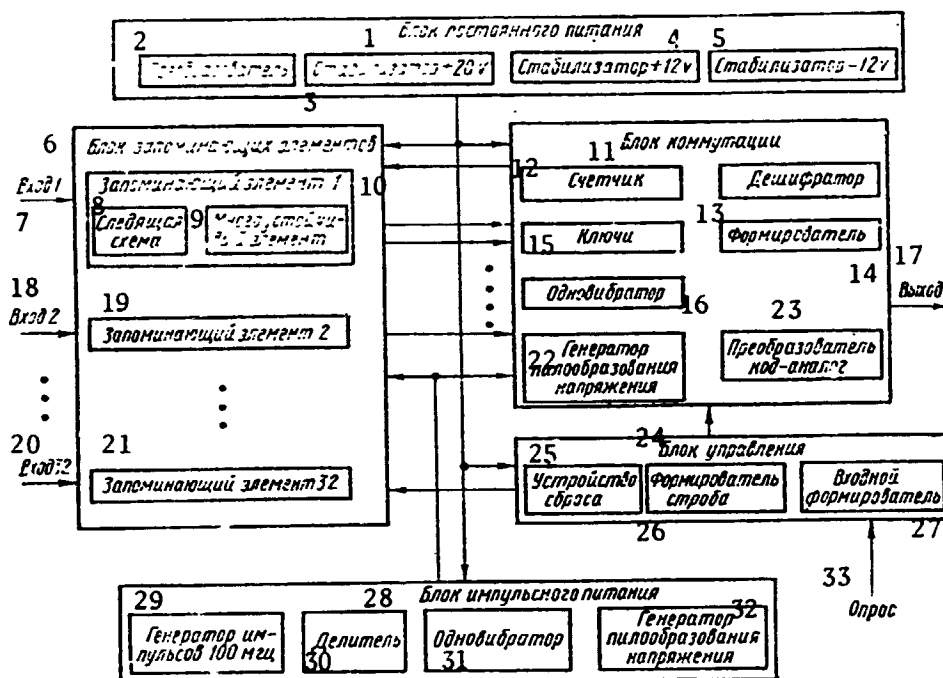


Fig. 1. Block diagram of 32-channel device for storage of analog signals, varying in the limits 0 to +6 v.

- KEY:
- |                             |                                |
|-----------------------------|--------------------------------|
| 1. Constant supply block    | 19. Memory element 2           |
| 2. Converter                | 20. Input 32                   |
| 3. Stabilizer +20 v         | 21. Memory element 32          |
| 4. Stabilizer +12 v         | 22. Sawtooth voltage generator |
| 5. Stabilizer -12 v         | 23. Code-to-analog converter   |
| 6. Block of memory elements | 24. Control block              |
| 7. Input 1                  | 25. Interrogator               |
| 8. Servo circuit            | 26. Strobe shaper              |
| 9. Multistable element      | 27. Input shaper               |
| 10. Memory element 1        | 28. Pulse supply block         |
| 11. Commutation block       | 29. 100 MHz pulse generator    |
| 12. Counter                 | 30. Divider                    |
| 13. Decoder                 | 31. Monovibrator               |
| 14. Shaper                  | 32. Sawtooth voltage generator |
| 15. Switches                | 33. Interrogation              |
| 16. Monovibrator            |                                |
| 17. Output                  |                                |
| 18. Input 2                 |                                |

Let us further present the characteristics of a storage device distinguishing it from the preceding one in that it has four common outputs instead of one, and an additional "calibration" regime is

introduced. The technical solution here has several points of difference. To simplify the circuitry of the device and to reduce its power load, the memory cells in each channel are simplified and consist of capacitative memory units [MU], marked by great simplicity, but with a short data storage time. The unlimited data storage time in the device is achieved by using a servo-multivalued correction circuit, achieved by a single multistable element for a group of AU.

The input time is 2 msec; the storage time is unlimited; input impedance is  $10^8$  ohms; the power required is 2 w; the volume /105 is 2 decimeters<sup>3</sup>; and the weight is 2 kg.

Use of these devices is promising for operation in information transmission systems using the system of accumulation and the system of re-interrogation. This necessitates the appropriate organization of the functioning of the control block, without modifying the operating principle of the devices as a whole. These devices are applicable for storage over a specified time interval of the shapes of functions under study, whose frequency spectrum permits selecting the sampling step larger than the data input time into the memory cells.

Of some interest is an analyzer of extremal values of functions in a specified time interval, involving the use of multistable elements as analog-to-discrete transformers of input voltages. The magnitudes of the zones of the potentials sign of the stable states determine the amplitude selection of the extrema.

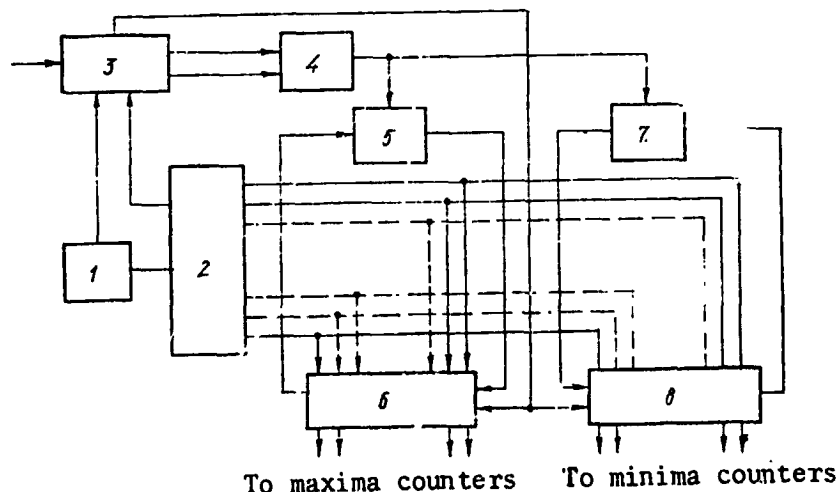


Fig. 2. Block diagram of analyzer

The analyzer is constructed according to the block diagram (Fig. 2) and operates as follows. Voltage from the static output of analog-to-discrete converter (3), in the form of a stepwise-varying

function, controls, with a trigger the generation of extrema, (4), which responds to the change of signs of the pulse fronts of this voltage. This is achieved by using a trigger with divided inputs, where one input responds only to the first positive front of the input voltage arm and the second -- to the first negative front. This trigger, in turn, is controlled by triggers determining the type of extrema, where the trigger generating the maximum values (5) is controlled only by positive pulse fronts, while the trigger controlling minimum values (7) is controlled only by negative pulse fronts. To determine the specific zone in which an extremum lies, the pulse sequence at the phase-impulse output of the analog-to-discrete converter is used, together with pulse voltages at the outputs of the pulse distributor (2) and the triggers determining the type of extremum. To each zone there corresponds a specific pulse sequence at the phase-impulse output of the analog-to-discrete converter and at the corresponding output of the pulse distributor which carries out their spatial distribution. Its operation is synchronized by the bar pulse generator (1), which provides for high stability of zone separation. These pulse sequences are sent to the coincidence matrices (6, 8) performing the commutation of signals to the channels of the corresponding zones. When an extremum is present, the triggers for determining the type of extremum, due to the presence of a reset circuit pulse, pass one pulse of the phase-impulse sequence to one of the outputs of the corresponding matrix. Then these pulses are read by the counters of the /106 zones in which the extrema occurred.

Depending on the problem to be solved, subsequent data processing can be of different kinds and can be conducted either on board the craft or on earth. Problems of further data processing require a more detailed study for specific cases and are not examined in this article.

In conclusion we must note that circuitry solutions of memory cells using time-pulse multistable elements make it possible to use to the maximum the achievements in microelectronics. Building memory cells in micromodular standard cases makes it possible to build small-sized universal storage devices with a wide range of problems to be solved in space research.

#### REFERENCES

1. Shannon, C. E., Proc. Z. RE, No. 37, (1949).
2. Balakrishnan, A. V., in the book: Statisticheskaya teoriya svyazi i yeye prilozheniye (Statistical Theory of Communications and Its Applications), "Mir", Moscow, 1967.
3. Kharkevich, A. A., Bor'ba s pomekhami (Interference Control), "Nauka", Moscow, 1965.
4. Taller, V., in the book: Teoriya informatsii i yeye prilozheniya (Information Theory and Its Applications), edited by A. A. Kharkevich, State Publishing House of Physico-mathematical Literature, Moscow, 1959.
5. Dub, Ya. T., and Rakov, M. A., Avtomatika i telemekhanika, No. 7, (1970).
6. Rakov, V. I., Rakov, M. A., and Tarasevich, V. A., in the book: Otbor i peredacha informatsii (Selection and Transmission of Information), No. 24, 1970.